博士論文

High-Accuracy Verification Method of Coordinate Measuring Machines Using a Single-Mode Fiber Optical-Comb Pulsed Interferometer

（シングルモードファイバー光コムパルス干渉計を用いた三次元座標測定機の高精度検査手法）

スダータム　ウィロート

平成 28 年度 博士論文

東京大学
THE UNIVERSITY OF TOKYO

シングルモードファイバー光コムパルス干渉計を用いた三次元座標測定機の高精度検査手法

High-Accuracy Verification Method of Coordinate Measuring

Machines Using a Single-Mode Fiber Optical-Comb Pulsed

Interferometer

指導教員 高増 潔 教授

東京大学大学院 工学系研究科 精密工学専攻

学生証番号 37-137240

スダータム ウィロート

Abstract

This research presents a new optical measurement method of Coordinate Measuring Machine, CMM verification based on the temporal coherence interferometry of the optical frequency comb. The absolute-length measurements are successfully implemented by the first combination of a single-mode fiber optical-comb pulsed interferometer and a ball lens target. The required lengths or absolute positions are controlled by a fiber etalon that is used to modify the repetition frequency of an optical frequency comb. The optical frequency comb directly traces through the rubidium frequency standard to the base SI unit, and a ball lens serves as a three-dimensional target of the interferometer. The principle is original and the experiments were done by the author. Specially, the peak detection method of envelope interference fringe and the automatic measurement was developed for practical real-time applications. The proposed measuring technique was compared with the conventional standard step gauge method. The result is that the measurement procedure is simply and less time consumption. It has a high efficiency for the medium-sized to large-sized CMM verification, long-measuring range up to 10 m with a small measurement uncertainty of ~0.26 μm/m ($k = 2$). In addition, the first complete set of the absolute-length measuring machine has been established. Consequently, this research is not limited for only CMM verification, but also can be applied to other absolute-length measurements in dimensional metrology, which performed as a non-contact measurement. Furthermore, this study provides background knowledge for development of the calibration system using the single-mode fiber optical-comb pulsed interferometers, which is able to identify 21 parametric errors of a CMM based on multi-lateration measurement method. The proposed research is therefore intended to make contributions to the literatures on coordinate metrology, and variety on dimensional metrology.

Contents

Chapter 1 Introduction

1.1 Introduction

This chapter explains the important role of the metrological term, which states that why we have to pay attention accurately about the measurements. Chapter begins with a short brief history of the length definition (metre), and who are responsibilities of world metrology. This part provides background to the reader for understanding the role of metrology.

Subsequently, Coordinate Measuring Machine (CMM) is introduced, which CMMs are widely used to measure the three dimensional sizes, forms, and positions of manufacturing parts. This section describes general term of CMM, error sources, and the maximum permissible error of a CMM.

Next, standardizations of CMM verification are introduced. CMM verification based on artifact test methods is illustrated. At the end of this section, some limitations of standard artifact tests and the problems of large artifacts have been discussed, especially the problem on the large-sized CMM verification.

Finally, aiming to overcome the problems of the conventional verification methods, a new optical measurement technique for the verification of medium-sized to large-sized CMM has been proposed. The research goals, research contributions, and dissertation contents of thesis are presented at the end of this chapter.

1.2 Metrological background

Dimensional metrology has always played an important role in the field of science and technology. The increasing of international trade in the past, the need for international agreement on length and mass measurements formed for the global homogenization of units as embodied in the Metre Convention [1]. The Convention of the Metre is a diplomatic treaty which gives authority to the General Conference on Weights and Measures (CGPM), the International Committee for Weights and Measures (CIPM), and the International Bureau of Weights and Measures (BIPM) to act in matters of world metrology, particularly concerning the demand for measurement standards of ever increasing accuracy, range and diversity, and the need to demonstrate equivalence between national measurement standards.

The metre (m) is the base SI unit of length, which is defined by the Conférence Générale des Poids et Mesures [1, 2]. In 1960 the metre became the first SI unit to be defined based on a quantum phenomenon (wavelengths of light from a specified transition in Krypton-86), and in 1983 it became the first SI unit to be defined by fixing the numerical value of a fundamental constant. "*The metre is the length of the path travelled by light in vacuum during a time interval of 1/299 792 458 of a second.*" The metre is realized at the primary level in terms of the wavelength from an iodine-stabilised helium-neon laser. The BIPM is particularly concerned with ensuring that measurements made in one country agree with measurements made in another. Each country has its own National Metrology Institute (NMI) that is responsible for realizing these units. The committees also define "*The second as equal to the duration of exactly 9 192 631 770 periods of the radiation corresponding to the transition between two hyperfine levels of the ground state of the cesium 133 atom*". This is actually quite a subtle definition because time can be much more accurately measured than any physical lengths can actually be measured. Today, the realization of the metre is essentially based on laser frequency standards, which are increasingly accompanied by techniques to directly generate optical frequencies from the second in terms of optical frequency comb systems.

Additionally, the metrological activities are valuable inputs to ensure the quality of many industrial and quality of life related activities and processes. This includes the need to demonstrate traceability, which means property of a measurement result whereby the result can be related to a reference through a documented unbroken chain of calibrations, each contributing to the measurement uncertainty. For the measurement uncertainty, it is non-negative parameter characterizing the dispersion of the quantity values being attributed to a measurand, based on the information used [3]. Uncertainty is a quantitative measure of the quality of a measurement result, enabling the measurement results to be compared with other

results, references, specifications or standards. Measurement uncertainty can be determined in different ways. A widely used and accepted method, e.g. accepted by the accreditation bodies, is the ISO recommended GUM method, described in the "Guide to the expression of uncertainty in measurement" [4]. Obviously, a traceability chain as shown in **Fig.1.1** is an unbroken chain of comparisons, all having stated uncertainties. This ensures that a measurement result or the value of a standard is related to references at the higher levels, ending at the primary standard. An end user may obtain traceability to the highest international level either directly from a National Metrology Institute or from a secondary calibration laboratory, usually an accredited laboratory.
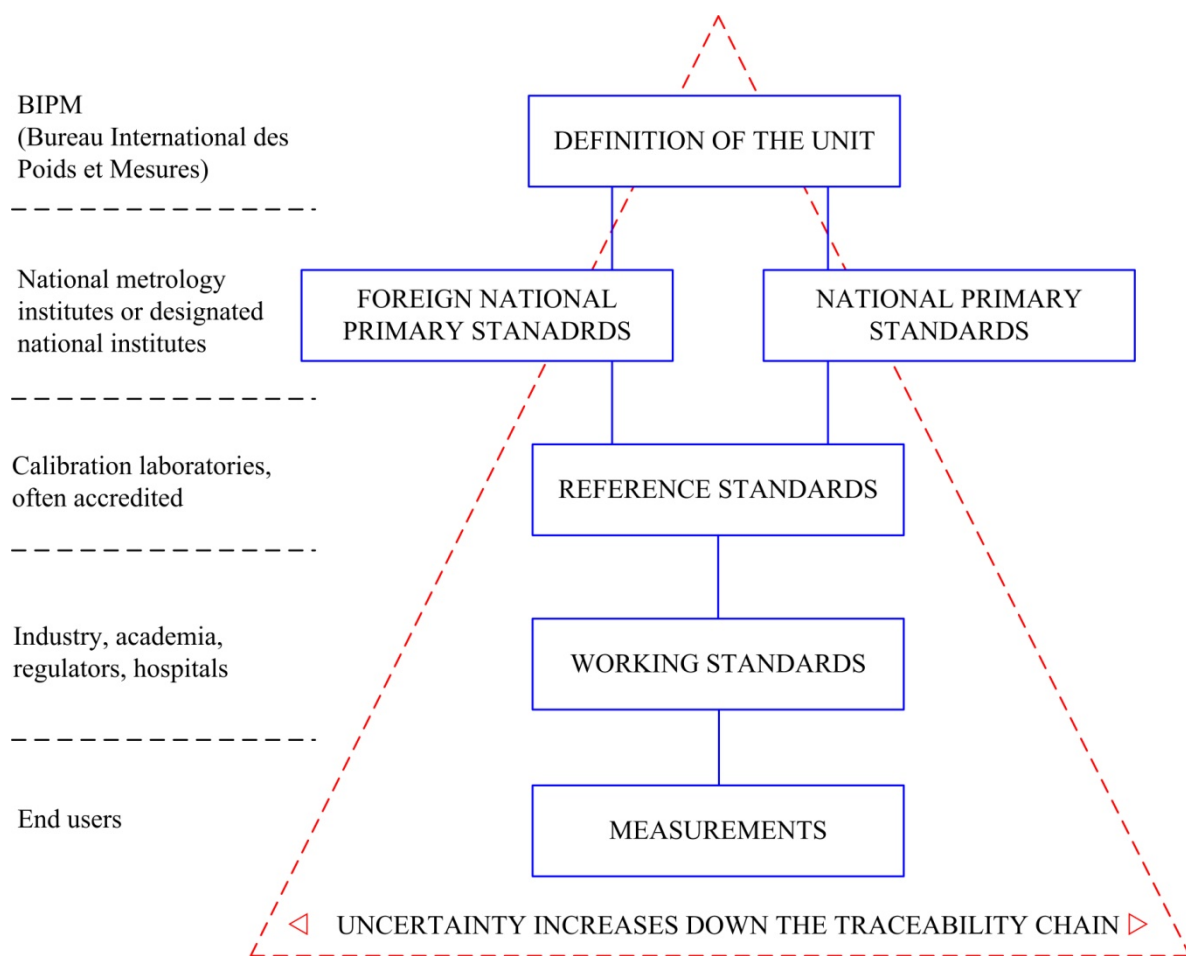
Fig 1.1 The traceability chain.

(*Figure was redrawn from* **Ref. [1]**)

1.3 Coordinate Measuring Machine, CMM

Coordinate measuring machine (CMM) is defined as "*measuring system with the means to move a probing system and capability to determine spatial coordinate on a workpiece surface*" [5]. In general, a CMM is made up of three linear moving axes that allow a contacting spherical stylus tip to move in three mutually orthogonal directions and touch an object to be measured. The position of each of the three axes is recorded during the measurement. Corrections are applied by the computer for stylus tip diameter and probing direction and sometimes for the geometric errors of the machine itself, and associated dimension is calculated. CMMs range in size from small workshop machines that can measure within a 300 mm cube or large size with 3 m or 5 m. CMMs are widely used to measure the three dimensional sizes, forms, and positions of manufacturing parts. However, CMM measurement inaccuracy occurs when there is an error in the relative position between the measured points and the probing points. CMM errors directly influence the quality of product inspections. Therefore, CMM must be calibrated on installation and verified periodically during their operation.

1.3.1 CMM error sources

The accuracy of a CMM is affected by many sources [6–8]. These error sources may cause a change in the geometry of the machine's components present in their mechanical structure such as the guideways, the scales, and the probing system (kinematic errors), the environments in which the CMM is operated these are the ambient temperature, temperature gradients, humidity and vibration (thermo-mechanical errors). In addition, the CMM software used to estimate the geometry of the workpiece is a source of CMM error (motion control and control software error). However, kinematic errors are a major source of errors. They are errors in the machine components due to imperfect manufacturing or alignment during assembly.

For kinematic errors, a moving component always produces six errors of deviation from the nominal path as shown in **Fig. 1.2**. One positional deviation in the direction of motion (linear error), two linear deviations orthogonal to the direction of motion (straightness errors), and three angular deviations or called rigid body rotations (roll, pitch, and yaw). Moreover, there are the three squareness errors between pairs of axes. Therefore, a CMM has 21 sources of kinematic errors. Analyzing the geometrical errors of a CMM depend on the machine geometry and the purpose of the parameter evaluations. It can be decided between "direct" and "indirect" method. Direct measurement method allows the measurement of mechanical errors for a single machine axis without the involvement of other axes. For examples, positioning

error measurement of an axis by a laser interferometer, measurement of straightness errors comparing with mechanical straightness standard, angular error measurement by an autocollimator, and measurement of squareness errors by mechanical square standard. On the other hand, indirect measurement method requires multi-axes motion of the machine for movement to measure positions at different *X, Y, Z* positions such as measurement of 1D artifacts (e.g. a step gauge, and a series of gauge blocks), 2D artifacts (e.g. a ball plate, and a hold plate) and 3D ball plate, or indirect measurement based on displacement measurements such as using laser trackers.
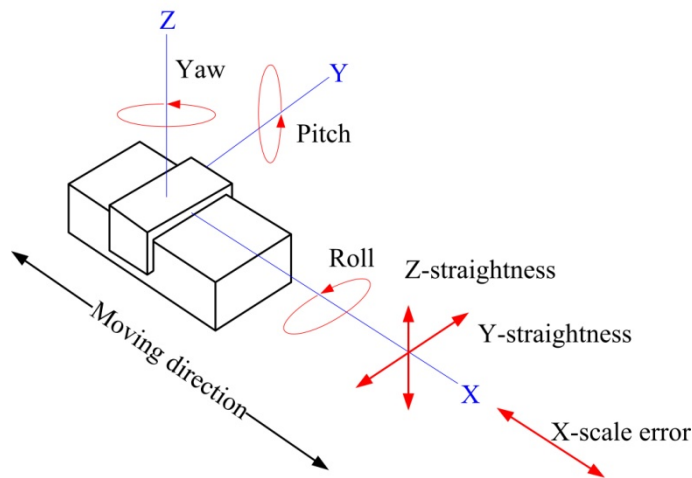
Fig. 1.2 The individual error parameters for one axis.

1.3.2 Maximum permissible error

The term of maximum permissible error of indication of a CMM for size measurement is defined by ISO 10360-1 as the extreme value of the error of indication of a CMM for size measurement $E_{\text{L, MPE}}$, permitted by specifications, regulation etc. for a CMM [5]. Error of indication of a CMM for size measurement means that the error of indication from which the size of a material standard of size can be determined with a CMM, the measurement being taken through two opposite probing points on two nominally parallel planes and normal to one of planes, when the probing points are approached from opposite direction. The maximum permissible error of indication of a CMM for size measurement error, $E_{\text{L, MPE}}$ is stated in one of three forms:

    a) $E_{\text{L, MPE}} = \pm$ minimum of $(A + L/K)$ and B (see **Fig. 1.3 (a)**),

    b) $E_{\text{L, MPE}} = \pm (A + L/K)$ (see **Fig. 1.3 (b)**),

    c) $E_{\text{L, MPE}} = \pm B$ (see **Fig. 1.3 (c)**).

Where;

A is a positive constant, expressed in micrometers and supplied by the manufacturer;

K is a dimensionless positive constant supplied by the manufacturer;

L is the measured size, in millimeters;

B is the maximum permissible error $E_{L, MPE}$ in micrometers, as stated by the manufacturer.

The expressions apply for any location and/or orientation of the material standard of size within the measuring volume of the CMM.

(a)   (b)   (c)
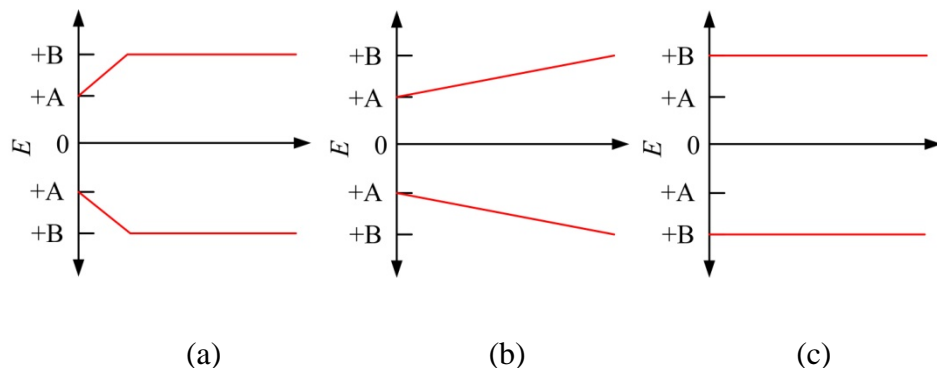
Fig. 1.3 CMM maximum permissible error of indication for size measurement error.

It should be noted that the maximum permissible error of length measurement, E_L is newly defined as the extreme value of length measurement error permitted by specification as shown in part 2 of the ISO 10360:2009, $L = 0$ mm and $L = 150$ mm (default values of ram axis stylus tip offset which means the distance (orthogonal to the ram axis) between the stylus tip and a reference point), are specified.

1.4 Standardizations for CMM verification

Standards and guidelines for CMM verification have been developed and modified to harmonize the performance specifications of a CMM to enable a user to make meaningful performance comparisons when using a machine. Standards have been introduced to obtained machine performance such as International Standard [9] as well as National Standards from some countries [10–13]. **Table 1.1** shows some parts the comparison of specification standards.

Table 1.1 Comparison of specification standards for CMM performance verification

Standards	International ISO 10360-2	Japan JIS B 7440-2	UK BS 6808	USA B89.1.12M	Germany VDI/VDE 2617
Measuring task	Length	Length	Length	Various	Length
Test lengths	5	5	5-10	CMM dependent	5
Artifact tests	End standards	End standards	End standards	End standards	End standards
Measuring positions	7	7	8	Various	7

The testing method for verifying CMM can be categorized at different levels reflecting their application, i.e. calibration, reverification, acceptance test, and interim check. Another type of classification consists basically of method based on measuring 21 sources of error, and method based on measuring certain artifacts. However, most standards prefer to use end standards such as a series of gauge blocks, a step gauge, and a ball plate, and the length is the main measuring task.

1.4.1 CMM verification based on artifact tests

The ISO 10360 series of standards detail the acceptance, reverification tests and interim tests required to determine whether the CMM performs to the manufacturer's stated maximum permissible error of length measurement. The main tests of a CMM are detailed in ISO 10360-2 [9] It states that the calibrated test length should choose five different lengths. The longest calibrated test length should be at least 66% of the maximum travel of the CMM along a measurement line through the calibrated test length. The standard lists four required positions, which shall be the space diagonals as shown in **Fig. 1.4**, and three-position are

parallel to each of the CMM axes. Some examples of a CMM verification based on end standards such as a series of gauge blocks, a step gauge, and a ball plate are demonstrated in **Fig. 1.5–1.7**, respectively. Those artifact tests must be calibrated to produce traceable value of dimensional quantity.
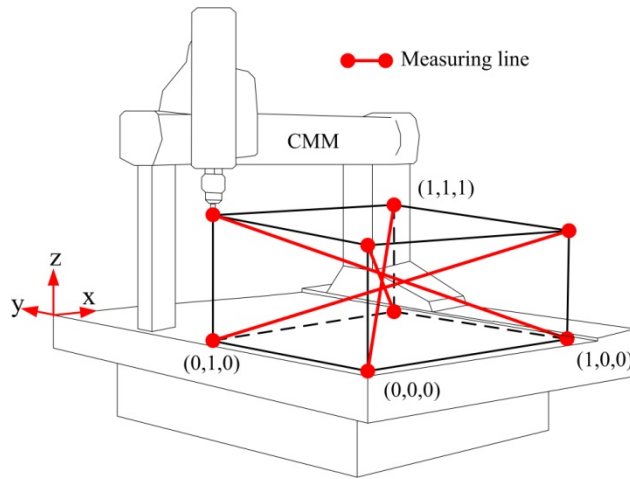
Fig. 1.4 Orientation in the measuring volume; opposite corners of the measuring volume are assumed to be (0, 0, 0) and (1, 1, 1) in coordinates (*X, Y, Z*).

Fig. 1.5 Verification of a CMM using a series of gauge blocks.
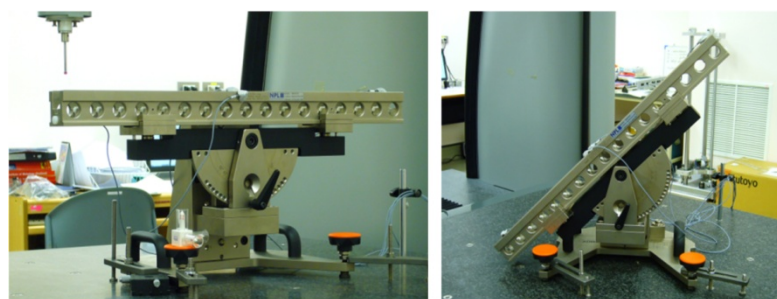
Fig. 1.6 Verification of a CMM using a step gauge.

9
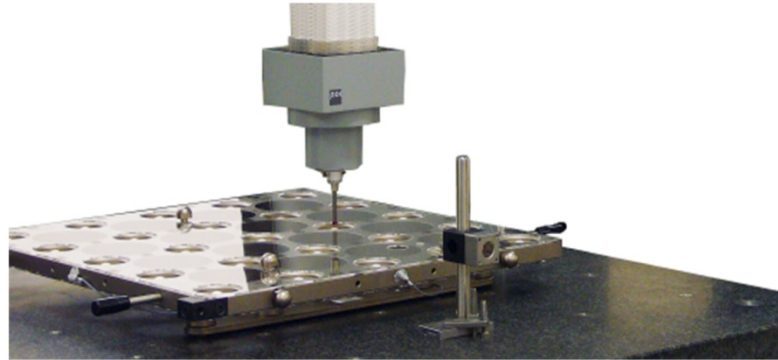
Fig. 1.7 Verification of a CMM using a ball plate.

1.4.2 Artifact tests for large-sized CMM verification

The performance evaluation of the large-sized CMM (measuring volume larger than 2 m^3) has often been problematic because of the unavailability of large calibrated artifacts. Some of National Institute of Metrologies and CMM makers have developed large artifact tests. For examples, a laser ball step gauge has been developed by S.D. Phillips, et al., NIST [14] as shown in **Fig. 1.8 (a)**.
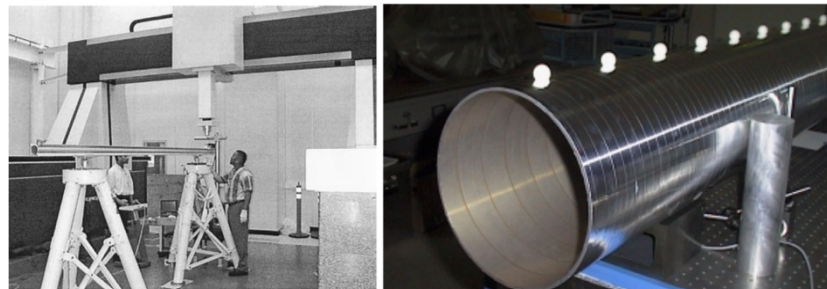
(a) A laser ball step gauge   (b) A multi-ball-beam

Fig. 1.8 Large artifact tests for large-sized CMM verification.

(*Photos (left to right) were copied from* **Ref. [14]** *and* **Ref. [15]**)

The key component of a laser ball step gauge is a spherically mounted retroreflector (SMR) which consists of an optical retroreflector located within a spherical gauging ball, and the length of measurement is obtained by a continuous-wave (cw) laser interferometer system. The system can be used over large distances (over 4 m) with an uncertainty of less than one part per million. However, the measuring length capability is limited by the rigidity of the rail fixture and the length measuring capability of the laser system. Moreover, the measuring

system requires very large supports of the rail fixture to avoid bending error, and the gauge is also hard to carry. Other artifact tests as shown in **Fig. 1.8 (b)** is a disassemblable multi-ball-beam, which has been developed by L. Arriba, et al. [15]. It is made of the same structural elements of the carbon fiber tubes as the L-shaped plate, which can be composed from this tubes of an universal set, e.g. of 1 m, 1.5 m, 2 m, and 3 m modules. Multi-ball-beams are feasible up to 12 m. However, arrangement for 3D-calibrated multi-ball-beams to assess all rigid-body errors require minimum of 5 styli, 10 positions, and 15 measurements. This concept requires more positions than using a ball plate. The gauge is also required a large supporting stand.

According to examples of large artifacts description above, the difficulties of producing large calibrated artifacts are many factors. For instance, the size and weight of these artifacts quickly become unmanageable. The calibration of such large gauges is difficult and expensive, and maintaining the gauge accuracy during storage and handling is troublesome.

1.4.3 Large-sized CMM verification based on cw-laser interferometer

For the direct measurement of the positioning errors, laser interferometers are aligned and measured to the axis of interest. An almost infinite sampling point can be achieved by the use of interferometers for measurement of positioning errors as shown in **Fig. 1.9**.

Fig. 1.9 Positioning error measurements of a CMM using cw-laser interferometer.

For a high accuracy on short and long machine axes, the stabilized cw-laser interferometer has becomes most common for measuring positioning errors of machines.

11

However, for these CMMs, laser interferometer measurements along a body diagonal without losing laser beam strength can be slow and difficult. Moreover, the laser beam cannot be interrupted during measurements, because the interferometers are operated based on the interference fringes counting method. If the laser beam is interrupted, the re-initial measurement at the reference position of the measuring system is required. Since the evaluation length of the conventional cw-laser interferometer operated based on interference fringes counting method, it has practical difficulties in the long-range or large-step measurement, because the target mirror should be installed for translating from the initial position to final position continuously without any interruption.

For three-axes machines, tracking interferometers have been introduced in industry for geometry verification [16–18]. The verification of a CMM with a tracking interferometer is based on the measurement of displacement between the laser tracker and reflector fixed on CMM probing system and moved along a predefined path. The error parameters are calculated from the difference between nominal and measured lengths.
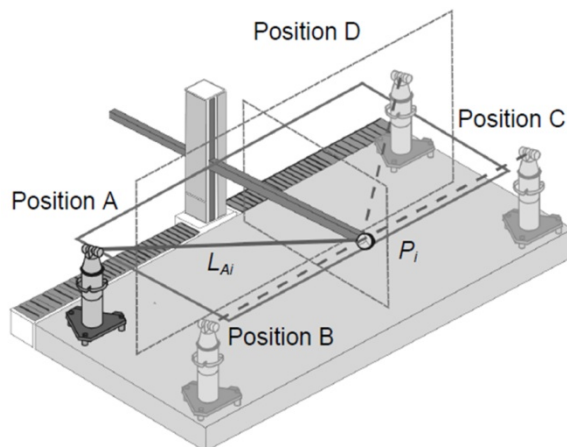
Fig. 1.10 Verification of a CMM using laser tracker.
(*Figure was copied from* **Ref. [16]**)

Fig. 1.10 shows that two or even three dimensional positions can be determined exclusively by length measurements. This procedure is called multi-lateration measurement method [16]. All lengths are measured only using one conventional laser tracker. In turn the tracker is placed in three or even more positions.

The modern tracking interferometer, commercially called "laser-tracer", has been developed by the British and German national metrology institutes, the NPL and the PTB, and Etalon-ag as shown in **Fig. 1.11**. The laser-tracer has a highly stable optical centre which permits spatial displacement measurements with an expanded uncertainty of 0.2 μm + 0.3 μm/m [17]. However, laser tracking system is only a relative measuring device. For each laser tracker position in **Fig.1.10**, a primary unknown length offset has to be considered, and the laser tracker is located manually and therefore its positions are generally not exactly in the same plane with other. In addition, a cat's eye target provides a limited angle of the observation, and tracker beam also cannot be interrupted during measurement as same as cw-laser interferometer.

Fig. 1.11 Verification of a CMM using Laser-Tracer.
(*Photo was copied from Etalon-ag website*)

Although laser tracker can be used to measure for a long-measuring length (> 15 m), the measurement procedure is more complicated when using only one tracking station, because of limitation angle of the target. The location positions of tracker have to be changed during measurement. In addition, for performing geometric errors of a CMM, at least three-tracking stations are required for multi-lateration measurement method. Using several trackers is not sensible because a laser tracker is an expensive instrument. Moreover, the verification of CMM's working volume is reduced if a large size trackers [(200×200×400) mm] installed inside CMM working space, installing outside a CMM table, a fixed-bridge type CMM cannot be measured by this method, because the target cannot be moved along in one axis.

1.5 Research goals and contributions

1.5.1 Research goals

Verification of the large-sized CMMs is assessed by conventional tools like laser interferometers, artifacts tests. These methods, however, are very time-consuming and do not enable the full analysis of all errors. Artifact-based methods, e.g. based on a series of gauge blocks, a step gauge, a ball plate or a hole plates are limited in their application to small and medium-sized CMMs (measuring volume < 1 m^3). This technique cannot easily be applied to large CMMs, because the artifacts cannot be simply up scaled. They become too heavy and hard to handle. Elasticity and thermal behavior of the artifacts also become critical to maintenance of the gauge accuracy.

Aiming to overcome these problems, a new optical-comb pulsed interferometer method for verification of large-sized CMMs has been proposed. This study focuses on the direct application of the optical frequency comb to standard in length for a medium-sized to large-sized CMM verification. The proposed technique is the absolute-length measurement based on a single-mode fiber optical-comb pulsed interferometer. An optical frequency comb is used as a laser pulsed source, and a fiber etalon is applied to generate the absolute position of the measurement. This work requires using only one target of interferometer, which the measuring system can be applied to measure absolute lengths in all directions of the measurement setup. Truly speaking, the research plan will apply more than one measuring system on the CMM calibration with a target of interferometer in future. General targets of interferometer such as a flat mirror, a cube mirror, or a rough surface are one-directional target, while a cat's eye retroreflector provides a limited angle of the observation as shown in **Fig.1.12**. Hence, the spherical targets of interferometer are considered in this thesis.
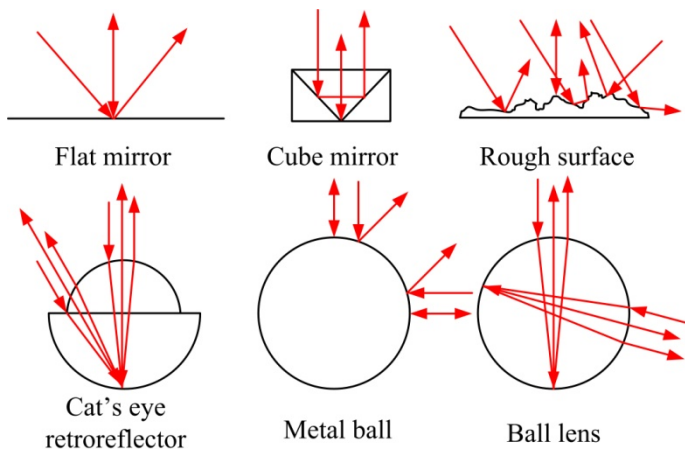
Fig. 1.12 Incidence and reflection of the laser beam on different targets.

In addition, the measuring range is expected up to 10 m, which covers the measuring range of a medium-sized to large-sized CMMs. The accuracy of the proposed measuring system must be accepted within the maximum permissible error of CMM specification, the accuracy ratio is following the requirements of the ISO 10012:2003 [19]. The expecting specifications of a measuring machine in this research are summarized in **Table 1.2.**

Table 1.2 Summary of the expecting specifications of a measuring machine.

Categories	Goals
Main propose	Application for CMM verification
CMMs target	Medium-sized to large-size CMM
Measurand	Absolute length
Measurement method	Pulsed interferometer
Interferometer type	A single-mode fiber optical-comb pulsed interferometer
Target of interferometer	Spherical target
Measuring range	Up to 10 m
Measurement accuracy	Better than 1 μm/m
Resolution	~10 nm
Stability	~50 nm/1h
Traceability	International Standard or SI base unit

1.5.2 Research contributions

The reverification and acceptance tests of CMM should be measured following the requirements of National Standard or International Standard. The main tests of CMM are detailed in the ISO 10360-2:2009. This standard proposes the tests by artifact methods or continuous-wave laser interferometer techniques. However, previous researches based on this standard have some limitations as mentioned in **Section 1.4.1–1.4.3**.

This research presents a new optical measurement method of CMM verification based on the temporal coherence interferometry of the optical frequency comb. The absolute-length measurements are successfully implemented by the first combination of a single-mode fiber optical-comb pulsed interferometer and a ball lens target. The required lengths or absolute positions are controlled by a fiber etalon that is used to modify the repetition frequency of an optical frequency comb. The optical frequency comb directly traces through the rubidium frequency standard to the base SI unit, and a ball lens serves as a three-dimensional target of the interferometer. The principle is original and the experiments were done by the author. Specially, the peak detection method of envelope interference fringe and the automatic

measurement was developed for practical real-time applications. The proposed measuring technique was compared with the conventional standard step gauge method. The result is that the measurement procedure is simply and less time consumption. It has a high efficiency for the medium-sized to large-sized CMM verification, long-measuring range up to 10 m with a small measurement uncertainty due to less effect by surrounding conditions. In addition, the first complete set of the absolute-length measuring machine has been established. Consequently, this research is not limited for only CMM verification, but also can be applied to other absolute-length measurements in dimensional metrology, which performed as a non-contact measurement. Furthermore, this study provides background knowledge for development of the calibration system using the single-mode fiber optical-comb pulsed interferometers, which is able to identify 21 parametric errors of a CMM based on multi-lateration measurement method. The proposed research is therefore intended to make contributions to the literatures on coordinate metrology, and variety on dimensional metrology.

1.5.3 Dissertation contents

Thesis contents on following topic:

Chapter 1 explains about metrological background, standardization, problems of CMM verification based on the conventional methods, and the research goals.

Chapter 2 discusses characteristics of the optical frequency comb, demonstrates a pulsed laser source in terms of frequency and time domain, illustrates light source properties corresponding to the length, principle of pulsed interferometer, and the applications for dimensional metrology.

Chapter 3 demonstrates the absolute-length measurement based on a single-mode fiber optical-comb pulsed interferometer, introduces properties of Fabry-Pérot fiber etalon which plays an important role of absolute position in the measurement, and demonstrates the measurement accuracy and stability of the proposed measuring system.

Chapter 4 presents the positioning accuracy of a CMM verification based on a single-mode fiber optical-comb pulsed interferometer, which a rough metal ball is used as the target. The measurement is compared with the conventional continuous-wave laser interferometer. Experimental measurements demonstrate the effect of absolute-length measurement due to the targets, and the measurement uncertainties are discussed.

Chapter 5 presents the ball lens, which is a new target of interferometer, shows affecting of the target to accuracy of the measurement, and demonstrates efficiency with unique advantages of a long measurement range up to 9 m. Then, the diagonals in space

verification of a CMM are measured by the proposed technique comparing with the conventional standard step gauge method. The uncertainty of both measurement methods are evaluated and discussed. In addition, the effectiveness of the proposed method and validation of uncertainty claim are demonstrated.

Chapter 6 suggests the accuracy improvement of absolute-length measurement based on the proposed method. Measuring machine prototype has been established. It can be applied to measure absolute lengths of CMM, and other absolute-length measurements in dimensional field, which performed as a non-contact measurement. The design of measuring system is analyzed. In addition, Optical components of measuring machine prototype and the developing measurement software are explained. Furthermore, the basic performances of measuring machine prototype have been determined and the measurement accuracy is estimated and discussed.

Chapter 7 is the overall thesis summary and discussion. The main advantages of the proposed method and applications are indicated. In contrast, some problems and solutions during experimental measurements are discussed. Moreover, this chapter introduces about future work that will be applied for CMM calibration system, which is able to identify 21 parametric errors of a CMM based on multi-lateration measurement method. The discussion provides background and the concept idea state how to conduct, and what requirement of next step research is.

Appendix contains the simulation codes and the programming codes, which had been used for demonstrations and experimental measurements in this thesis.

Chapter 2 Optical frequency comb

2.1 Introduction

What is an optical frequency comb, and how to construct the single-mode fiber optical-comb pulsed interferometer is explained in this chapter. However, this chapter discusses the important characteristic properties of an optical frequency comb for constructing a single-mode fiber optical-comb pulsed interferometer rather than producing the optical frequency comb synthesizer.

To begin with the principle of pulsed laser and mode-locking laser technique, which are the most important technique and most commonly-employed technique of an optical frequency comb, are explained. The characteristics of an optical frequency comb in the time domain and frequency domain are described. Subsequently, the C-fiber femtosecond laser is an optical frequency comb, which is used as a laser pulsed source in this research, is introduced. Then, some researches and applications of the optical frequency comb for dimensional metrology are reviewed. Two efficient methods are regularly used for absolute-length measurement by the optical frequency comb. There are based on the temporal coherence interferometry and the optoelectronic phase-shifting method. Both methods have several techniques for achieving absolute-length measurements, which are discussed. Finally, the constructing diagram of an optical-comb pulsed interferometer based on a single-mode fiber type is explained. Additionally, in order to achieve a high accuracy of the measurement, the compensation of the group refractive index of air due to the variation of environmental conditions for absolute-length measurement is discussed.

2.2 Pulsed lasers

The simplest method of obtaining pulsed light from a laser is to use a continuous-wave (cw) laser in conjunction with an external switch or modulator that transmits the light only during short time intervals. By this simple method, the peak power of the pulses cannot exceed the steady power of the cw source. In pulsed laser operation, many effective techniques for internal modulation of laser light such as Gain switching, Q-switching, and Mode locking have been proposed [20–23]. Gain switching is used to generate very short laser pulses through the control of oscillator transients. For the concept of gain switching, the gain parameter of a laser is switched on rapidly above the laser threshold, which is defined by the loss parameter, by fast, pulsed pumping so that a very short laser pulse is generated through the transient effects of the laser oscillator. Subsequently, Q-switching is the most widely used technique for the generation of high-intensity giant laser pulses of short duration. Q-switching relies on the transient dynamics of a laser to generate very short pulses. However, it does not require extremely fast pumping, as does the technique of gain switching. It is possible to pump the gain medium continuously while switching the cavity Q factor repetitively to generate a periodic train of Q-switched pulses. The principle of Q-switching is based on delaying the onset of laser oscillation relative to the start of pumping to accumulate a large population inversion. This task is accomplished by reducing the laser cavity Q factor in the early stage of pumping to exclude the depletion of population inversion caused by premature laser oscillation. Next, in mode locking technique, pulsed laser action is attained by coupling together the modes of a laser and locking their phases to each other. They behave like the Fourier components of a periodic function, and therefore form a periodic pulse train when the phases of these components are locked together. The coupling of the modes is achieved by periodically modulating the losses inside the cavity.

For pulsed operation methods, depending on the laser material, the cavity design, and the technique employed for the pulsed operation, laser pulses of temporal pulse widths ranging from the order of microseconds to the order of femtoseconds with large ranges of pulse repetition rates, from single shots to gigahertz. Mode locking technique is the most important technique and most commonly-employed techniques for the generation of repetitive ultrashort laser pulse. Therefore, here only the basic principle of the mode locking laser will be discussed.

2.3 Introduction to mode-locked laser

Mode locking technique refers to the situation when all of the oscillating longitudinal modes of a laser are locked in phase. When this situation is happened, constructive interference of all of the oscillating modes inside the cavity is amplified by the gain medium after periodically, delivering an output pulse through an output-coupling mirror in each round trip. The mode-locking operation is accomplished by a nonlinear optical element that is placed inside the laser cavity, typically near one end of the cavity if the laser has the configuration of a linear cavity [21].

The simplest case consideration of multimode oscillation inside the cavity, supposing there are only two oscillating longitudinal modes of frequencies ω_1 and ω_2 as:

$$E_1(t) = E_1 \cos[(\omega_1 t + \varphi_1(t)], \quad E_2(t) = E_2 \cos[(\omega_2 t + \varphi_2(t)] \tag{2.1}$$

where E_1 and E_2 are the amplitudes, and φ_1 and φ_2 are the phases.

Therefore, the output of the laser will only react to the intensity I of the field. That is the square of the total electric field amplitude as $I(t) \propto |E(t)|^2$:

$$I = E_1^2 \cos^2[\omega_1 t + \varphi_1(t)] + E_2^2 \cos^2[\omega_2 t + \varphi_2(t)] + 2E_1 E_2 \cos[\omega_1 t + \varphi_1(t)]\cos[\omega_2 t + \varphi_2(t)] \tag{2.2}$$

In practice, the detector will respond with a signal proportional to the mean value of the intensity I over the time respond of the detector (τ_D). Therefore, the observed intensity of the laser will become:

$$\langle I \rangle = \frac{E_1^2}{2} + \frac{E_2^2}{2} + \frac{E_1 E_2}{\tau_D} \int_0^{\tau_D} \cos[(\omega_1 - \omega_2)t + \varphi_1(t) - \varphi_2(t)]dt \tag{2.3}$$

The first two terms of **Eq. (2.3)** correspond to the intensity of each of the modes taken separately. The third term states the beating between the two modes.

If the phase factors $\varphi_1(t)$ and $\varphi_2(t)$ vary randomly with time on a characteristic time scale that is shorter than $2\pi/(\omega_1 - \omega_2)$, the beat note of the two frequencies cannot be observed even with a very fast detector. This situation the output of the laser has a constant intensity that is the incoherent sum of the intensities of the individual modes, and it simply represents the ordinary multimode oscillation of a cw laser.

On the other hand, if the phase factors are totally correlated so that $\varphi_1(t) - \varphi_2(t) = 0$, the laser intensity becomes periodically modulated with a period of $2\pi/(\omega_1 - \omega_2)$ defined by the

beat frequency. This is simply coherent mode beating. If the number of modes that are locked in phase increases, the characteristics of periodic pulses become increasingly apparent in the output of the laser, as demonstrated in **Fig. 2.1** (MATLAB simulation code can be found in **Appendix, Fig. A1**). This simulation shows thirty sinusoidal modes are fixed and random phase orientations. As a result, only the mode-locked relationship yields pulses output.
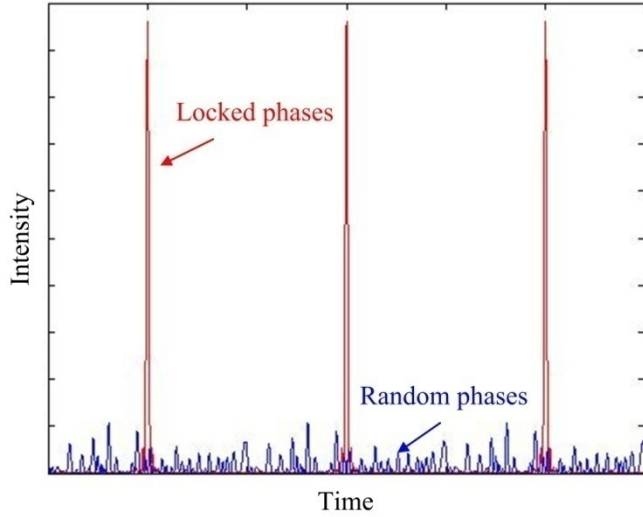
Fig.2.1 Thirty sinusoidal modes of the simulation are fixed and random phase orientations.

Subsequently, the case of $2q + 1$ longitudinal modes oscillating with the same amplitude E_0, and assumed the phases of the modes in the output beam to be locked according to the relation of $\varphi_n - \varphi_{n-1} = \varphi = constant$, and assumed to be zero. The result is that the total electric field $E(t)$ can be written as:

$$E(t) = \sum_{-q}^{+q} E_0 \exp[i(\omega_0 + q\Delta\omega)t] \tag{2.4}$$

where ω_0 is the frequency of the central mode, $\Delta\omega$ is the frequency difference between two adjacent modes. Therefore, $E(t)$ can be transformed as:

$$E(t) = A(t)\exp(i\omega_0 t) \tag{2.5}$$

where $A(t) = \sum_{-q}^{+q} E_0 \exp[i(q\Delta\omega)t]$.

Thus, $E(t)$ can be represented in terms of a sinusoidal carrier wave, at the center-mode frequency ω_0, whose amplitude $A(t)$ is time dependent. The sum appearing in the right-hand

23

side of $A(t)$ can be easily recognized as a geometric progression with a ratio $\exp i(\Delta\omega t)$ between consecutive terms. Summation of this progression can then be performed and be written:

$$A(t) = E_0 \frac{\sin\left[(2q+1)\Delta\omega t/2\right]}{\sin\left[\Delta\omega t/2\right]} \qquad (2.6)$$

The temporal characteristics of this field depend on the phase relationships among the oscillating modes, as well as on the distribution of the field magnitudes $A(t)$ and the frequency spacing between neighboring modes. Ordinarily, the spectral envelope is expected to have a bell-shaped form, the amplitude E_q of the q-th mode as an envelope with a Gaussian distribution is considered:

$$E_q = E_0 \exp\left[-\left(\frac{2q\Delta\omega}{\Delta\omega_L}\right)^2 \ln 2\right] \qquad (2.7)$$

where $\Delta\omega_L$ represents the bandwidth (FWHM, the total width at the haft maximum of the total field distribution) of the spectral intensity. Here, if the sum of $A(t)$ is approximated by an integral, the field amplitude $A(t)$ is seen to be proportional to the Fourier transform of the spectral amplitude E_q. Thus, $A^2(t)$, the pulse intensity, is a Gaussian function of time, which can be written as:

$$A^2(t)\alpha \exp\left[-\left(\frac{2t}{\Delta\tau_p}\right)^2 \ln 2\right] \qquad (2.8)$$

where $\Delta\tau_p = 2\ln 2/\pi\Delta\upsilon_L$, and represents the width (FWHM) of the pulse intensity. The Fourier series of this function shows a real-valued periodic function with period $T = 2\pi/\Delta\omega = 2L/c$. Here L is the cavity length and c is the speed of light in vacuum. For that reason, the laser intensity is also periodic.

Fig. 2.2 is the summary of time behavior of the squared amplitude of the electric field for the case of M oscillating modes with locked phases and equal amplitudes, and the summary of characteristic properties of a mode-locked pulse train is shown in **Table 2.1**, the simplest diagram of a mode-locked laser is shown in **Fig. 2.3**, respectively.
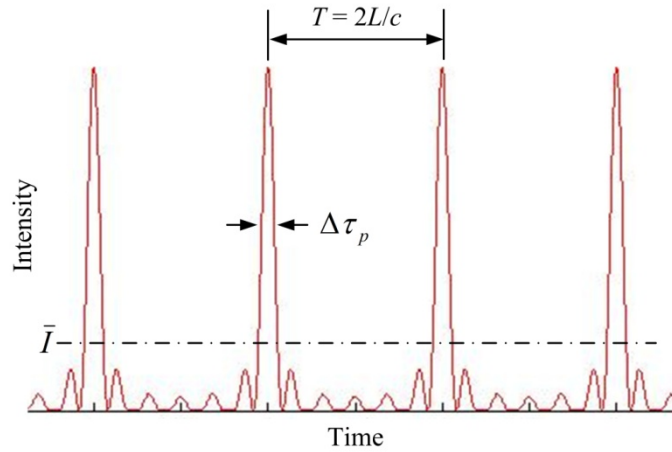
Fig. 2.2 Intensity of periodic pulse train resulting from sum of M laser modes of equal magnitudes and phase. Each pulse has a width that is M times smaller than the period T and a peak intensity that is M times greater than the mean intensity $\bar{I}$.

Table 2.1 Characteristic properties of a mode-locked pulsed train [20]

Properties	Parameters
Temporal period	$T = 2L/c$
Pulse width	$\Delta\tau_p = T/M$
Spatial period	$2L$
Pulse length	$c\Delta\tau_p = 2L/M$
Mean intensity	$\bar{I} = M|A|^2$
Peak intensity	$M\bar{I}$
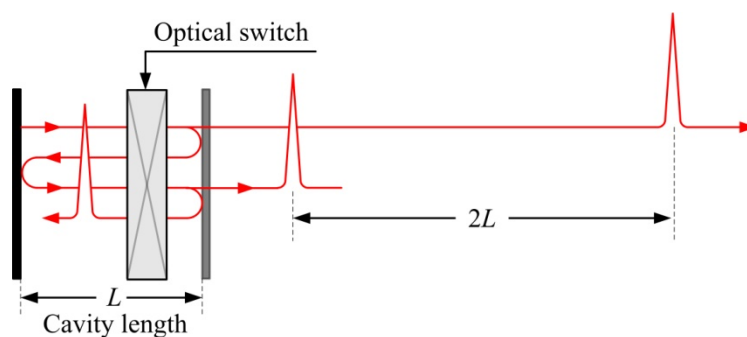
Fig. 2.3 Simple diagram of mode-locked laser: laser pulse reflects back and forth between the mirrors of the resonator. Each time it reaches the output mirror, and transmits a short optical pulse. The transmitted pulses are separated by the distance $2L$ and travel with velocity c.

25

2.4 Time and frequency domain pictures of an optical comb

An optical frequency comb, optical comb, or comb is an optical spectrum which consists of equidistant frequency lines. It is employed by mode-locked laser method that is mentioned in **Section 2.3.** The pulse train creates a spectrum consisting of narrow spikes at integer multiples of the repetition rate of the laser. This spectrum is called a frequency "comb" because it resembles a hair comb. An optical comb can be described by two measurable parameters, which are the repetition rate and the carrier-offset frequency. A repetition rate refers to equally spacing between longitudinal modes, which is determined by the laser cavity length. Other is a carrier-offset frequency that is caused by dispersion in the cavity. Under stabilization of the repetition rate and a carrier-offset frequency, longitudinal modes are able to be employed as a scale on the optical frequency ruler with the traceability to the frequency standard, cesium atomic clock [24–27].

The following section is discussion of the optical comb properties, specially the carrier-envelope phase. This phase is based on the decomposition of an ultrashort pulse into an envelope function $A(t)$, which is explained in **Section 2.3**. The envelope function is superimposed on a continuous carrier wave with frequency ω_0, so that the electric field of the pulse is written as $E(t) = A(t)\exp(i\omega_0 t)$. The carrier-envelope phase, $\Delta\varphi$, is the phase shift between the peak of the envelope and the closest peak of the carrier wave. In any dispersive material, the difference between group and phase velocities will cause $\Delta\varphi$ to evolve as the pulse propagates. If we just consider a single pulse as shown in the right-hand side of **Fig 2.4 (a)**, it will have a power spectrum that is the Fourier transform of its envelope function, and is centered at the optical frequency of its carrier. Generally, for any pulse shape, the frequency width of the spectrum will be inversely proportional to the temporal width of the envelope. For a train of identical pulses, separated by a fixed interval, the spectrum can easily be obtained by a Fourier series expansion. The result is that a comb of regularly spaced frequencies, where the comb spacing is inversely proportional to the time between pulses. Thus, when $\Delta\varphi$ is evolving with time, a rigid shift will occur for the frequencies at which the pulses add constructively. This shift is determined to be $(1/2\pi)\,\Delta\varphi\,/T$.

For the time domain, the pulse train is emitted as the same period by mode-locked laser as illustrated in **Fig.2.4 (a)**, which the pulse-to-pulse is separated by $1/f_{rep}$, where f_{rep} is the repetition frequency of the optical frequency comb. The pulse-to-pulse states in the phase of pulses emitted by the mode-locked laser due to the phase and group velocities inside the laser cavity are different, and can be expressed in terms of the average phase (v_p) and group (v_g) velocities inside the cavity. Specifically, $\Delta\varphi = (1/v_g - 1/v_p)l_c\omega_c$, where l_c is the round-trip length of the laser cavity and ω_c is the carrier frequency.

For the frequency domain, each shape lines are separated equally. The optical frequencies f_m of the comb lines is described as $f_m = mf_{rep} + f_0$ where m is a large integer of order 10^6 and f_0 is the offset frequency due to pulse-to-pulse phase shift. The comb offset is connected to the pulse-to-pulse phase shift by $f_0 = (1/2\pi) f_{rep} \Delta\varphi$.
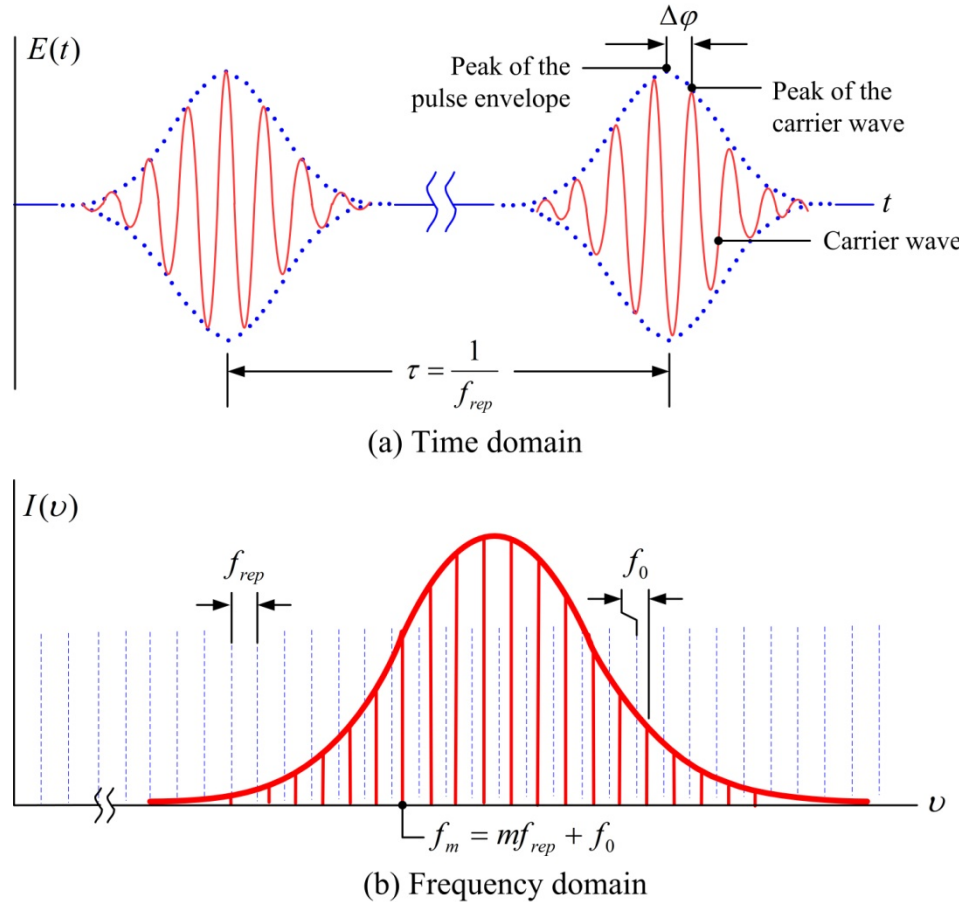
Fig. 2.4 The time and frequency domain properties of an optical comb.

Both f_{rep} and f_0 depend on conditions inside the laser cavity, and a stabilized comb refers to one in which both f_{rep} and f_0 can be determined and controlled. The stabilization of these two frequencies means the stabilization of every optical mode in the comb.

2.5 C-fiber femtosecond laser

The laser source which has been used in this research is a C-fiber femtosecond laser from MenloSystems that integrates latest achievements in fiber technology into an easy to use for various applications. This laser is a mode-locked Erbium doped fiber laser. It is driven by a passively mode-locked fiber ring laser with a central wavelength of 1560 nm. The Er^{3+} doped silica fiber is used as gain medium instead of a laser crystal. The microcontroller driven actuators built into the fiber ring start and maintain stable mode locking automatically. **Fig. 2.5** shows an optical comb system and **Table 2.2** lists technical data specifications of this laser.
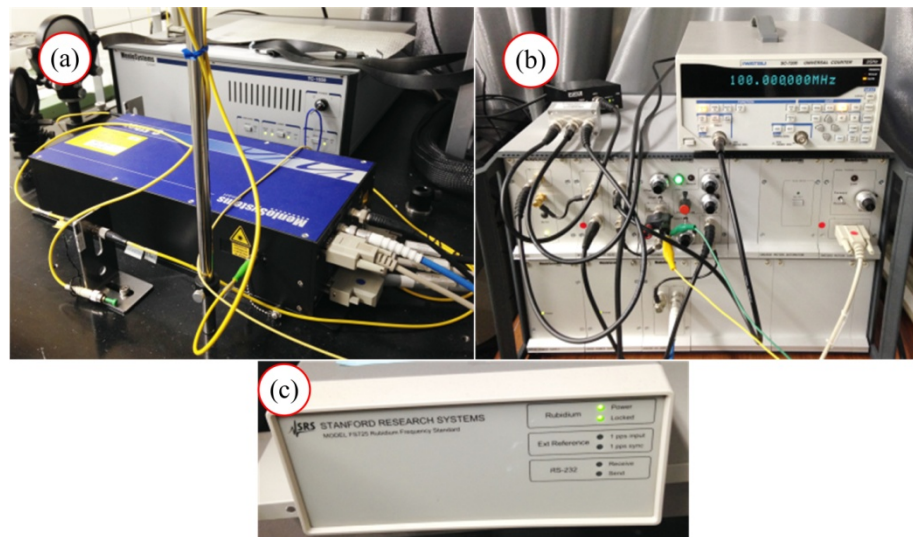
Fig. 2.5 C-fiber femtosecond laser from MenloSystems: (a) is a laser head and a control unit, (b) is a repetition rate stabilization controller and a frequency counter monitor, and (c) is a rubidium frequency standard.

Table 2.2 Technical specifications of C-fiber femtosecond laser

Parameter	Technical data
Central wavelength	1560 nm
Repetition rate	100 MHz
Repetition rate instability	< 1 ppm
Output power	(17.9, 17.5, 18.4) mW[*]
Pulse width	< 150 fs
Spectral width	(58.9, 59.9, 60.5) nm[*]

[*] For output port A, C, and F, respectively.

According to technical data of the C-fiber femtosecond laser, the pulse train properties corresponding to the length scale can be explained as **Fig.2.6**. The laser pulse width of less than 150 fs corresponding to the length scale is approximately 44.96 μm. The laser pulses are equally separated approximately 3 m.
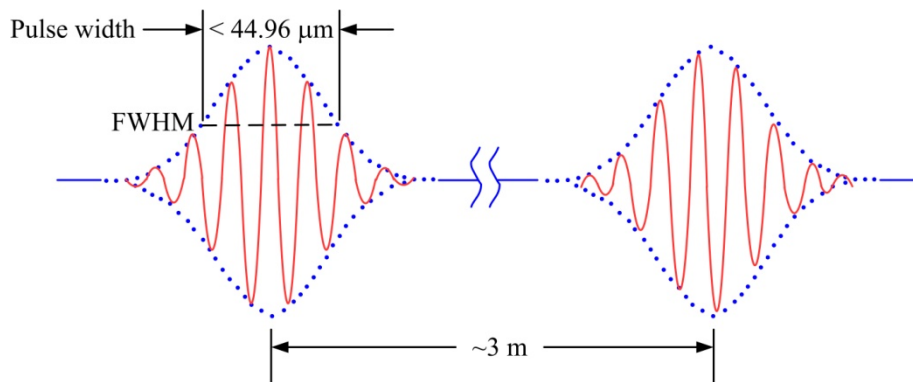
Fig. 2.6 Pulse train properties of the C-fiber femtosecond laser corresponding to the length.
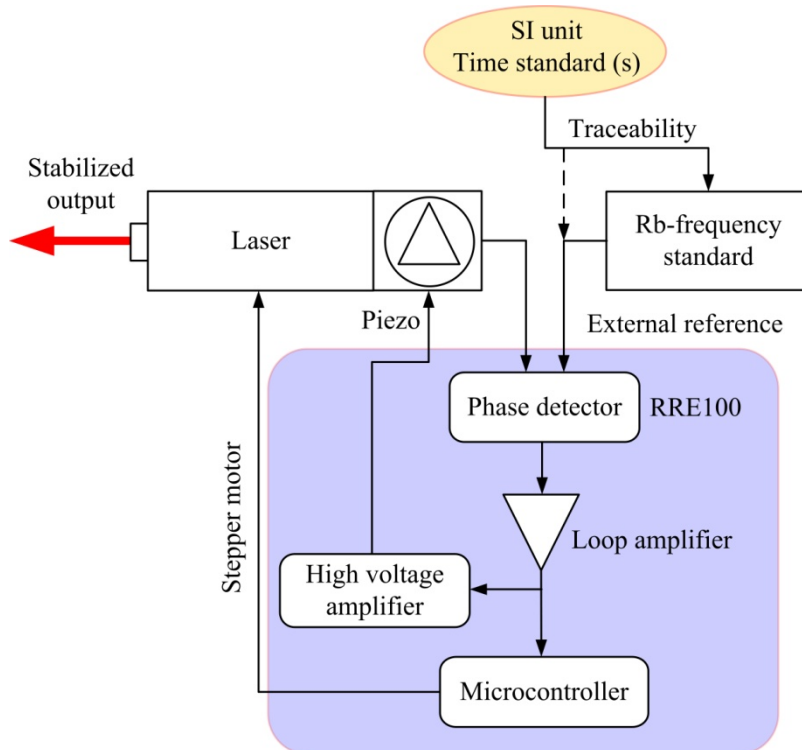
Fig. 2.7 Stabilized repetition rate diagram of C-fiber femtosecond, the repetition frequency of the laser is stabilized by a 10 MHz reference signal from Rb-frequency standard (FS725).

(*Figure was redrawn from manual of C-fiber femtosecond*)

The C-fiber femtosecond laser has three main components as shown in **Fig. 2.5**: (a) is a laser head and a control unit, (b) is a repetition rate stabilization controller (RRE100) and a frequency counter monitor (IWATSU SC-7206), and (c) is a rubidium frequency standard (FS725).

The stabilized repetition rate diagram of C-fiber femtosecond laser is illustrated in **Fig. 2.7**. The RRE100 is used to synchronize the repetition rate of a pulsed laser source to an external reference frequency source (Rb-frequency standard FS725, Stanford research system). The reference frequency can be derived from a radio frequency clock or from the repetition rate signal of another pulsed laser source. From stabilized diagram, the Rb-frequency standard and repetition rate signal of the pulsed laser are compared and detected by a phase detector. The phase signal is detected by mixing a harmonic of the repetition signal with a reference frequency signal. The result is that a phase detector generates the error signal for a loop amplifier unit. The fast feedback signal of the loop amplifier is amplified to a high voltage and feedback to a fast piezo actuator mounted below one end mirror of the pulsed laser source. Slow drifts of the repetition rate are compensated by a microcontroller driven stepper motor unit. By this close-loop control, the stability of the repetition frequency is stabilized better than order of $\sim 10^{-11}$.

2.6 Optical comb applications for dimensional metrology

Since the Nobel Prize in Physics was awarded to John L. Hall and Theodor W. Hänsch in 2005 "*for their contributions to the development of laser-based precision spectroscopy, including the optical frequency comb technique*", the use of femtosecond pulse lasers has been dramatically exploded because of its wide spectral bandwidth, short pulse duration, high frequency stability and ultra-strong peak power in precision spectroscopy, time-resolved measurement, and micro/nano fabrication [25]. The femtosecond pulse laser has more than $10^5 \sim 10^8$ longitudinal modes in the wide spectral bandwidth of several hundred nanometers in wavelength. Under stabilization of the repetition rate and a carrier-offset frequency, longitudinal modes are able to be employed as a scale on the optical frequency ruler with the traceability to the frequency standard, cesium atomic clock. For that reason, many precise-length measurements based on optical comb have been developed. An optical frequency comb can be directly used for absolute measurement not only of frequency levels [25–28] but also of various distances [29–38].
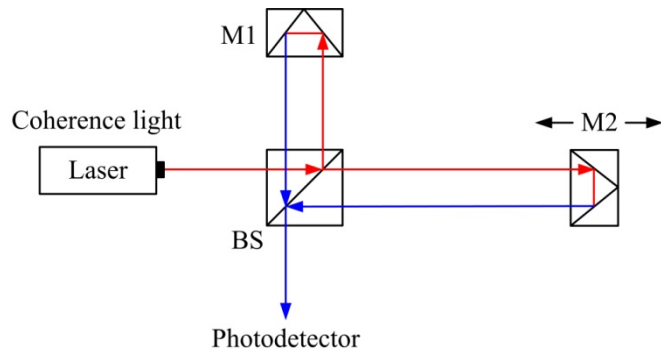
Fig. 2.8 Relative displacement measurement based on principle of Michelson interferometer: BS is a beam splitter, M1 is a reference mirror that is fixed, and M2 is a target mirror.

General optical interference is the superposition of two or more lights that result produces interference fringes, which depends on the optical path differences of the light rays. Michelson interferometer is the most well known optical diagram as shown in **Fig. 2.8**, used in precision dimensional metrology. When the optical path difference is changed by moving the mirror target (M2), it is shown the periodic interference fringe pattern. The pattern fringe relates to the degree of coherence of a light source. Therefore, the optical path difference can be determined within less than a half wavelength uniquely. Since the interference fringe pattern is very sensitive to the optical path difference, the displacement can be determined with sub-wavelength resolution. In the measurements, the interference patterns are counted

continuously during the motion of the target mirror. This relative displacement measurement technique is one of the most precise metrological tools. However, it has practical difficulties in the long-range measurement or large step measurement because the target mirror should be installed for translating from the initial position to the final position continuously without any interruption. Moreover, for the long-distance measurements, the accuracy of the interferometer is affected by air turbulence and mechanical vibration, and therefore, is not easy to apply.

On the other hand, an optical frequency comb can be directly used as the light source of a long-path interferometer, and this has prompted various research efforts to develop new distance measurement devices [29–38]. Optical frequency combs have a strong potential for use in interferometry because they are characterized by pulse-repetition frequencies that are traceable to the definition of second (SI base unit of time) with a high accuracy. Two efficient methods are regularly used for absolute-length measurement by the optical frequency comb. There are based on the temporal coherence interferometry and the phase measurement. Several techniques are applied for achieving absolute length from both methods. Based on the temporal coherence interferometry, the heterodyne interferometer with an optical frequency comb has been proposed [30–33]. This method used the acousto-optic modulator (AOM) for generating a frequency shift in the beam of the reference arm of the interferometer. Temporal coherence interference fringe occurs at discrete spatial positions, when two pulse trains overlap. The lengths are measured by determining the relationship between time intervals and scanning length of a piezoelectric transducer when interference fringes are appeared. However, the absolute lengths are measured by each step length of 1.5 m corresponding to the repetition frequency of laser source (100 MHz). Based on the phase measurement by beating frequency, the femtosecond distance meters have been proposed [29, 34–36], because wide-ranging frequency components up to high frequencies can easily be utilized for the measurements. By the evaluation of the phase shifts of two distinct comb frequencies, a coarse measurement and a fine measurement of the absolute distance can be performed [37]. This technique leads to development of the electronic distance measurement system based on a time-of-flight approach, driven by a femtosecond laser source as a modulator. However, the length measurement based on phase information is always affected by noise of the electronic components, which leading to the accuracy improvement is difficult and complex of the measurement system. In addition, high frequency is required for high resolution because the phase resolution generally limits the measurement and higher frequency results in a smaller distance for the same phase value. Therefore, selectable frequency is required to determine the absolute distance without continuous scanning.

This research conduct the measuring system based on the temporal coherence interferometry, which an unbalanced optical-path Michelson interferometer is applied as shown in **Fig. 2.9**. The pulsed laser is divided by a beam splitter (non-polarization) and the reference beam passes through a delay path in which the beam is scanned up to 250 μm with the piezoelectric transducer (PZT) or over 5 mm with the voice coil actuator or other scanning devices. The beam is reflected at two positions by a reference mirror (the zero-path position, $OPD = 0$) and the target mirror. Finally, these beams are recombined with the scanning beam to produce interference fringes, and detected by a photodetector. Unlike Michelson interferometer, the interference fringes are generated only when the distance between the zero path and target positions is equal to $mc/2n_{air}f_{rep}$, where m is an integer (interference fringe order), c is the speed of light in vacuum, n_{air} is the refractive index of air and f_{rep} is the repetition frequency of the laser source. The optical frequency comb is practical use when conducting the absolute-length measurements as a pulsed interferometer, because it is less influenced by the surrounding conditions when applying with optical fiber communications.
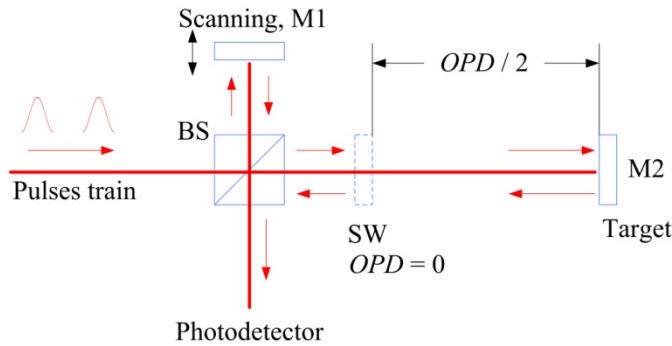
Fig. 2.9 Absolute position measurement based on optical-comb pulsed interferometer: BS is beam splitter, M1 is a scan mirror which is fixed on a linear scanning device, SW is a sapphire window plate or a semi-permissible mirror, which is placed at the reference position and M2 is a target mirror.

2.7 Optical comb pulsed interferometer

The absolute length based on an optical-comb pulsed interferometer can easily be composed by using single-mode optical fibers. So that is called a single-mode fiber optical-comb pulsed interferometer. In applications, it is constructed as a diagram shown in **Fig. 2.10**. The optical frequency comb generates pulsed laser, which the laser pulses pass through an optical fiber circulator (CIR), are divided into two beams by a non-polarization optical fiber beam splitter (FBS). One beam is transmitted in the direction of a scanning mirror (M1) for scan interference fringes over displacement, while other is transmitted passing a reference position (SW) to the target mirror (M2).
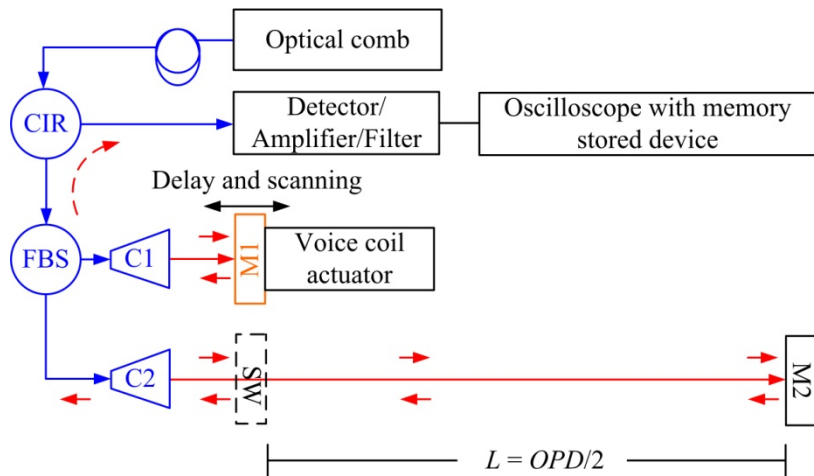
Fig. 2.10 The single-mode fiber optical-comb pulsed interferometer: CIR is an optical fiber circulator, FBS is a fiber beam splitter, C1 and C2 are collimators, SW is a sapphire window plate ($OPD = 0$), and M1 and M2 are scanning mirror and target mirror.
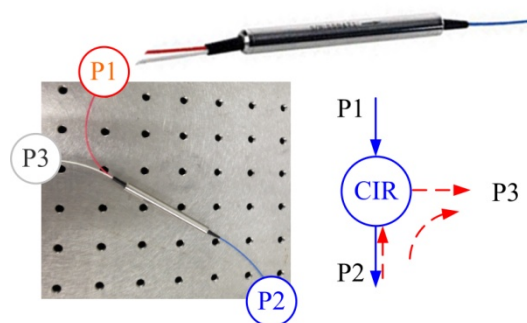
Fig. 2.11 The optical fiber circulator: P1, P2, and P3 are the port number.

Subsequently, the returned beams from the SW and the M2 recombine with the beams that are reflected from the scanning mirror to produce interference fringes. These fringes pass through the CIR again to the output port of P3, and are detected by a photodetector. Here, an optical circulator is a three-port device that allows light to travel in only one direction as shown in **Fig. 2.11**. The light pulse signal entering from P1 will exit to P2 with minimal loss. Alternatively, the light pulse signal entering from P2 will exit to P3 with minimal loss.

The optical-comb pulsed interferometer involves with the temporal interference pattern fringe. The controllable repetition frequency is a key for practical length applications of a pulsed interferometer. So, the interference fringe will occur only when the pulses of two arms overlap, and the optical path difference (*OPD*) of the two arms is satisfied as following conditions:

$$OPD = \frac{mc}{n_{air} f_{rep}} \tag{2.9}$$

where m is an integer, c is the speed of light in vacuum, n_{air} is refractive index of air, and f_{rep} is the repetition frequency. Therefore, the absolute length under measurement is a haft of the optical path difference, and is reversely proportional to the repetition frequency as shown in **Table 2.3.**

Table 2.3 Relationship of the optical path differences and the repetition frequencies

Repetition frequency (f_{rep})	$L = OPD/2$
100 MHz	1.5 m
1 GHz	150 mm
2 GHz	75 mm
3 GHz	50 mm

* The relationship of the repetition frequencies and the optical path differences in **Table 2.3** are assumed based on the parameters of $c = 3 \times 10^8$ m/s, and the refractive index of air is assumed to exactly be 1.

2.8 Refractive index of air and compensation

For the optical-comb pulsed interferometer, the optical path difference is inversely proportional to the repetition frequency as described in **Eq. 2.9**. In addition, it also relates to the refractive index of air that is not exactly equal to 1 under real-measurement conditions. Therefore, the speed of light will be reduced due to the refractive index of the medium. In order to archive a high accuracy of the measurement, the optical path lengths have to be compensated by the index of the refraction of air.

Demonstrable equations for refractive index of air were derived from the experimental data obtained by Edlén, Ciddor, Downs, and another researches [39–47]. These equations are often determined from the physical parameters of the atmosphere such as air temperature, air pressure, air humidity, and CO_2 gas content. These values are acquired from sensors with high accuracy. For length measurements, many electronic distance-measuring instruments, use intensity-modulated light or pulsed light, and therefore require a precise of the group refractive index, rather than the phase refractive index in order to acquire high accuracy of the measurement, including an optical-comb pulsed interferometer [39–44]. General the group refractive index of air is analytically derived from the empirical equations of the phase refractive index. The group index for any component under standard conditions is found by replacement of the corresponding standard phase index by **Eq. 2.10**.

$$n_g = \sigma \left(\frac{dn_p}{d\sigma} \right) \tag{2.10}$$

where n_p is phase index, σ is wave number, and the following results become:

$$(n_g - 1) = \left(\frac{\rho_a}{\rho_{axs}} \right)(n_{gaxs} - 1) + \left(\frac{\rho_w}{\rho_{ws}} \right)(n_{gws} - 1) \tag{2.11}$$

where ρ_{axs} is the density of dry air, and ρ_{ws} is the density of pure water vapor at the standard conditions, while ρ_a and ρ_{ws} are the densities of the dry air component and the water vapor component of moist air for the actual measurement conditions. The values of (n_{gaxs}-1) and (n_{gws}-1) are determined from **Eq. (2.12)** and **Eq. (2.13)**, respectively.

$$10^8 (n_{gaxs} - 1) = \left[\frac{k_1(k_0 + \sigma^2)}{(k_0 - \sigma^2)^2} + \frac{k_3(k_2 + \sigma^2)}{(k_2 - \sigma^2)^2} \right] \times \left[1 + 0.534 \times 10^{-6}(x_c - 450) \right] \tag{2.12}$$

$$10^8(n_{gws} - 1) = cf\left[w_0 + 3w_1\sigma^2 + 5w_2\sigma^4 + 7w_3\sigma^6\right] \qquad (2.13)$$

The standard constants in **Eq. (2.12)** and **Eq. (2.13)** are list in the **Ref. [39]**. Some parts of the group refractive index of air in the laboratory during experiment are show in **Table 2.4**.

Table 2.4 Air conditions and group refractive indices of air in the laboratory

Date	Air temperature (°C)	Air humidity (%RH)	Air pressure (kPa)	n_g
13-Dec-13	19.3	24.8	101.13	1.00026976
27-Dec-13	18.9	29.5	99.20	1.00026493
9-Jan-14	20.9	24.4	100.20	1.00026580
13-Jan-14	19.1	21.4	101.11	1.00026992
14-Feb-14	24.3	27.3	99.36	1.00026047
14-Mar-14	21.9	17.7	100.29	1.00026519
27-Mar-14	23.6	30.5	100.34	1.00026364
2-Apr-14	23.3	25.1	101.23	1.00026632
8-Apr-14	22.0	27.5	100.22	1.00026482
28-May-14	20.7	39.3	98.70	1.00026186
2-Jun-14	24.6	41.2	100.70	1.00026356
22-Jun-14	21.9	52.7	100.13	1.00026443
14-Jul-14	23.3	49.1	100.29	1.00026359
11-Aug-14	22.6	45.3	99.59	1.00026243
22-Oct-14	24.4	48.6	100.61	1.00026343
6-Nov-14	23.3	48.7	101.08	1.00026568
15-Mar-15	21.8	22.9	101.28	1.00026785

*Note that the laboratory is not controlled. The environmental conditions are varying due to open the air conditioner in summer and heater during winter. The group refractive indices of air are calculated by Ciddor's equation as **Eq. (2.11)**, and assumed that the content of CO_2 is 450 ppm (molar fraction in parts per million). The calculation results in **Table 2.4** indicate that although the laboratory is not controlled, the variations of group refractive index of air due to experimental conditions are in order 10^{-6}. However, the group refractive index of air has to be concerned for the single-mode fiber optical-comb pulsed interferometer.

Chapter 3 Pulsed interferometer and Experiments

3.1 Introduction

This chapter explains principle of absolute-length measurement and demonstrates experimental measurements based on the single-mode fiber optical-comb pulsed interferometer. First, the requirements of mechanical and optical components for the construction of a single-mode fiber optical-comb pulsed interferometer are explained. Measurement setup and optical alignment are significant in order to achieve a perfect interference fringe pattern. Then, fringe patterns are analyzed and discussed for determining the distance of peak-to-peak of envelope interference fringes.

Subsequently, the principle of Fabry–Pérot etalon is provided. The fiber etalon is used as a frequency mode selector for generating the absolute position of requiring absolute distance. The absolute position of interference fringe relates to the free spectral range (FSR) of the etalon, which depends on the cavity length of the fiber etalon. So, an experiment demonstrates the simplest method to measure the cavity length of a fiber etalon. Moreover, the compensation of incomplete fiber etalon cavity is discussed.

Next, experimental measurements based on 1-GHz FSR etalon are discussed. The single-mode fiber optical-comb pulsed interferometer is assembled as the absolute-length measurements. The converting of time scale to the length scale is demonstrated to evaluate peak-to-peak distance of envelope interference fringes.

Finally, the measurement stability and accuracy of the absolute-length measuring system based on the 1-GHz FSR are discussed. Experimental measurements are compared with a commercial continuous-wave laser interferometer, and measurement results are discussed.

3.2 The single-mode fiber optical-comb pulsed interferometer

The pulsed interferometer refers to a temporal coherence interferometry, which the pulsed source is an optical frequency comb as described in **Chapter 2**. The diagram of pulsed interferometer illustrated in **Fig. 2.10** can easily be composed by using optical fibers. Therefore, this interferometer is based on a single-mode fiber type. The following topics are going to explain the composition of a single-mode fiber optical-com pulsed interferometer and demonstration of absolute-length measurement.

3.2.1 Pre-measurement setup and alignment

The single-mode fiber optical-comb pulsed interferometer is based on the operating principle of the unbalanced-arms Michelson interferometer. The first arm of the interferometer is used for delaying or scanning the interference fringe. **Fig.3.1** shows optical and mechanical components of this part.
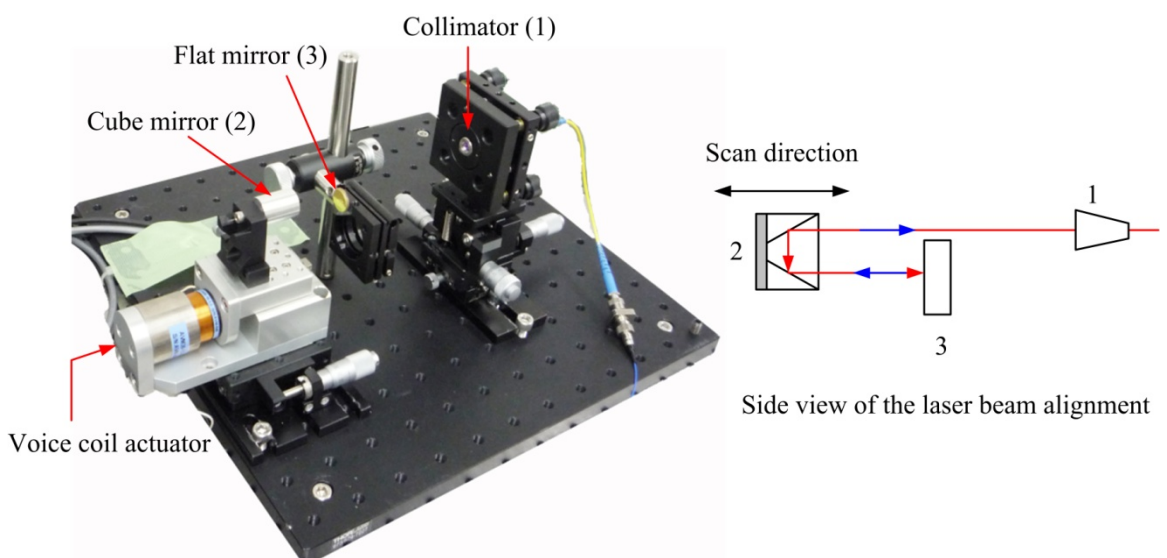
Fig. 3.1 The scanning path of the pulsed interferometer.

The scanning path consists of a collimator (1), a cube mirror (2) which is installed on a scanning device (voice coil actuator), and a flat mirror (3). Voice coil actuator acts as a scanning device and it is always oscillated as the same frequency, which is used to extend and delay optical path difference between two arms of the interferometer. The laser beam that is spitted by a fiber beam splitter (50:50) is connected to a collimator. The collimated beam is aligned to parallel with the scanning direction of a voice coil actuator over the traveling length.

In practice, a flat mirror is used to reduce the motion errors (pitching and yawing) of a voice coil actuator. A flat mirror is adjusted perpendicular to the laser beam that reflected from a cube mirror. The laser beam alignment diagram is explained in the right hand side of **Fig. 3.1**.

Other arm of interferometer is illustrated in **Fig. 3.2**, called the measuring arm. This arm consists of a collimator (1), a semi-permeable mirror or a sapphire mirror (2), and a target mirror (3). The laser beam which split by a fiber beam splitter is collimated by a collimator. Then, a semi-permeable is placed in front of a collimator for setting as a reference position (this position $OPD = 0$). A target mirror is placed far away from a semi-permeable mirror approximately 1.5 m. Both mirrors are aligned perpendicular to the laser beam.
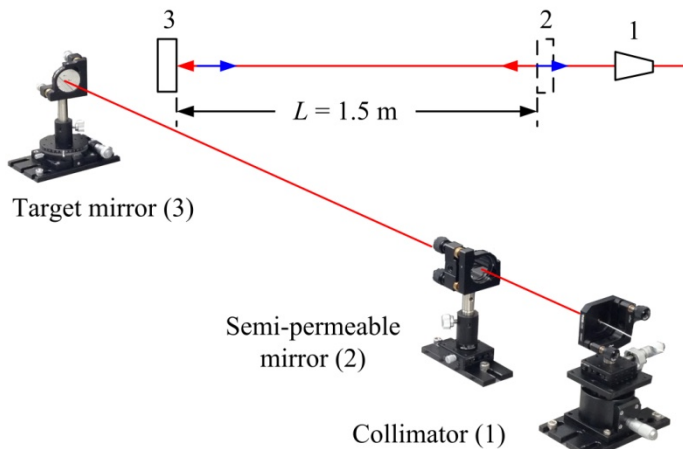
Fig.3.2 Measurement arm of the pulsed interferometer.

Other parts such as a fiber beam splitter, an optical fiber circulator, and a photodetector, are connected together with interferometer passing through FC-connectors that make the measuring system very convenient for applications. However, the optical alignments are very important to the interferometer, because any misalignment, the returned light signal will be weak. Additionally, all optical components must be cleaned because dust, oil or alcohol can damage optical components, especially optical fibers.

3.2.2 Peak positions of envelope interference fringes analysis

The interference fringes of a single-mode fiber optical-comb pulsed interferometer will occur only if the *OPD* of the two arms is satisfied by conditions of **Eq. 2.9**. The first fringe generated by a reference position (semi-permeable mirror, m_0) will be overlapped with the second fringe that is produced by a measuring arm (target mirror, m_1). Both fringes will be combined together, and appeared at the same position on the screen, when observed by an oscilloscope. In practice, a measuring arm is provided a slightly displacements while a

scanning path extends the optical path difference. As a result, both interference fringes will be separated as shown in **Fig. 3.3**. Therefore, the optical path length of the absolute length under observation is longer than ($mc/n_{air}f_{rep}$), so that the absolute length under measurement is determined by **Eq. 3.1**, where ΔL is the distance of peak-to-peak of the envelope interference fringes.

$$L = \frac{mc}{2n_{air}f_{rep}} + \Delta L \tag{3.1}$$

In practices, the distance of peak-to-peak of envelope interference fringes are determined offline after achieving interference fringes signal from a memory device of an oscilloscope. For interference fringes analysis, if the interference fringe is a smooth curve as a Gaussian profile as shown in **Fig. 3.4 (a)**, it is simply to determine the peak position of envelope interference fringe by Gaussian fit curve function. However, the signals contain noise due to air-flow fluctuations and mechanical vibrations. To reduce the error, only a haft of the maximum intensity of each interference fringe is considered. After that, the signals are fitted to obtain envelope fringes by a Gaussian distribution function and determined the distance of peak-to-peak of envelope signals. Normally, the distance of ΔL in **Fig. 3.3** is represented in time scale. So that ΔL has to be converted from time to length scale, which the conversion of time to length scale measurement is discussed in **Section 3.4.1**
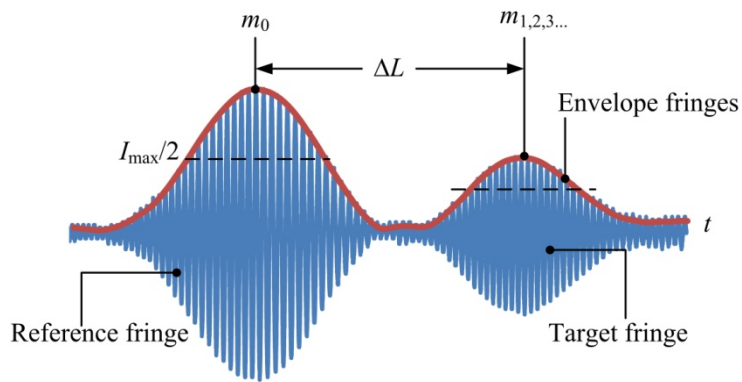
Fig. 3.3 Interference fringes of pulsed interferometer.

The experimental measurements found that the closest of peak positions can be remained close together approximately 20 μm as shown in **Fig. 3.4 (b)**. The interference fringes will overlap with each others, if they are closed less than 20 μm. This situation the peak position cannot be precisely detected because one interference fringe will affect another. On the other hand, if two interference fringes are completely separated with each others as shown in **Fig.**

3.3, the distance of peak-to-peak of envelope interference fringes can be precisely achieved. Graph in **Fig. 3.5** shows standard deviations of peak-to-peak position detections by Gaussian fit curve function corresponding to the distance of peak positions.
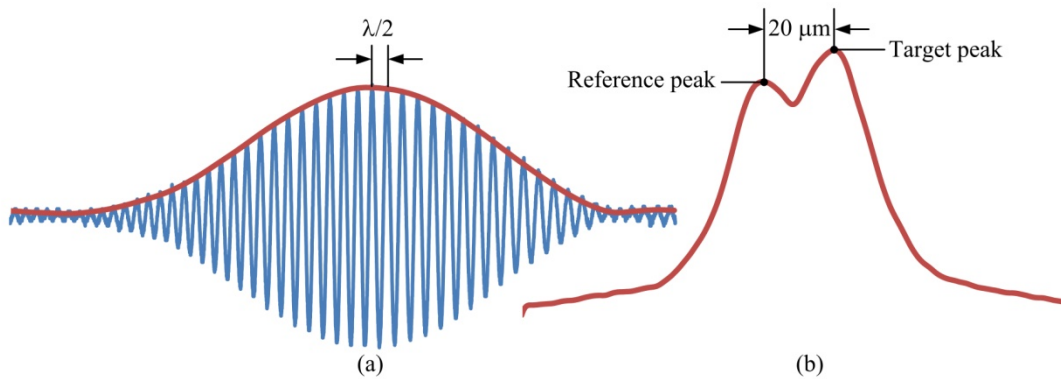
Fig. 3.4 Envelope interference fringe: (a) is a smooth Gaussian profile, (b) is shown the closest envelope peaks.
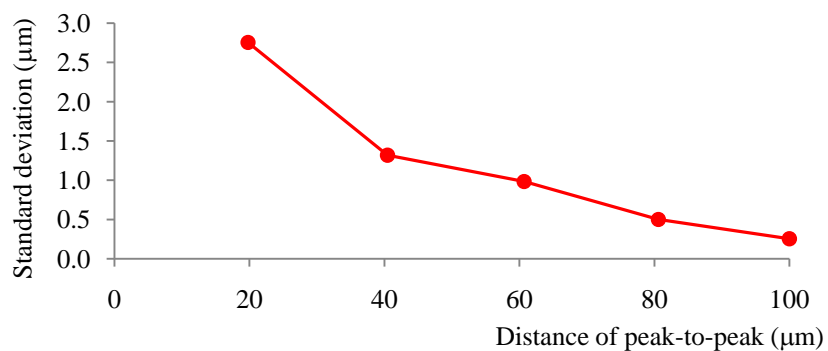
Fig. 3.5 Standard deviations of peak-to-peak positions detected by Gaussian fit curve function corresponding to the peak positions of interference fringes.

The distances of peak-to-peak estimation by Gaussian fit curve function corresponding to the peak positions of two interference fringes show that the distance, ΔL can be precisely achieved when two interference fringes are completely separated with each others. However, based on Gaussian fit curve function, the peaks detection will be lost the accuracy if both sides of interference fringe between the peaks are asymmetry. Asymmetry interference fringes can be caused by affecting of environmental conditions and imperfect of optical alignment. More precise peak detection method is discussed in **Chapter 6**.

3.3 Fabry-Pérot etalon

The controllable repetition frequency is a key for practical absolute-length measurement of a single-mode fiber optical-comb pulsed interferometer as mentioned in **Table 2.3**. In this research, a fiber type of Fabry–Pérot etalon or etalon plays an important role of frequency mode selector for generating the absolute fringe positions of the requiring distance. Fortunately, the original accuracy of the optical frequency comb is not affected by the etalon. Generally, an etalon is a typically made of a transparent plate with two reflecting surfaces, or two parallel highly reflecting mirrors. It is an interferometer which a beam of laser undergoes multiple reflections between two reflecting surfaces. The resulting optical transmission is periodic in wavelength [48–51]. Following sections are going to explain characteristic of etalon in application of a single-mode fiber optical-comb pulsed interferometer.

3.3.1 Properties of Fabry-Pérot etalon

The simplest etalon consists of a plane-parallel solid plate of thickness d and refractive index n which is enclosed in medium of index n' as shows in **Fig. 3.6**.
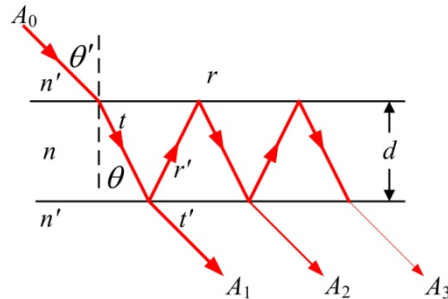
Fig. 3.6 Multiple-reflection model of a Fabry–Pérot etalon.

Let the light wave is incident on the etalon at an angle θ' to the normal, a part of light reflected and transmitted. The transmission gives an angle θ in refractive index of the medium n due to Snell's law. The partially transmitted amplitude from the first ray is given by A_1. Successive reflections inside an etalon, path difference between adjacent rays is:

$$OPD = 2nd \cos\theta \qquad (3.2)$$

The multiple output beams change in phase due to the different path length traversed by each beams. The optical phase obtained by the light on one round-trip through the etalon is:

45

$$\delta = \frac{2\pi}{\lambda} \cdot 2nd \cos \theta \qquad (3.3)$$

Assume that, r and t is the amplitude transmission and reflection coefficient for light waves incident from n toward n' while r' and t' are corresponding quantities for waves traveling from n' toward n respectively. The complex amplitude of the total transmitted wave is the sum of transmitted wave amplitude and is given by:

$$A_t = A_0 \cdot tt' (1 + r'^2 e^{i\delta} + tt' r'^4 e^{i2\delta} + ...) = \frac{tt'}{1 - rr' e^{i\delta}} \cdot A_0 \qquad (3.4)$$

According to Stokes relations, the relative phase of light reflected and transmitted at a boundary of difference refractive indices, so that $r^2 + tt' = 1$, and $r = -r'$. The fraction output intensity or power transmission from the ideal etalon is given by:

$$\frac{I_t}{I_0} = \frac{A_t A_t^*}{A_0 A_0^*} = \frac{(tt')^2}{(1 - rr')^2 + 4\sqrt{rr'} \sin^2(\delta/2)} = \frac{(1-R)^2}{(1-R)^2 + 4R \sin^2(\delta/2)} \qquad (3.5)$$

where $R = r^2 = r'^2$ and $T = tt'$ are the fraction of intensity of the reflected and transmitted at each interface respectively. Therefore, the transmission of the etalon is a maximum when the phase difference for a round-trip is:

$$\delta = \frac{2\pi}{\lambda} \cdot 2nd \cos \theta = 2m\pi \qquad (3.6)$$

So that the fractional output intensity or power transmission in **Eq. (3.5)**, and from the ideal etalon is given by:

$$\frac{1}{1 + F \sin^2(\delta/2)} \quad , \text{ where } \quad F = \frac{4R}{(1-R)^2} \qquad (3.7)$$

This function is known as the Airy function, and F is called finesses coefficient. **Fig. 3.7** presents the Airy distribution as a function of δ with difference reflection coefficients R (the MATLAB simulation code can be found in **Appendix, Fig. A2**). Expressing the maximum condition in terms of frequency, the location of transmission peak locations are:

$$f = m \frac{c}{2nl \cos \theta} \qquad (3.8)$$

Therefore, the frequency separation between successive peaks can be determined. The peak-to-peak separation in frequency is called the free spectral range (FSR) and is given by:

$$\text{FSR} = \Delta f = f_{m+1} - f_m = \frac{c}{2nd\cos\theta} \qquad (3.9)$$

If θ in **Eq. (3.9)** is very small, the frequency spacing between maximum transition peaks in an etalon depends on the refractive index of the medium n and thickness d. When peaks are very narrow (high finesse), this property permits the etalon to act as very narrow band-pass filter. The characteristic of an etalon as a function of frequency is presented in **Fig.3.8**.
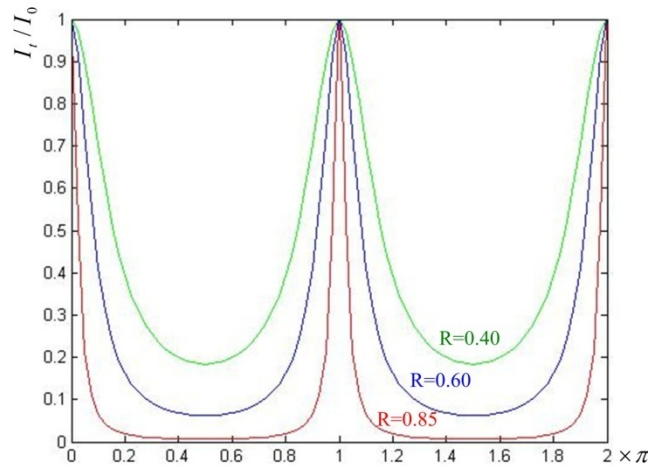
Fig. 3.7 Simulation of Airy functions for difference reflection coefficients of the idea etalon.
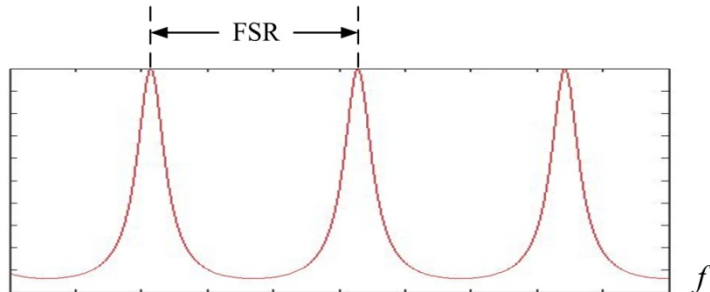
Fig. 3.8 Free spectral range of an etalon.

In addition, Fabry–Pérot etalon can also be produced from a pair of plane-parallel mirrors, concave mirrors, or optical fiber with coating [50, 52]. Examples of etalons and their central frequency shown in **Fig.3.9** and **Fig. 3.10** are the plane-parallel mirror etalon, and the fiber etalon. The etalon types depend on their applications. An etalon that is build from mirror type, the cavity length can be adjusted for selecting the required FSR. However, it is unstable because it is easily disturbed by air temperature and mechanical vibration. Alternatively, fiber

etalon is very useful because it is a slightly disturbed by surrounding environment, but the cavity length is fixed. However, the accuracy of the original repetition frequency of an optical frequency comb is not affected by etalon, because the performance of the etalon is only filtering of the comb.
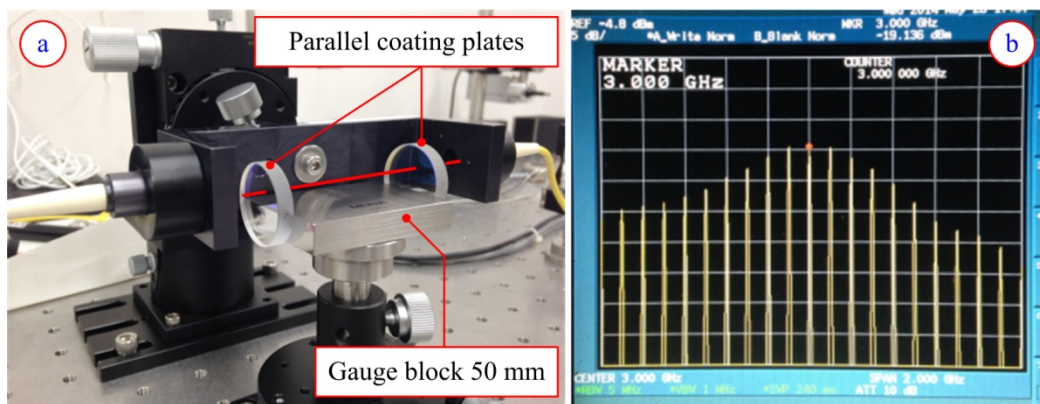
Fig. 3.9 Plane-parallel etalon: (a) is the simplest build by a gauge block and a pair of optical-parallel coating plates, cavity length can be adjusted by changing the size of gauge block or using mirror holder, (b) is the central frequency of 3−GHz FSR.
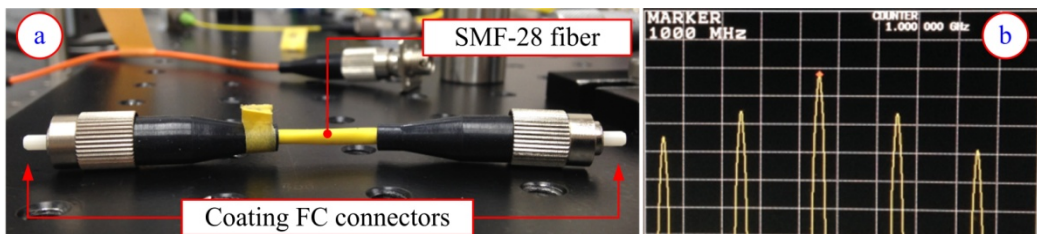
Fig. 3.10 Fiber type etalon: (a) is a single-mode optical fiber, which the FC-connectors coated by 85% reflecting able film, (b) is the central frequency of 1−GHz FSR.

3.3.2 Cavity length of an etalon measurement

The FSR of an etalon is proportional to refractive index of the fiber medium and the length of the fiber cavity. To compose a prefect fiber etalon is not easy because of inhomogeneous-medium index of a fiber and the coating etalon. It is difficult to control the cavity length of a fiber etalon. This experiment demonstrates the simplest way to measure the cavity length of a fiber etalon.

To measure the cavity length of a fiber etalon, an unbalanced-arms Michelson interferometer is applied. The measurement setup diagram is shown in **Fig. 3.11 (a)**. A fiber etalon was connected to a low-coherence light source (Multiband ASLD-CWDM-3-B-FA, Amonics, wavelength range of 1456 nm-1650 nm). The light beam was divided by a fiber beam splitter (50:50), a reference mirror (M1) was fixed, and a measuring mirror was installed on a precise translation stage (50 nm resolution of FS-3150X, FC-401 controller, Sigmatech), and the interference fringe signal was detected by an InGaAs photoreceiver (2053FC-M, Newport).
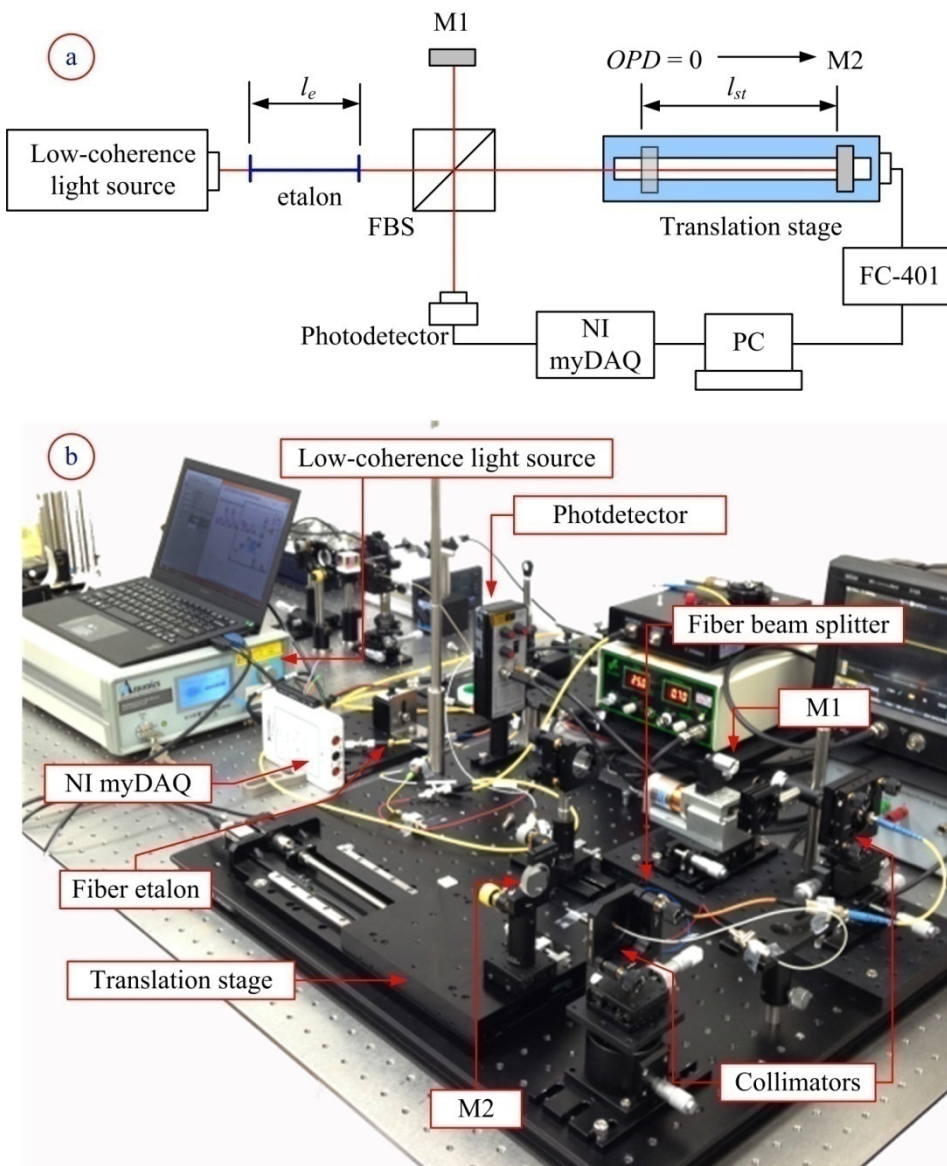
Fig. 3.11 the cavity length of a fiber etalon measurement: (a) is measurement setup diagram, and (b) is a photograph of the measurement.

Based on a low-coherence interferometer, the interference fringe will be generated if the *OPD* of M2 to M1 equals to zero, and the length of etalon cavity. Thus, the cavity length of a fiber etalon can be directly determined by the relationship between the peak-to-peak of the interference fringe and the length of a translation stage as:

$$l_e = \frac{l_{st}}{n_f} \qquad (3.10)$$

where l_e is the cavity length of a fiber etalon, l_{st} is the indication length of a translation stage, and n_f is the refractive index of a fiber etalon ($n_f = 1.4682$).

To achieve high accuracy of the measurement, an automatic data recording system is required. The interference fringes were recorded to a personal computer passing through the connection of a photodetector and a data acquisition device (NI DAQ). As the same time, the travel-length positions of a translation stage were acquired by a stage controller (FC-401, Sigmatech) to a personal computer through a Universal Serial Bus (USB) device. In the experimental measurement, a translation stage was operated by a constant speed of 2 mm/s, and NI DAQ was set at the maximum sampling rate of 200kS/s. The pattern fringes of a low-coherence interferometer are shown in **Fig. 3.12**.
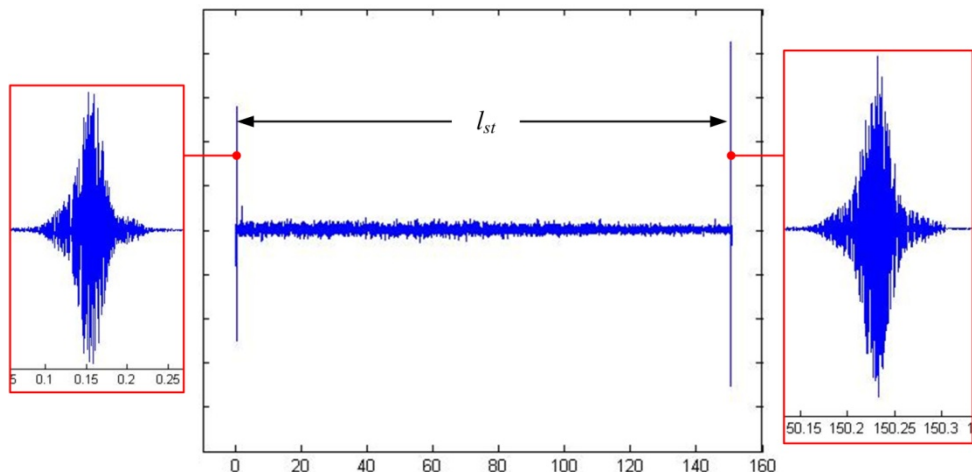
Fig. 3.12 The position length of a translation stage when pattern fringes are generated.

The average length of l_{st} is 150.31689 mm for 10 time measurement repetitions, which the maximum measurement standard deviation is approximately 18 μm. Therefore, the cavity length of a fiber etalon calculated by **Eq. 3.10** became 102.338175 mm. By this technique, the cavity length of a fiber etalon can be measured in order of sub-micrometer. However, for a high precision of the measurement, this measuring system is required a high-speed data

acquisition and real-time detecting of both the position of translation stage and the interference fringe signals. Although a poor length of the etalon cavity, the single-mode fiber optical-comb pulsed interferometer can be compensated. The important properties of an etalon are that a high finesse which indicates a sharper transmission peaks with lower minimum transmission coefficients, while accurate etalon cavity provides precise absolute position of interference fringe.

3.3.3 The absolute length of 1-GHz FSR fiber etalon
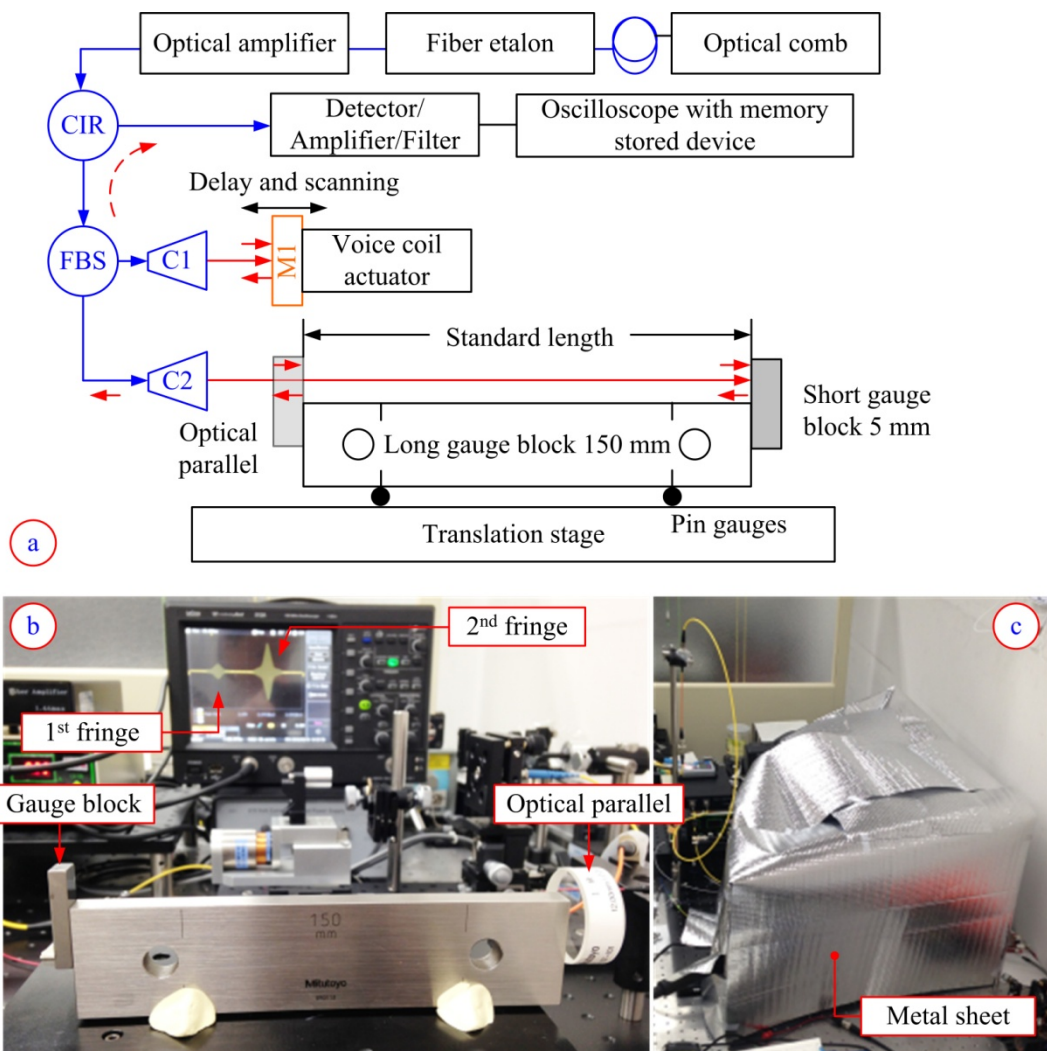
Fig. 3.13 The absolute-length measurement by a single-mode fiber optical-comb pulsed interferometer based on using 1−GHz FSR fiber etalon comparing with a standard long gauge block: (a) is measurement setup diagram, (b) is a photograph of the experimental measurement, (c) is the measurement setup covered by the metal sheet.

The generated positions of interference fringes are very importance for determining the absolute length under measurement, which relate to the FSR of a fiber etalon. If the FSR of an etalon is not completely meet as the required length, it must be measured and compensated. This experiment demonstrates how to confirm the accuracy of a single-mode fiber optical-comb pulsed interferometer based on using a fiber etalon. The absolute length is directly compared with a standard length of a long gauge block. The measurement setup is shown in **Fig.3.13**. The standard long gauge block, LGB [Mitutoyo, 150 mm, grade−0, thermal expansion coefficient of $(10.8 \pm 0.5) \times 10^{-6}$ K^{-1}] was used as the standard length. The first fact of the LGB was wrung by an optical parallel, and other fact was wrung by a short gauge block (GB). The Airy points of the LGB were supported by two pin gauges on a translation stage. The laser beam after passing through a fiber etalon was amplified, because the laser power was reduced by a fiber etalon. The laser beam that connected to a collimator C2 was aligned until perpendicular to an optical-parallel plate over the travel range of a translation stage. This condition can be obtained by a power meter, which is connected to the output port (P3) of the CIR. The maximum output power is obtained when laser beam is perpendicular to an optical parallel plate. After that, a translation stage was moved until the first interference fringe appeared due to the reflected beam from the inner surface of an optical-parallel plate. Suddenly, the second fringe will be automatically generated because the stroke of a voice coil actuator provides enough range for the extended *OPD* condition.

Table 3.1 The measurement results between the proposed method and a standard LGB

t (°C)	ΔLGB_t (mm)	LGB_t (mm)	ΔL (μm)	Measured value (mm)	Difference (μm)
21.80	0.00292	150.00292	486.62	150.00294	-0.02
21.80	0.00292	150.00292	486.52	150.00304	-0.12
21.81	0.00293	150.00293	486.52	150.00304	-0.10
21.81	0.00293	150.00293	487.04	150.00292	0.01
21.81	0.00293	150.00293	486.52	150.00304	-0.10
21.81	0.00293	150.00293	486.94	150.00292	0.01
21.82	0.00295	150.00295	486.71	150.00285	0.10
21.83	0.00296	150.00296	486.44	150.00312	-0.15
21.83	0.00296	150.00296	485.95	150.00311	-0.14
21.83	0.00296	150.00296	486.93	150.00311	-0.15
Average	0.00294	150.00294	486.93	150.00301	-0.07
SD	0.00002	0.00002	0.31	0.00009	0.09
Variation	0.00005	0.00005	1.09	0.00027	-0.25

Note: SD is the measurement standard deviation, and difference is the measured value − LGB_t.

In this experiment, the thermal-expansion compensation for the LGB is required. The length of the standard gauge block relates to the gauging temperature and the thermal expansion coefficient, which depends on material of gauge block. For that reason, a temperature sensor was attached on the LGB, and the measurement comparison was covered by the metal sheet more than 24 hours for keeping stabilized gauging temperature of the LGB before taking the measurement as shown in **Fig. 3.13 (c)**. The results of 10 measurement repetitions are shown in **Table 3.1**. The experimental measurements were done under the conditions of 23.02 °C, 23.34 %RH, and 101.28 kPa for air temperature, air humidity, and air pressure, respectively. Where t is the gauging temperature of the LGB, ΔLGB_t is the expanded length of LGB due to difference in length from the reference temperature (20 °C).

The measurement results in **Table 3.1** indicate that the single-mode fiber optical-comb pulsed interferometer, which the absolute lengths are determined based on using the 1−GHz FSR fiber etalon, is different from the standard length of a long gauge block of approximately −0.07 μm with measurement standard deviation is approximately 0.09 μm.

Additionally, for a high accuracy measurement in nanometer scale with an interferometer, the effect of the phase change of reflected light from the surface between two media should be considered. General phase change is presented because of a surface roughness. However, although the surface is flat, the phase changes on reflection still occur due to the complex refractive index ($n_1 - ik_1$), which depends on laser wavelength and optical properties of material. The difference of phase change gives measurement errors of several tens of nanometers. The reflection of the light penetrates from the geometrical surface to the inside of the substrate by $\lambda\rho/4\pi$, where λ is the wavelength of light source and ρ is the phase change that is given by **Eq. 3.11** [53].

$$\rho = \tan^{-1}\left[\frac{2n_0 k_1}{(n_1^2 + k_1^2 - n_0^2)}\right] \tag{3.11}$$

From above experimental measurement, n_1 is the refractive index of a steel gauge block and k_1 is the extinction coefficient, and it is approximately $2.67 - 4.03i$ for steel material [54]. The refractive index of air layer is defined as n_0 and assumed to be 1. Thus, the phase change is calculated to be 19° that is equivalent to a shift length of ~43 nm. However, this calculation is based on a wavelength of 1.56 μm. In this experiment, the first face of the LGB is wrung by an optical parallel plate, which the refractive index is greater than air. Therefore, the phase of the reflected light from the inner surface of the optical parallel plate is not changed. Then, only the

penetration depth on gauge block surface should be considered. Additionally, the error due to wringing of gauge blocks should also be considered for the compensation. The wringing error depends on flatness and roughness of gauge block surface, which affect to the change of phase. This correction can be measured and determined by several methods [55–57]. However, the shifting in length due to phase change is in order of ~10 nm to ~50 nm, depends on optical properties of material, surface roughness and wavelength of light source. This error can be ignored when compared with the accuracy ratio of the maximum permissible error of a general CMM. Conversely, it has to be concerned when apply for the nanometer scale measurements.

3.4 Absolute length based on 1-GHz FSR fiber etalon

As mentioned in **Section 3.3**, the step length or absolute distance of the absolute-length measurement can be performed approximately of every 150 mm by the 1−GHz FSR fiber etalon. Following topics below are going to discuss and demonstrate the time scale to the length scale measurement of peak-to-peak distance of envelope interference fringes, stability of a single-mode fiber optical-comb pulsed interferometer, which 1−GHz FSR fiber etalon plays a role of determining the absolute position, and the accuracy of a single-mode fiber optical-comb pulsed interferometer comparing with a commercial cw-laser interferometer.
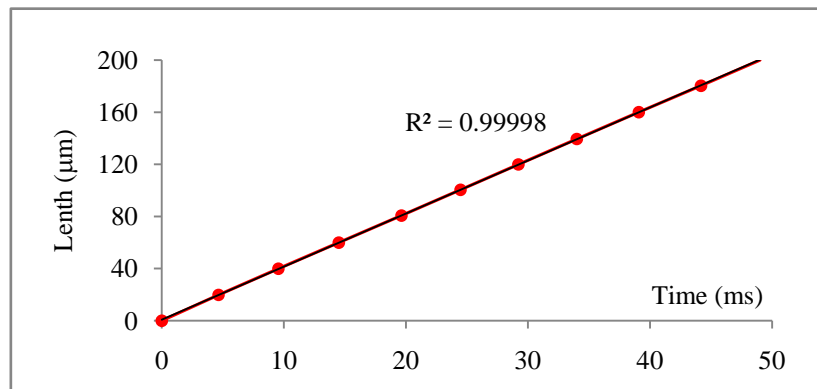
3.4.1 Time scale to length scale measurement
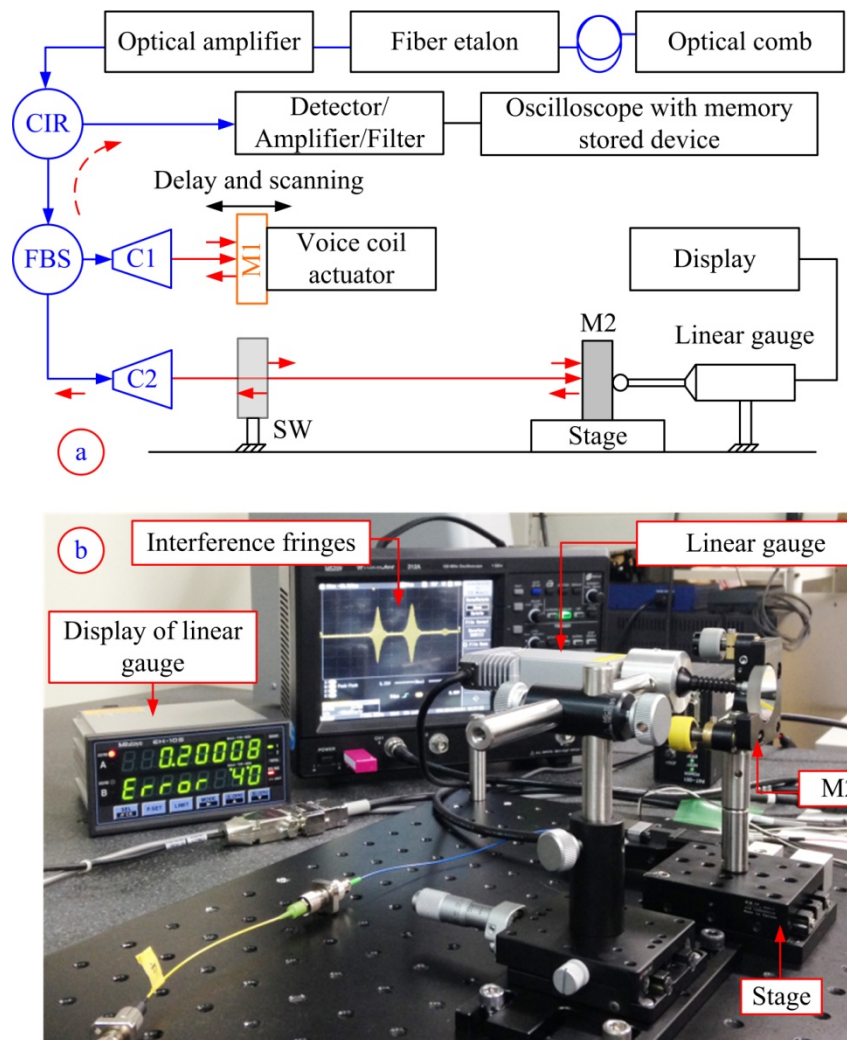
Fig.3.14 Time scale to length scale measurement: (a) is measurement setup diagram, and (b) is photograph of the experimental measurement.

The peak envelope interference fringes of a single-mode fiber optical-comb pulsed interferometer are involved with the time domain as mentioned in **Section 3.2.2**. In application, the time scale must be converted to the length scale for determining distance of peak-to-peak of envelope interference fringes [58]. The measurement setup diagram to determine this relation is shown in **Fig. 3.14**.

The linear gauge (Laser Hologauge LGH-110, Mitutoyo) with a resolution of 10 nm was installed behind a target mirror (M2). Normally, two interference fringes will occur on the screen of an oscilloscope when the distance between the target mirror (M2) and the reference position (SW) is approximately 150 mm or the *OPD* is approximately 300 mm. This measurement was performed, when the target mirror was moved by a translation stage controller (FC-401, Sigma Tech) in positive direction. The result is that the changing positions of the mirror target were measured by a linear gauge. As the same sequence, the changing positions in time scale of peak envelope interference fringes on the screen of an oscilloscope were recorded. In this experiment, a voice coil actuator was operated by a constant speed of 0.001 m/s. The measurement results are shown in **Fig. 3.15**.

Fig. 3.15 Measurement result of the relation between time and length scale.

Fig. 3.15 is a least-squares fitting of the data set between the length scale (*y*-axis) and the time scale (*x*-axis). The maximum deviation between the dependent variable (length scale) and the best-fit line is approximately 0.31 μm with the standard deviation is approximately 0.23 μm, and the correlation coefficient (R^2) is approximately 0.99998. Results indicate that two data sets match a straight line and linearity. Although a voice coil actuator oscillates both positive and negative directions, the hysteresis of the scanning device is not affected because only one side of the scanning is required and selected for determining this relation. However, the conversion factor depends on the speed of the scanning device. Thus, a constant speed of the scanning fringe is necessary.

3.4.2 Stability of a single-mode fiber optical-comb pulsed interferometer

The stability of the measuring system is a factor that indicates the efficiency of a measuring instrument for a long-time of the operation. To perform measurement stability of a single-mode fiber optical-comb pulsed interferometer, the measurement was setup as shown in **Fig. 3.16**.
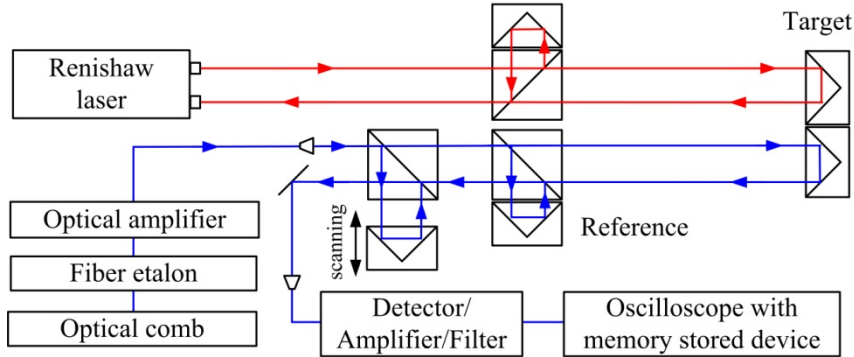
Fig. 3.16 Stability measurement setup diagram of a single-mode fiber optical-comb pulsed interferometer comparing with a commercial cw-laser interferometer.

A single-mode fiber optical-comb pulsed interferometer was set pair with a commercial cw-laser interferometer (Ranishaw length-measuring 633 nm, He-Ne laser interferometer). Both interferometers were prepared in an air-uncontrolled laboratory. Lengths approximately of 150 mm were measured every ten minutes in one hour. The environmental conditions (ambient air temperature, relative humidity and air pressure) were also recorded. Then, the drifts in length of both interferometers were calculated.
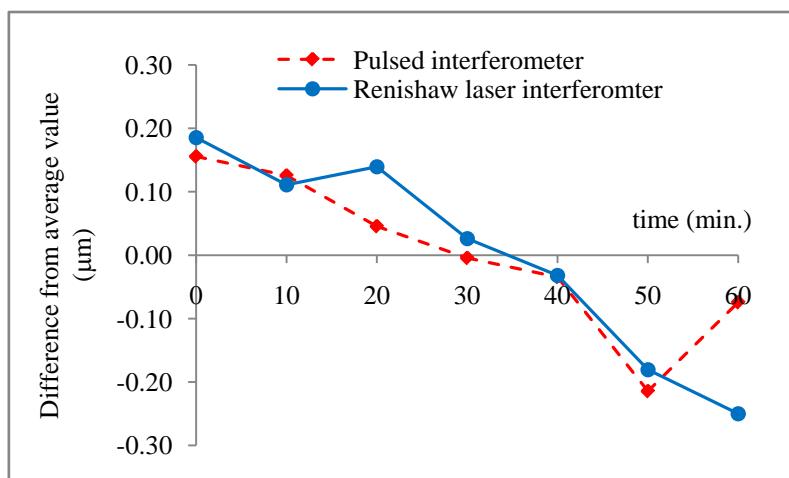
Fig. 3.17 Measurement results of the stability between a single-mode fiber optical-comb pulsed interferometer and a commercial cw-laser interferometer.

The average value of the ambient air temperature, relative humidity, and air pressure are 25.60 ℃, 36.5 %, and 101.02 kPa; and the maximum variations are approximately 0.2 ℃, 1.7 % and 10 Pa, respectively. The measurement results are illustrated in **Fig. 3.17**, and results show that the variations from the average values of both measuring systems have the same drift tendency. The maximum variations of pulse interferometer and incremental interferometer are 0.25 μm and 0.21 μm. The maximum difference between the two curves is approximately 0.1 μm. This experimental experiment can be summarized that the measurement stability of a single-mode fiber optical-comb pulsed interferometer is satisfied for applications comparing with a commercial cw-laser interferometer.

3.4.3 Measurement accuracy comparison

The accuracy of a single-mode fiber optical-comb pulsed interferometer was compared with a commercial cw-laser interferometer again. **Fig. 3.18** shows the measurement comparison.
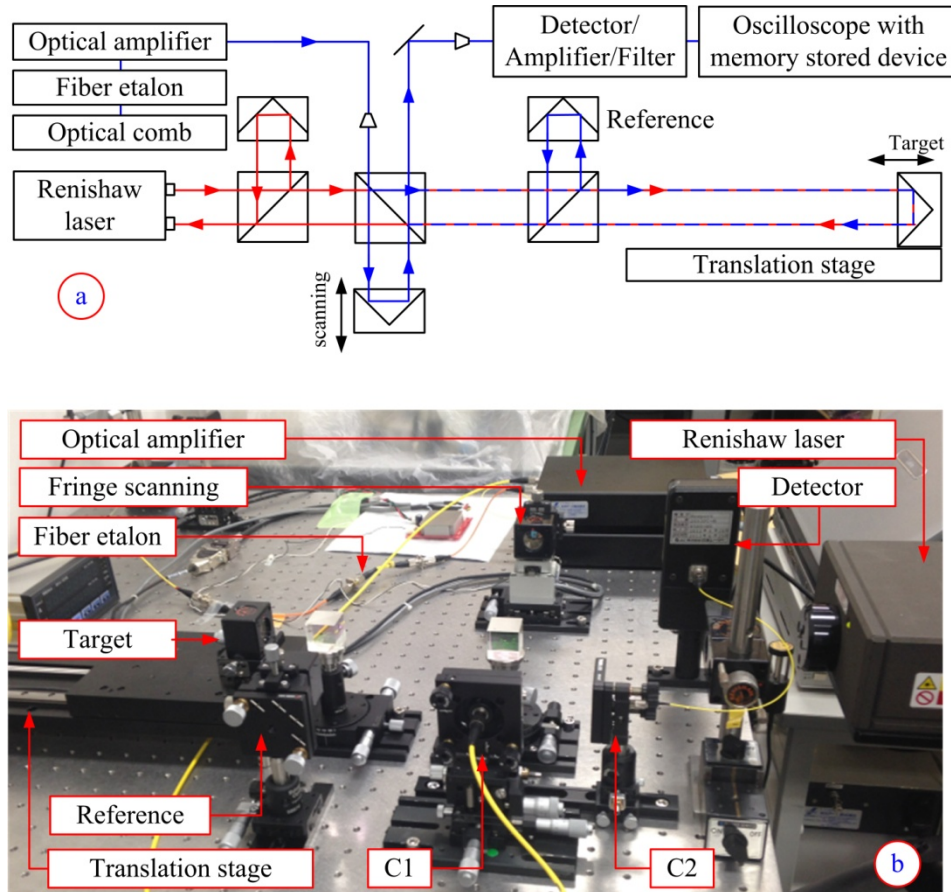
Fig. 3.18 Accuracy of the single-mode fiber optical-comb pulsed interferometer comparison: (a) is comparison setup diagram, and (b) is photograph of the measurement comparison.

Because of the interference fringe counting method of a cw-laser interferometer, the measurement accuracy comparison requires a long-precise translation stage. Both interferometers share the same target for avoiding the motion errors of a translation stage. The precise positions of a translation stage were controlled by a stage controller with a resolution of 0.05 μm. The target which was installed on a translation stage was moved by the stage controller from the reference position to the distance of approximately 150 mm. Subsequently, the lengths were measured five times by both interferometers. The environmental conditions were recorded for compensation of the refractive index of air for both interferometers. The measurement results are listed in **Table 3.2**.

Table 3.2 Accuracy comparison results.

Average of environmental conditions		
Air temperature (°C)	Air humidity (%RH)	Air pressure (kPa)
25.60	36.5	101.02
No.	Pulsed interferometer (mm)	cw-interferometer (mm)	Difference (μm)
1	149.85692	149.85689	0.03
2	149.85693	149.85694	-0.01
3	149.85692	149.85682	0.09
4	149.85692	149.85689	0.03
5	149.85693	149.85710	-0.18
SD	0.01	0.10	μm

Note: SD is the measurement standard deviation of five time repetitions.

The measurement results indicate that the maximum difference of length measurement by both interferometers is approximately −0.18 μm. The measurement repeatability of a single-mode fiber optical-comb pulsed interferometer is a tiny larger than a commercial cw-laser interferometer. The measurement repeatability can be affected by many factors such as the peak detection method, affecting of environmental conditions, imprecise of a scanning device, and imperfect of optical alignment. However, the accuracy of the single-mode fiber optical-comb pulsed interferometer is acceptable comparing with a commercial laser interferometer. The accuracy and repeatability improvements are discussed more details in **Chapter 6**.

3.5 Chapter conclusion

This chapter mainly discusses about the single-mode fiber optical-comb pulsed interferometer in which the 1−GHz FSR fiber etalon is used as a frequency mode selector for generating required absolute length. In practice, a high finesse of an etalon indicates a sharper transmission peaks with lower minimum transmission coefficients, while accurate etalon cavity provides precise absolute position of interference fringe. However, to compose a perfect fiber etalon is not easy because the cavity of a fiber etalon depends on both fiber length and homogenous medium index of fiber material. So, the absolute position of interference fringe using any fiber etalon must be confirmed before applications. It is simply to confirm absolute position by comparing with known length such as the standard length of a long gauge block. The average difference in length from the 150 mm of a standard long gauge block is approximately −0.07 μm with the maximum standard deviation approximately 0.09 μm. The measurement repeatability of a single-mode fiber optical-comb pulsed interferometer mainly involves with the evaluated distance of peak-to-peak of envelope interference fringes.

The distance of peak-to-peak estimation by Gaussian fit curve function corresponding to the position of two interference fringes shows that the distance, ΔL can be precisely achieved when two interference fringes are completely separated with each others. The closest position of two peaks can be remained close together approximately 20 μm, before they are overlap. However, the peaks detection will be lost the accuracy if both sides of fringes between the peaks are asymmetry. Asymmetry interference fringes can be caused by affecting of environmental conditions, imperfect optical alignment, and poor accuracy of a scanning device. The conversion of the time scale to the length scale of interference fringes is measured by a linear gauge with resolution of 10 nm. The maximum deviation from the best-fit line is approximately 0.31 μm, and the standard deviation is approximately 0.23 μm. These results can be caused by peak detection method, affecting of environmental conditions, imprecise of a scanning device, and imperfect of optical alignment. The accuracy and repeatability improvements are discussed more details in **Chapter 6**. The measurement accuracy and the stability of the proposed measuring system are confirmed by comparing with a commercial cw-laser interferometer. The results show that the variations from the average values of both measuring systems have the same drift tendency. The maximum variations of pulse interferometer and commercial interferometer are 0.25 μm and 0.21 μm in 1 hour. The maximum difference of length measurement form both systems is approximately −0.18 μm. The measurement accuracy and stability of a single-mode fiber optical-com pulsed interferometer is satisfied for CMM applications comparing the maximum permissible error of industrial CMM. The applications are discussed in the next chapter.

Chapter 4 Positioning accuracy of a CMM verification using a metal ball target

4.1 Introduction

This chapter discusses an application of the single-mode fiber optical-comb pulsed interferometer for the measurement of the CMM positioning accuracy. Normally, a single-mode fiber optical-comb pulsed interferometer with a flat mirror or a cube mirror target, the measuring system can be applied to measure absolute length only one direction because the target has to reflect the laser beam back to interferometer as the same path in opposite direction of the incident beam. These targets make time consumption in alignment process for CMM verification. As mentioned before, this research requires using only a target that can be applied to measure the absolute length in any directions of the measurement setup, and plans to use more than one measuring system with a target in the future. Thus, a spherical target type is considered as the target of interferometer.

To begin with the rough metal balls, because they are able to act as three-dimensional targets of a single-mode fiber optical-comb pulsed interferometer. In addition, the laser beam alignment on a rough sphere surface target is easily. It has a large surface area for reflecting the laser beam back to interferometer than a smooth surface ball. Therefore, this chapter starts with studying the effect of the surfaces roughness of the targets to the absolute-length measurements. The standard roughness scale plate with difference of Ra vales is used to obtained interference fringes. Experiments demonstrate interference fringes which are produced by difference of roughness surface of the target and show how they affect to absolute-length measurement. Subsequently, an experiment demonstrates that what will happen if the laser beam is not located at the center of the metal ball target. Then, the preliminary absolute-length measurement up to 1.5 m is demonstrated and discussed. Finally, the positioning accuracy of a moving-bridge type CMM is verified by the proposed measuring system comparing with a commercial continuous-wave laser interferometer. Additionally, the uncertainty of measurement based on proposed measuring system is explained and discussed at the end of this chapter.

4.2 Absolute-length measurement with a rough metal ball target

In applications, a target that can be used to measure the absolute length in any directions of the measurement setup is required. Thus, the rough metal ball is considered as the target of a single-mode fiber optical-comb pulsed interferometer because a sphere ball provides three-dimensional target for the interferometer. Moreover, a rough metal ball easily makes the laser beam alignment. However, the repeatability and accuracy of the measurement are affected by the target surface. The experimental measurements below demonstrate the efficiency of absolute-length measurement to the target surfaces.

4.2.1 Effect of the surface roughness targets to the absolute-length measurement
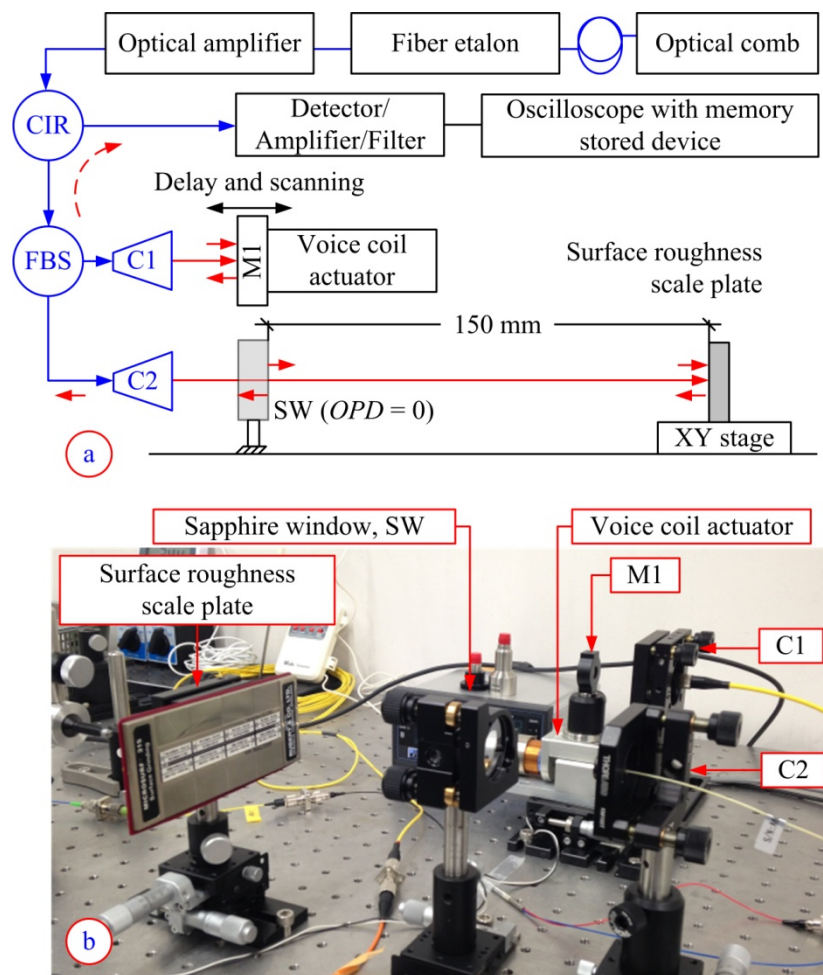
Fig. 4.1 Measurement setup to determine the effect of the target surfaces to interference fringes: (a) is measurement setup diagram, and (b) is photograph of the measurement.

The measurement setup is illustrated in **Fig. 4.1**. The surface roughness scale standard plate with Ra of 0.025 μm, 0.05 μm, 0.1μm, and 0.2 μm was used as the target. It was set at the position of approximately 150 mm far from the reference position (SW). After that, the interference fringes were recorded and analyzed. The results are shown in **Fig. 4.2**.
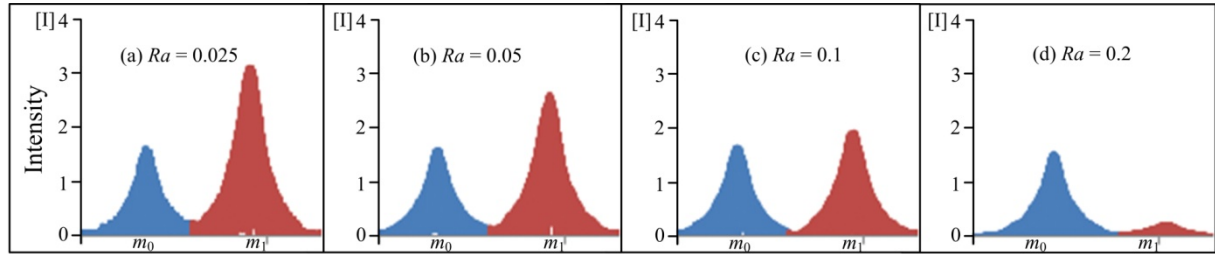
Fig. 4.2 The interference fringes are generated by the different Ra surface: the red graphs are the interference fringes which are generated by the different Ra surfaces; others are generated by a sapphire window plate at the reference position.

The interference fringes which are generated by a surface roughness scale standard plate indicate that the intensity of the interference fringes are significantly weak if the value of Ra is increased. These experimental results strongly show that the power intensity of the reflected beam will be weak if a rough surface of the target ($Ra >> 0.2$ μm) is used. On the other hand, if a smooth surface of the target ($Ra << 0.1$) is used, the power intensity of the reflected beam will be enhanced.

Subsequently, the same plate was moved to a distance of approximately 1500 mm. Then, the absolute length was measured 10 times and was evaluated by **Eq. (3.1)**. The measurement standard deviations were determined corresponding to different Ra surfaces of the target as shown in **Table 4.1**.

Table 4.1 The standard deviations of absolute-length measurement to target surfaces.

Nominal length (mm)	Surface roughness, Ra (μm)	Standard deviation (μm)
	0.025	0.59
	0.05	0.64
1500	0.1	0.74
	0.2	–

The standard deviations of the absolute-length measurements are gradually enlarged if the roughness of the target surface is increased. When the surface roughness of the target is greater

than 0.2 µm, it cannot be used as the target because the reflecting beam from that target cannot reflect back to interferometer. These experimental results show that the surface roughness of the target significantly affects to intensity of interference fringes and basic performances of pulsed interferometer.

4.2.2 Metal ball targets and their interference fringes

Unlike a flat target, a very smooth surface of the sphere target difficultly align the laser beam, because only a small surface area of the center of the concave sphere is the best area for reflecting the laser beam back to interferometer. In contrast, the laser beam alignment is easier when using a slightly rough surface of a sphere target. This experiment demonstrates of two interference fringes, which generated by two rough metal ball targets. They have the same diameter of approximately 25 mm as shown in **Fig. 4.3**
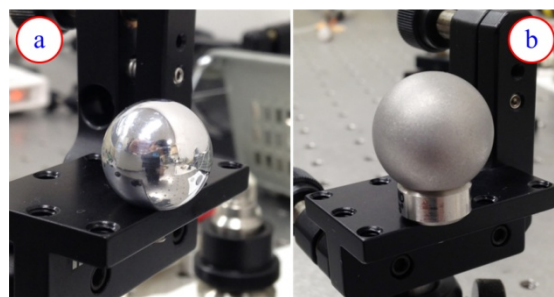
Fig. 4.3 Metal balls targets; (a) is a rough metal ball with *Ra* ~0.1 µm, and (b) is a smooth metal ball with *Ra* ~0.2 µm.

(a) SD = 0.32 µm   (b) SD = 0.55 µm
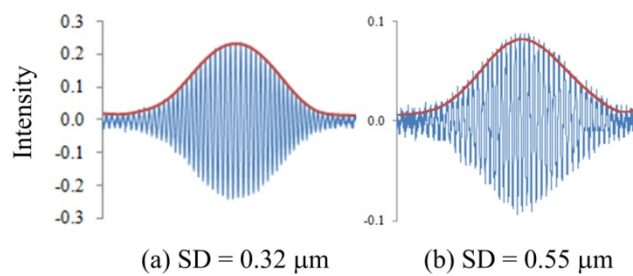
Fig. 4.4 Interference fringes are generated by two metal ball targets; (a) is a smooth surface, *Ra* ~0.1 µm, and (b) is a rough surface, *Ra* ~0.2 µm. SD is the standard deviation of five times measurement repetitions at the reference position ($m = 0$).

Both rough metal ball targets were used to obtain the interference fringes at the reference position ($m = 0$). The experimental setup is the same as described in the previous section, only the target is replaced by metal balls. The first target is a smooth ball that Ra is approximately 0.1 μm; other is a rough ball that Ra is approximately 0.2 μm. The generated interference fringes by both targets were obtained and recorded for analysis. The results are shown in **Fig. 4.4**. The pattern fringes clearly indicate that the roughness surface of the target affects the shape quality and intensity of the pattern fringe. A smooth surface ball presents a perfect shape of interference fringe; intensity is higher than that of a rough metal ball. In addition, a smooth surface ball provides measurement repeatability better than a rough ball target. The maximum standard deviation is approximately 0.32 μm, while a rough ball target is approximately 0.55 μm. Moreover, if the Ra value of the target is higher than 0.2 μm, the interference fringe will disappear, because the laser beams randomly reflect. It cannot be reflected back to interferometer. On the other hand, the intensity of the interference fringe is enhanced if the Ra value is smaller than 0.1 μm. However, the laser beam alignment is not simply if the roughness surface of the metal ball is very smooth ($Ra \ll 0.1$ μm), because the reflected-beam area on the metal ball is too small. This situation also depends on the beam diameter, which a small beam diameter enhance intensity of interference fringe than a large beam.

4.2.3 The accuracy requirement of the laser beam alignment on the target

The small area at the center of a concave sphere is only the best area to reflect the laser beam back to the interferometer. So, this experiment demonstrates that what will happen if the laser beam is not located at the center of a metal ball target. In this experiment, the measurement setup is similar to **Fig. 4.1**, but a smooth metal ball (Ra ~0.1 μm) was used as the target and installed on XY–stage 150 mm far from the reference position by approximately. The photograph of experimental setup is shown in **Fig. 4.5**.
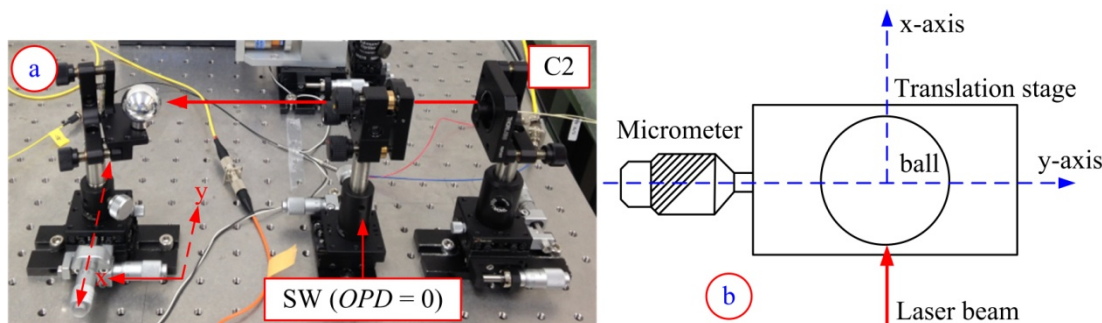
Fig. 4.5 Experimental setup for determining the accuracy requirement of the laser beam alignment on the target: (a) is photograph of the measurement setup, and (b) is a top view setup diagram.

This experiment was assumed that the laser beam was incident on the target in the direction of *x*-axis, and the beam was set at the center of a metal ball, which was confirmed by obtaining the maximum power of the reflected beam from the output port of the CIR. Subsequently, the absolute lengths were measured. Then, the target was moved in the direction of *y*-axis; each step of 20 μm by a micrometer in the range of ± 0.2 mm. The difference in lengths from the center of each step were measured and compared with the theoretical values. The measurement results are shown in **Fig. 4.6**.
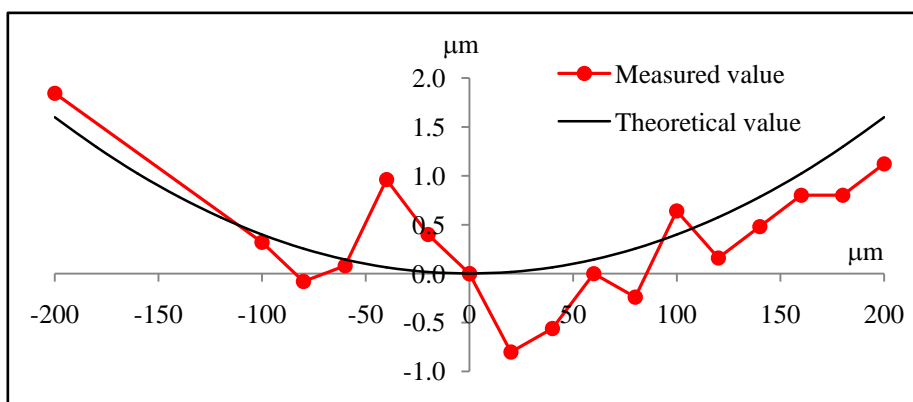
Fig. 4.6 Difference in length from the center of a metal ball between the measured values and the theoretical values.

Graph above shows that the location of the laser beam on the target is significant to the accuracy of length measurement. The trend of measured values seems to be within theoretical value, but some surface area of a metal ball is not smooth enough with its concavity. This is an error factor of the length measurement when the laser beam is misaligned from the center of a metal ball target. However, this experimental result can be implied that if a rough metal ball with *Ra*~0.1 μm and a diameter of 25 mm is used as the target, the beam misalignment of ± 0.2 mm from the center of the target will cause an error of length measurement approximately 1 μm, and cosine error is approximately 1.3 μm.

4.2.4 Preliminary absolute-length measurement

The measurement repeatability of the absolute-length measurement in which a rough metal ball is used as the target has been considered by the preliminary measurements up to 1.5 m. The roughness surface of the target was confirmed and measured based on the international standard of ISO-4287 [59] by Tokyo Seimitsu Company. The surface roughness of a rough metal ball was measured in four sections and a sample profile is illustrated in **Fig.4.7**.
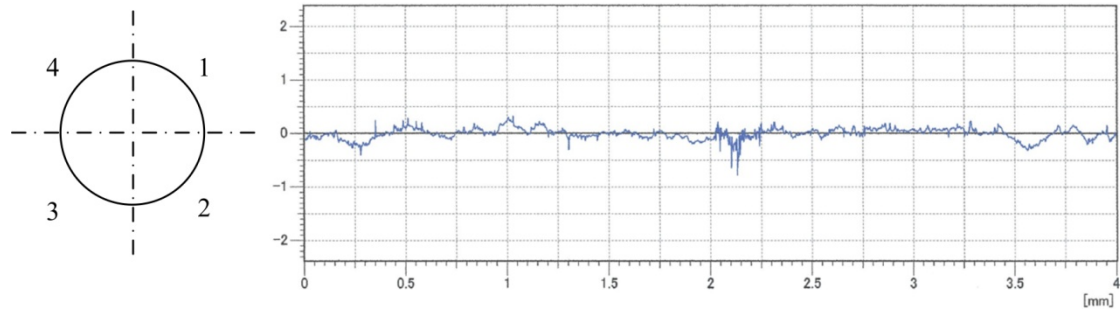
Fig. 4.7 Sample surface profile of a metal ball target in section 1 and the surface roughness; *Ra* are (0.078, 0.109, 0.099, and 0.076) μm for the section of 1, 2, 3, and 4, respectively.

The preliminary measurement setup diagram is shown in **Fig. 4.8**. Subsequently, the target positions were placed every approximately 150 mm to 1.5 m, and then each length was measured 10 times for determining the repeatability of the measurement.
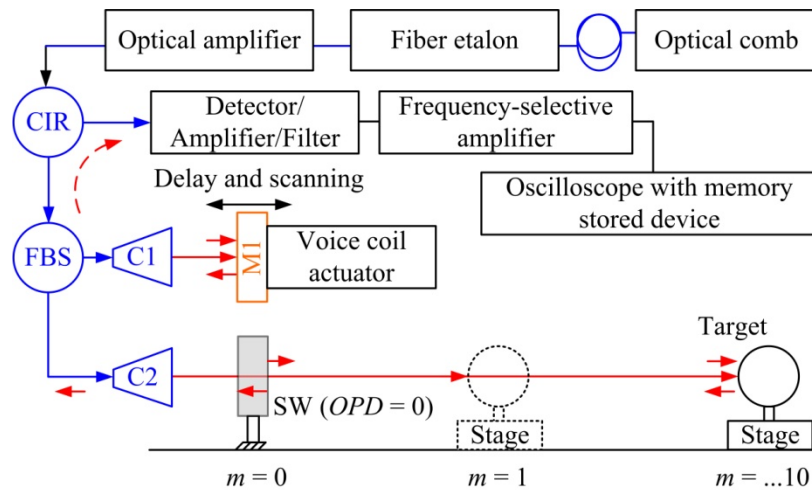
Fig. 4.8 Experimental setup diagram of preliminary measurement up to 1.5 m; a rough metal ball is used as the target and the target positions are changed by approximately of 150 mm for each length.

From this experiment, the laser power is reduced by a fiber etalon. In addition, the surface roughness of the target also affects the intensity of the laser beam that returns to the interferometer. As a result, the power of interference fringe signal was too small, hardly detected by using only a simple optical detector. Consequently, a frequency-selective amplifier was used to amplify a small interference fringe signal. Noise was also rejected by this

technique. The measurement results are shown in **Fig. 4.9**, which the measurement performance of the proposed technique is evaluated by the repeatability of the measurement of each position. The maximum standard deviation is approximately 1 μm for the absolute lengths up to 1.5 m. However, this measurement was done in a laboratory without control of air temperature and humidity. The environmental conditions swing between (19.9–22.3) °C, (23.7–28.4) %RH, and (99.7–100.9) kPa for the air temperature, air humidity, and air pressure, respectively.
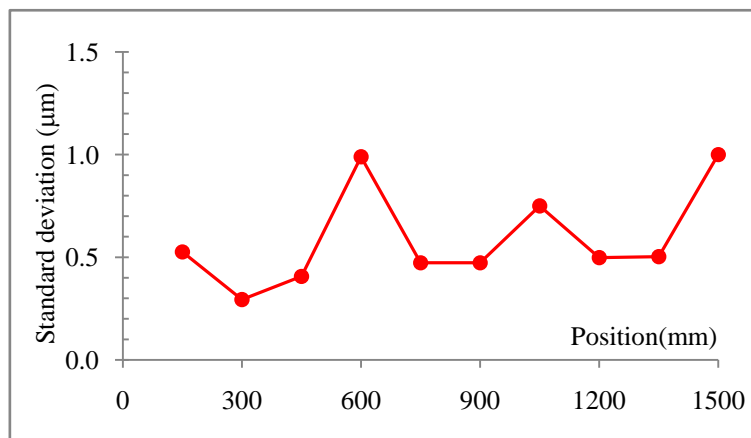
Fig. 4.9 Standard deviations of preliminary experimental measurement.

The surface roughness of the target is significant to the precision of length measurement [58, 60]. Surface roughness directly affects interference fringe acquisition. The suitable target surface is a factor that must be considered for applications with a high accuracy requirement. Moreover, the roundness and diameter tolerance of the target should also be considered for possible applications. When a metal ball with a diameter of 25 mm is used as the target, a beam misalignment of ± 0.2 mm from the center of the ball will cause an error of length measurement of ~1 μm. However, the error also depends on the surface roughness, roundness, and laser beam diameter. From experiments also found that using a focusing beam, the repeatability of measurement was improved over using a small spot beam and a large beam diameter. However, the laser beam will be lost when the ball is moved far away from its position. On the other hand, the laser beam is tiny lost respectively when using a small spot beam and a large beam diameter, but this presents a large standard deviation.
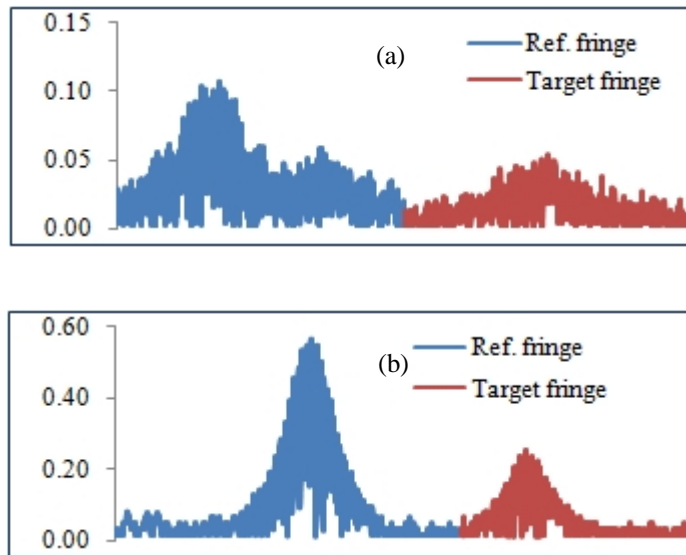
Fig. 4.10 Interference fringes (a) before, and (b) after passing through a frequency-selective amplifier.

Additionally, although an etalon plays the role of frequency mode selector for this application, but the power of the laser is reduced by property of a fiber etalon. Therefore, the consideration of reference mirror type should not only achieve a good transmission but also sufficiently reflects the laser beam to produce a reference fringe. From the experiment, a sapphire window plate was selected as a reference position ($m = 0$) because its transmission property is appropriate for a laser wavelength in the range of 1.56 μm. This means the laser power is slightly reduced when the laser passes through a sapphire window plate. Furthermore, an optical amplifier was used to gain the laser power. The interference-fringe signals were amplified by a frequency-selective amplifier. It was sufficiently powerful to gain a small signal and reduce noise. Although the power of the laser beam was reduced by an etalon, and the interference fringes were also influenced by the surface roughness of the target, the signal-to-noise ratio of the small signals was improved by a frequency-selective amplifier. It was apparent that the noise was rejected and the interference fringes intensity was amplified, as shown in **Fig. 4.10**. Consequently, the interference fringes were captured, and the length observations were also measured.

4.3 CMM positioning accuracy measurement

The rough metal ball with *Ra* approximately 0.1 μm was used as the target of a single-mode fiber interferometer for the positioning accuracy measurement of a CMM. The single-mode optical fiber more than 100 m long was used to connect a laser source from the 10th floor of a building to the measuring system inside a CMM room in the basement of the building. Then, the positioning accuracy of a CMM was measured and compared with a commercial cw-laser interferometer. The measurement setup is shown in **Fig. 4.11**.
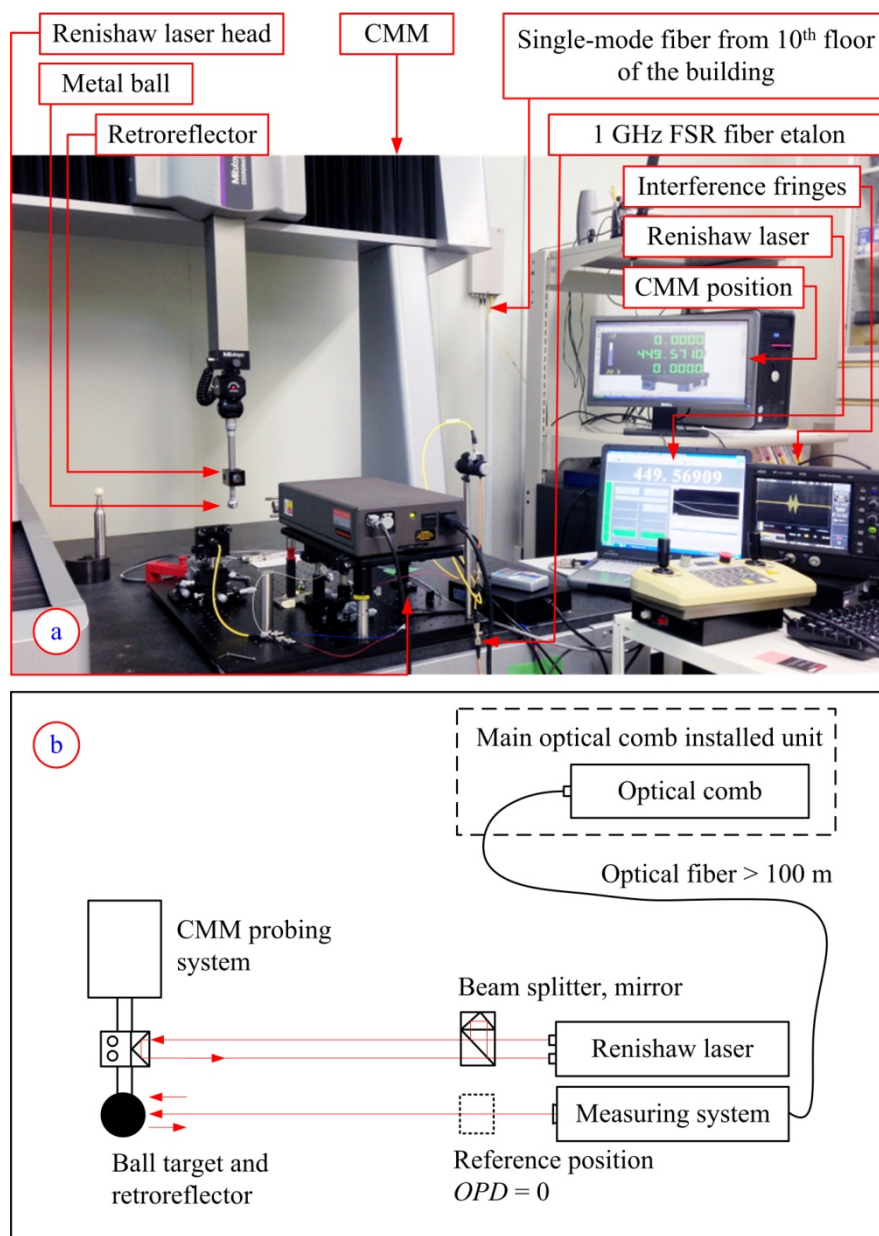
Fig. 4.11 CMM positioning accuracy measurements: (a) is the photograph of measurement comparison, (b) is the measurement setup diagram.

The rough metal ball with a diameter of 25 mm and a retroreflector were attached to the probing system of a CMM. The moving bridge-type CMM (FALCIO APEX 707, Mitutoyo) was measured in this experiment. The positions of measurement were controlled by the CMM controller. Then, the linear positions of a CMM were measured by the Renishaw laser interferometer and the single-mode fiber optical-comb pulsed interferometer. This experiment was conducted in an environmental control room. The average air temperature, relative humidity and air pressure were approximately 22.35 ℃, 21.1 %RH, and 100.40 kPa, respectively. The measurement results of five time repetitions are summarized in **Table 4.2**.

Table 4.2 Positioning measurement results of *y*-axis of a CMM.

CMM position (mm)	Pulsed interferometer (mm)	Positioning error 1 (μm)	Standard deviation (μm)
0.000	0.0000	0.00	0.00
149.857	149.8557	1.31	0.29
299.714	299.7127	1.33	0.41
449.571	449.5690	2.01	0.47
CMM position (mm)	Renishaw interferometer (mm)	Positioning error 2 (μm)	Standard deviation (μm)
0.000	0.0000	0.00	0.00
149.857	149.8559	1.11	0.14
299.714	299.7126	1.43	0.21
449.571	449.5692	1.77	0.24

The measurement results shown in **Table 4.2** were corrected for the refractive index of air to the reference temperature, 20 ℃ [61]. The positioning error 1 shows the position errors of a CMM that are determined by the different lengths of the CMM positions and the lengths which are measured by a single-mode fiber optical-comb pulsed interferometer. The positioning error 2 is the different lengths of the CMM positions and the lengths which are measured by the Renishaw laser interferometer. The maximum standard deviation of the measurement is approximately 0.47 μm for the proposed measuring system and 0.24 μm for the Renishaw laser interferometer.
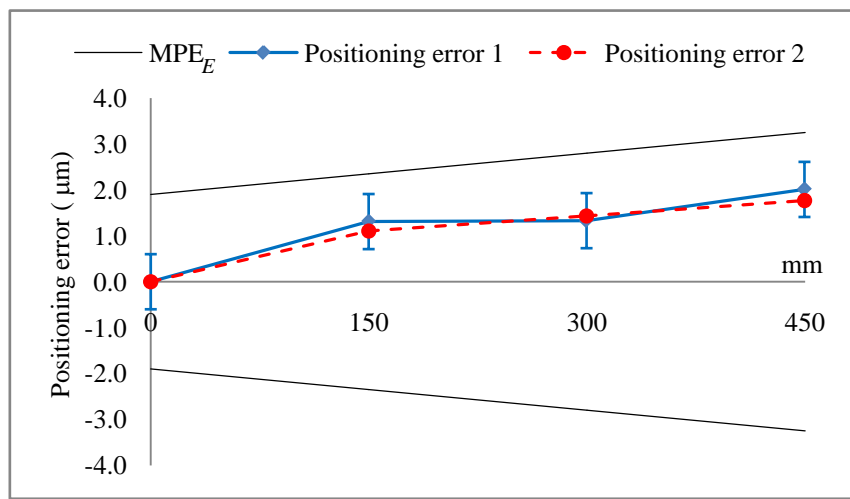
Fig. 4.12 Positioning errors of *y*-axis of a CMM; the blue-solid line is the positioning errors of a CMM with uncertainty bar of the measurement. The red-dash line is the positioning errors of a CMM that measured by Renishaw laser interferometer, and the black lines are the maximum permissible error of indication of a CMM for size measurement.

Graph in **Fig. 4.12** shows the position errors with measurement uncertainties of the *y*-axis of a CMM pairing with the maximum permissible error of indication of a CMM for size measurement—[$MPE_E = \pm(1.9 + 3L/1000)$] μm, where *L* is the indication length of a CMM expressed in mm. This graph indicates that the position errors of a CMM show the same trends when measured by both interferometers. The maximum difference between two curves is approximately 0.24 μm. These results suggest that the proposed measuring system can be applied successfully with high accuracy for industrial CMMs.

However, the maximum permissible error of a CMM includes usage of a contact probing system when the measurement is performed. On the other hand, the proposed measuring system is a non-contact type of measurement, and does not contain the effect of the probing error. The uncertainties of this measurement are discussed in **Section 4.4.3**.

73

4.4 Measurement uncertainty

4.4.1 Overview

When reporting the result of a measurement of a physical quantity, some quantitative indication of the quality of the result should be given, so that who use it can assess its reliability. Without such an indication, measurement results cannot be compared, either among themselves or with reference values given in a specification or standard. It is therefore necessary that there be a readily implemented, easily understood, and generally accepted procedure for characterizing the quality of a result of a measurement that is for evaluating and expressing its uncertainty [4, 62–63]. The concept of uncertainty is that when all of the known or suspected components of error have been evaluated and the appropriate corrections have been applied, there still remains an uncertainty about the correctness of the stated result, that is, a doubt about how well the result of the measurement represents the value of the quantity being measured.

4.4.2 Uncertainty evaluation

The measurement uncertainty associated with the input estimates is evaluated according to either a "type A" or a "type B" method of evaluation.

The type A evaluation of standard uncertainty is the method of evaluating the uncertainty by the statistical analysis of a series of observations. This case the standard uncertainty is the experimental standard deviation of the mean that follows from an averaging procedure or an appropriate regression analysis as **Eq. (4.1)**.

$$u_A = s(\overline{q}) \tag{4.1}$$

where $s(\overline{q})$ is the termed experimental standard deviation of the mean. The type A evaluation of standard uncertainty can be applied when several independent observations have been made for one of the input quantities under the same conditions of measurement.

The type B evaluation of standard uncertainty is the method of evaluating the uncertainty by means other than the statistical analysis of a series of observations. This case the evaluation of the standard uncertainty is based on some other scientific knowledge. The standard uncertainty $u(x_i)$ is evaluated by scientific judgments based on all available information on the possible variability of x_i. Values belonging to this category may be derived from previous measurement data such as manufacturer's specifications, data provided in calibration and other certificates, uncertainties assigned to reference data taken from handbooks.

For uncorrelated input quantities the square of the standard uncertainty associated with the output estimate y is given by **Eq. (4.2)**, called combined standard uncertainty.

$$u_c^2(y) = \sum_{i=1}^{N} u_i^2(y) \tag{4.2}$$

The quantity $u_i(y)$, where $(i = 1, 2,\dots N)$ is the contribution to the standard uncertainty associated with the output estimate y resulting from the standard uncertainty associated with the input estimate x_i as:

$$u_i(y) = c_i u(x_i) \tag{4.3}$$

where c_i is the sensitivity coefficient associated with the input estimate x_i. It is determined from the partial derivative of the mathematical model function of the measurement. The sensitivity coefficient c_i describes the extent to which the output estimate y is influenced by variations of the input estimate x_i.

Generally, the measurement uncertainty is stated an expanded uncertainty of measurement (U), obtained by multiplying the standard uncertainty $u_c(y)$ of the output estimate y by a coverage factor k, ($U = ku_c(y)$). In cases where a normal (Gaussian) distribution can be attributed to the measurand and the standard uncertainty associated with the output estimate has sufficient reliability, the standard coverage factor $k = 2$ shall be used. The assigned expanded uncertainty corresponds to a coverage probability of approximately 95%. These conditions are fulfilled in the majority of cases encountered in calibration work. The result of a measurement is then conveniently expressed as $Y = y \pm U$, which is interpreted to mean that the best estimate of the value attributable to the measurand Y is y, and that $y - U$ to $y + U$ is an interval that may be expected to encompass a large fraction of the distribution of values that could reasonably be attributed to Y. Such an interval is also expressed as $y - U \leq Y \leq y + U$.

4.4.3 The recommended standard uncertainty of CMM verification

General guidelines of uncertainty evaluation of the test CMM for size measurements are presented in the standard of ISO/TS 23165:2006. However, the standard uncertainty model does not include uncertainty sources from CMM under test. Uncertainties are evaluated by sources of the material standard of size and environmental conditions, because this standard is the evaluation of the test uncertainty required for the decision rules for proving conformity or nonconformity with specifications.

However, the uncertainty of CMM verification depends on material standard usage, environmental conditions, and measurement procedure. The recommended standard uncertainty of the error of indication should consist of uncertainty due to;

- The calibration of the material standards of size.
- The CTE (coefficient of thermal expansion).
- The temperature variation.
- Misalignment of the material standard of size.
- Finite resolution of a CMM.
- CMM repeatability.
- CMM stability.

It should be noted that some parameters can be neglected, which depend on measurement procedure. For example, cosine error due to misalignment of the material standard of size can be ignored if alignment process is the same as calibration procedure. On the other hand, more uncertainty sources should be added such as the following cases may be concerned in some applications.

- If the material standard of size is not fully demagnetized, the stylus may be attracted and give false measurements that may be caused by magnetisation of the material standard of size.
- When the material standard of size is either resting or hanging in a vertical position, its own weight will either compress or expand it, respectively.
- Based on artifact test method, gauge deformation due to supporing stand may affect to length standards.

4.4.4 Uncertainty of a CMM positioning accuracy measurement

The uncertainty of a CMM positioning accuracy measurements based on proposed measuring system has been evaluated following the recommended guideline [4, 62–63]. The sources of errors under consideration may be divided into three groups. The first group involves with the modified frequency source of the optical comb by the Fabry–Pérot fiber etalon. The stability of the repetition frequency after passing a Fabry–Pérot fiber etalon is in the order of 10^{-9} over 2 h [33]. This case is a partial contribution of uncertainty approximately $0.5 \times 10^{-9} l$, which is divided by the rectangular distribution, because of semi-range limits of a finite resolution of the used instrument. However, the repetition rate accuracy of the optical frequency comb is not changed because the performance of etalon is only filtering of the comb. Therefore, the uncertainty of the repetition rate and carrier offset frequency is canceled because the accuracy ratio with the MPE_E of a CMM is more than 100 times better.

The second group includes the environmental conditions, the compensation of the group refractive index of air, and thermal expansion of linear scale of a CMM. Because of the measurement errors of environmental conditions (air temperature, air pressure and, air humidity) during measurement, the contribution uncertainty of each parameter were determined by the standard uncertainty of each parameter multiple by their sensitivity coefficients. Therefore, the compensation uncertainty for the refractive index of air was calculated to be $3.08 \times 10^{-7}l$, where l is the indication length of a CMM. It was a root of square-sum of distribution uncertainties of air temperature, air pressure, air humidity and uncertainty of Cidder's formula. Next, the coefficient of thermal expansion of the linear scale of a CMM is approximately of 8.0 μm m^{-1}K^{-1} with an uncertainty of ± 1 μm m^{-1}K^{-1}. In this experiment, the changes of temperature of linear scale of a CMM cannot be directly measured. Therefore, the uncertainty due to thermal expansion of linear scale of a CMM was determined from the changes of air temperature, because thermal expansion effect of a CMM was automatically compensated to reference temperature (20 ℃) by CMM's software, and the measurement values of the air temperature are generally utilized in the place of the scale temperature.

The last group involves with the measurement procedures such as measurement repeatability and the uncertainty of conversion time to length scale measurement. The uncertainty of measurement repeatability was approximately 0.21 μm, which was evaluated from the maximum standard deviation of five times of measurement repetitions. The uncertainty due to the conversion of time to length scale measurement is evaluated from the maximum deviation of the measured values and the best-fit line [58]. It was assumed to be a rectangular distribution, and was approximately 0.18 μm. In addition, the digital scale interval of the linear scale of CMM is 0.001 mm (the resolution in X, Y, and Z axes of a CMM are 0.0001 mm. In the experimental measurement, the resolution of a CMM was rounded of the reading at the digit of 1 μm). Variations due to this finite resolution were estimated to have rectangular limits of 0.5 μm. From above evaluation, the error sources and their uncertainties of the measurement are summarized in **Table 4.3**

Based on uncertainty estimation, if the uncertainties due to a CMM are ignored because of dependent upon machines, the measurement capability of the proposed measuring system is approximately 0.64 μm for indication length of 1 m. The major uncertainty source is the repeatability of the measurement because it depends on the acquisition of the envelope interference fringes. Those fringes are sensitive to mechanical vibrations and air-flow fluctuations (repeatability of a CMM is a part that affects the measurement repeatability). Furthermore, the repeatability of the envelope interference fringes is also affected by the inconstant speed of a scanning device. In this evaluation, the uncertainty due to the roundness

of the target is not included, because this error does not affect the positioning accuracy verification in one-directional measurement. Alternatively, roundness error has to be concerned for three-dimensional applications.

Table 4.3 Uncertainty of CMM positioning accuracy measurement.

Uncertainty sources	Standard uncertainty, (x_i)	Sensitivity coefficient, c_i	Uncertainty contribution, $u(y_i)$
Sources from interferometer			
Repetition frequency stability	$2.89 \times 10^{-10}\, l$	1	$2.89 \times 10^{-10}\, l$
Refractive index of air compensation			
−Ciddor's equation	$< 10^{-8}$	l	$1.00 \times 10^{-8}\, l$
−Air humidity	0.25 %RH	$6.02 \times 10^{-8}\, l/\%RH$	$1.49 \times 10^{-8}\, l$
−Air temperature	0.15 °C	$5.66 \times 10^{-7}\, l/°C$	$2.03 \times 10^{-7}\, l$
−Air pressure	64.00 Pa	$2.66 \times 10^{-9}\, l/Pa$	$1.70 \times 10^{-7}\, l$
Conversion of time to length scale	1.79×10^{-4} mm	1	1.79×10^{-4} mm
Combined uncertainty	$0.18\ \mu m + 2.65 \times 10^{-7} l$		
Sources from CMM			
Thermal expansion of linear scale	$5.77 \times 10^{-7}\, °C^{-1}$	$0.62\ °C\ l$	$3.58 \times 10^{-7}\, l$
Finite resolution	2.89×10^{-4} mm	1	2.89×10^{-4} mm
Measurement repeatability	2.10×10^{-4} mm	1	1.79×10^{-4} mm
Combined uncertainty	$0.36\ \mu m + 3.58 \times 10^{-7} l$		
Expanded uncertainty ($k = 2$)	$[(0.80)^2 + (0.89 \times 10^{-3} l)^2]^{1/2}\ \mu m$		

Note: l is the indication length of a CMM expressed in mm.

4.5 Chapter conclusion

As previous mention, we are looking for a target that can be used as a target of a single-mode fiber optical-comb pulsed interferometer in three-dimensional measurement. In this chapter spherical targets produced by metal material have been considered. The effects of the roughness of the target to the absolute-length measurement had been studied first. Using a surface roughness scale standard plate with differences of Ra values as the target of interferometer, the relation of measurement standard deviation and power intensity of interference fringe can be summarized as shown in **Fig. 4.13**.
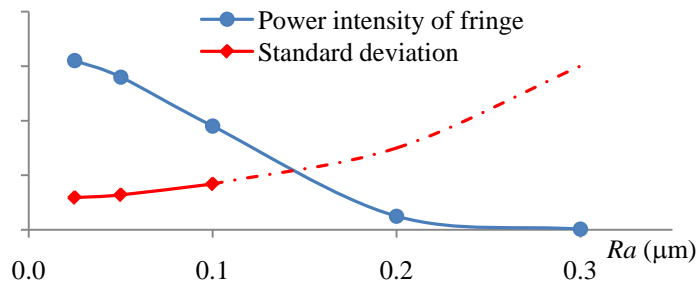
Fig. 4.13 Relation of power intensity of interference fringe, and measurement standard deviation corresponding to the surface roughness of the target.

Interference fringe produced by the target is enhanced, when surface of target is smooth (small of Ra). The power is gradually decreased, when Ra of target is increased. If Ra is larger than 0.2 μm, it cannot be used as the target of interferometer because it cannot reflect the laser beam back to interferometer. For the measurement standard deviation, a smooth surface presents a small standard deviation than a rough surface. However, using a spherical target type is unlike a plane target. The laser beam is difficultly alignment if surface of a spherical target is too smooth, because only a small area at the center of the target can reflect laser beam back to the single-mode fiber optical-comb pulsed interferometer; other areas reject the beam. For that reason, a rough metal ball with Ra is approximately 0.1 μm had been considered as the target of interferometer for CMM application.

The absolute length can be performed up to 1.5 m by using a rough metal ball. However, the laser beam misalignment of ± 0.2 mm from the center of the target will cause an error of length measurement approximately 1 μm, and cosine error is approximately 1.3 μm. In case of applying this target for CMM positioning accuracy measurement, although measured results are the same trend with a commercial laser interferometer, but the proposed measuring system presents measurement standard deviation two times larger than a commercial cw-laser

interferometer. In addition, the major uncertainty source is the measurement repeatability because it relates to the data acquisition of the envelope interference fringes. The efficient interference fringes depend on the laser beam that is reflected by the target. Furthermore, the envelope interference fringes are affected by the inconstant speed of a scanning device and environmental conditions.

According to previous experimental measurements, the limitation of the targets for the proposed measuring system can be summarized as **Table 4.4**.

Table 4.4 The limitation of target types for the proposed measuring system.

Target types	Limitations
Flat mirror	- Target provides only one dimension of the measurement.
Cube mirror	- Target provides only one dimension of the measurement.
Rough surface	- Target provides only one dimension of the measurement; - Rough surface reduce power intensity of fringe; - Rising of *Ra*, increasing measurement standard deviation; - Too rough surface cannot be used as the target.
Cat's eye retroreflector	- Target provides three dimension of the measurement, but observation angle is limited.
Metal ball	- Target provides three dimension of the measurement, but measuring range is limited ~1.5 m; - It presents a large measurement repeatability; - Laser alignment is difficult if $Ra \ll 0.1$ μm ; - Cannot be used as the target if $Ra \gg 0.1$ μm.
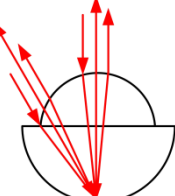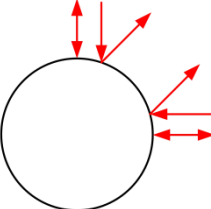
This research aims to use a spherical target type because it can be served as a three dimensional target for a single-mode fiber optical-comb pulsed interferometer. Although a rough metal ball provides three dimensional target, but measuring range is limited around 1.5 m. The measuring length is limited by the laser power that is reflected from the target to the interferometer. This limitation also involves with the splitting power ratio of the FBS. The splitting power of the FBS, which is 10% for the scanning arm and 90% for the measuring arm, is selected, because the traveling beam of the measuring arm is affected by surrounding conditions than the scanning arm, and the long-path beam travels in air, while the scanning arm almost light travel inside the single-mode optical fiber. The measuring range may be shorter than 1.5 m if the beam splitting ratios of the measuring arm is less than 90%.

However, the experimental results show that the longest length, which can be measured by measuring system as shown in **Fig. 4.8**, is approximately 1.5 m. No any signal return back to the interferometer if the measuring lengths are over 1.5 m. In addition, the rough surface of a rough metal ball is inefficient light reflection, especially at the long length of the measurement. A rough surface randomly reflects the laser light. As a result, a weak interference fringe signal is produced. That is simply destroyed by environmental conditions, and presents large measurement repeatability. In contrast, a smooth surface gives a small measurement standard deviation than a rough surface, but the laser alignment is troublesome in case of a spherical target type, because only a small area at the center of the target efficiently reflects the laser beam back to interferometer; other areas reject the laser beam. However, a rough metal ball can be applied for non-contact measurements in dimensional field, which is not too high accuracy requirement such as arm CMM or robotic arm measurements [60].

According to rough metal ball targets cannot be served for the long range of the measurement, (Our goal is approximately 10 m) and it present a large measurement uncertainty, the ball lens with a refractive index of 2 had been studied as the target of a single-mode fiber optical-comb pulsed interferometer. It can be served for the absolute-length measurement up to 10 m, and provides powerful interference fringes. More details are discussed in the next chapter.

Chapter 5 The space diagonals of a CMM verification using a ball lens target

5.1 Introduction

This chapter mainly discusses about the diagonal in space verification of a CMM by using a ball lens target, which acts as a retroreflector of a single-mode fiber optical-comb pulsed interferometer. General a retroreflector is an optical device that is widely used in length measurements based on interferometer. Two broad categories are commonly used; one is a cube-corner mirror and the other is a cat's-eye retroreflector. Both retroreflectors are limited on viewing angle in three-dimensional applications. This research aims to develop a measuring system that can be measure absolute length in all directions of the measurement setup. Therefore, the ball lens with a refractive index of 2 and a diameter of 10 mm was studied as the target of a single-mode fiber optical-comb pulsed interferometer because it can acts as a function of a retroreflector. Moreover, it can be served as the target for all directions in applications.

In application, a ball lens target is assembled on the CMM probing system instated of a stylus tip. The parameters affect to the optical path length such as the sphericity and the refractive index of a ball lens target are considered. The total accuracy of a ball lens target depends on both the accuracy of the refractive index of glass material and that of the spherical fabrication. The optical path error due to imperfect of a ball lens is demonstrated by the simplest experiment using an unbalanced-arm Michelson interferometer. Subsequently, the measurement repeatability is evaluated by preliminary experimental measurement up to 3 m, and efficiency for the long-measuring lengths is demonstrated. Experiments show that how long a single-mode fiber optical-comb pulsed interferometer with a ball lens target can be used to verify a CMM. Finally, a moving-bridge type CMM has been verified by the proposed measuring system in four space diagonals comparing with a standard artifact test method. Moreover, the uncertainties of diagonal measurements of both techniques are discussed at the end of this chapter.

.

5.2 Ball lens target

Generally, ball lenses are manufactured from a single substrate of glass such as S-LAH79, which has a density of 5.23g/cm^3 and coefficient of linear expansion of approximately 6.0 µm/m°C. Ball lenses are great optical components for improving signal coupling between fibers, emitters, and detectors. They are also used in endoscopy, bar code scanning, ball pre-forms for aspheric lenses, and sensor applications. In addition, they also can be used as a retroreflector.

To understand how a ball lens can be applied as a retroreflector, it should be started from cat's-eye retroreflector fabrication as show in **Fig 5.1 (a)**, which shows the principle of an ordinary cat's-eye retroreflector. This figure presents the cross section of the cat's-eye retroreflector, where two concentric hemispheres having different radii are adhered together. The larger hemisphere is covered by a total-reflection coating. Assuming r_1 and r_2 are the radii of the small and the large hemisphere and the refractive index of the glass is n. The cat's-eye retroreflector is fabricated to satisfy as **Eq. (5.1)** [64].

$$r_1 = (n-1)r_2 \qquad (5.1)$$

If a light beam incident to the small hemisphere, it will be focused on the surface of the large hemisphere in the glass. The reflected light beam traces the same path in the opposite direction. This is a function of a retroreflector.
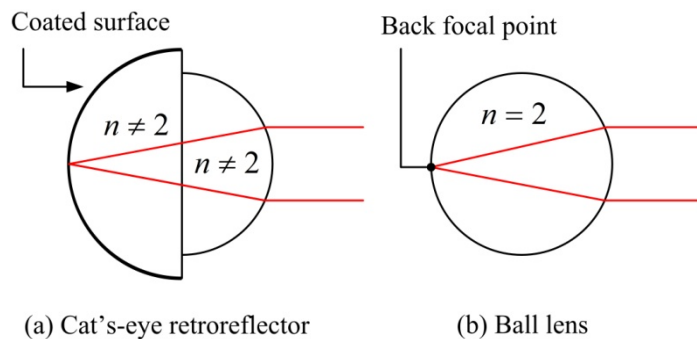
Fig. 5.1 Structure of the target; (a) is a cat's-eye retroreflector ($n \neq 2$), and (b) is ball lens ($n = 2$).

In case of a cat's-eye retroreflector, the refractive index n of glass material is not equal to 2. On the other hand, if the refractive index of glass material in **Eq. 5.1** equals to $n = 2$, then $r_1 = r_2$. That means the diameters of the two hemispheres are equal and consequently a sphere having a refractive index of 2 is the same property of a retroreflector as shown in **Fig. 5.1 (b)**.

Therefore, this sphere is free from problems due to misalignment of the centre of the two hemispheres, and from any undesirable effects of the adhesives used to join the two hemispheres [64, 65]. For that reason, a ball lens that has a refractive index of 2 can be used as a retroreflector of the interferometer. In addition, it can be applied to measure absolute lengths in all directions of the measurement setup, which is met the requirement of this research objects. Using a ball lens, some parameters have to understand as shown in **Fig. 5.2.**
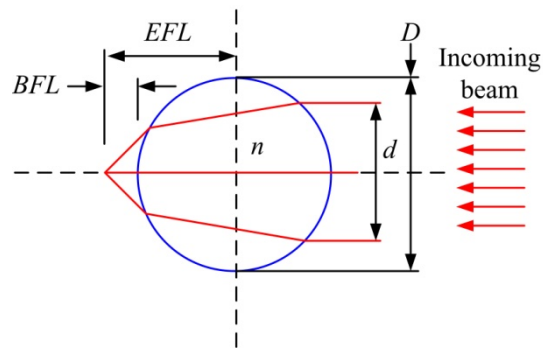
Fig. 5.2 Key parameter of a ball lens: *d* is diameter of input source, *D* is diameter of ball lens, *EFL* is the effective focal length, *BFL* is the back focal length, and *n* is the index of reflection of ball lens.

The effective focal length (*EFL*) is very simple to calculate that is measured from the center of the ball lens as **Eq. (5.2)**, since there are only two variables involved, there are diameter of ball lens and index of refraction. The back focal length (*BFL*) is easily calculated as **Eq. (5.3)** when the *EFL* and the diameter of ball lens (*D*) are known.

$$EFL = \frac{nD}{4(n-1)} \tag{5.2}$$

$$BFL = EFL - \frac{D}{2} \tag{5.3}$$

In this research, a ball lens (S-LAH79, Ohara) having a refractive index of 2 and a diameter of 10 mm is used as the target of a single-mode fiber optical-comb pulse interferometer. Thus, the *EFL* is calculated to be 5 mm, and the *BFL* become zero. Hence, the back focal point of a ball lens is the end of its surface. When this ball lens is employed as the target of interferometer, the entire incoming beam will fall to the end surface at the back focal point as shown in **Fig. 5.1 (b)**

5.2.1 Ball lens target and optical path error

The total accuracy of the ball lens target depends on the accuracies of both the refractive index of glass material and the spherical fabrication. For one-dimensional length measurements, the sphericity of the ball lens does not affect to the optical path difference, but it significantly affect to three-dimensional length measurements. The following experiment demonstrates the simplest method to determine the contribution of a ball lens target to optical path error as shown in **Fig.5.3**.
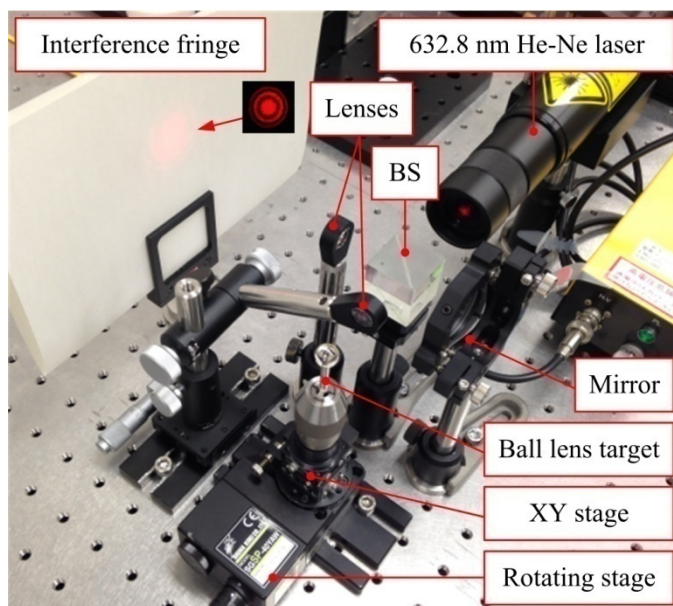
Fig. 5.3 Experiment setup of a ball lens target to optical path error.

The experimental setup is based on a general unbalanced-arm Michelson interferometer. A long-coherence light source (632.8 nm He-Ne laser, NEOARK) served as a light source of interferometer. The laser beam was divided by a beam splitter (BS). One beam was collimated by a lens to the back focal point of a ball lens target, and other was incident on the reference mirror. The reflected beams from the target and the reference mirror are recombined to produce a pattern fringe on an imaging screen. First of all, the ball lens was positioned to be concentric with a rotary stage by adjusting an *XY* translation stage for avoiding errors of stage rotation. The laser beam was then aligned until a fringe pattern appeared. The ball lens was rotated by the rotating stage controller, and the pattern fringe on the screen was observed.

In this experiment, the pattern fringe did not change during ball lens rotation. It can be implied that the ball lens caused an optical path error of less than one half of the laser

wavelength, i.e., less than 0.3 μm. However, vibration of the rotating stage directly affects to the fringe pattern. Therefore, a precise, smoothly rotary stage is required in order to achieve higher precision of the observed fringe pattern. A highly-accurate roundness measuring machine to confirm the roundness accuracy of the target is an alternative. However, for one-dimensional length measurements, the sphericity of the ball lens does not affect the optical path difference, but it does significantly affect three-dimensional lengths. Thus, using the proposed method, the error due to the target can be ignored for CMM diagonal measurements.

5.2.2 Optical path error due to misalignment

Although a ball lens acts as a function of a retroreflector, the laser beam alignment on the target is important to consider for avoiding unnecessary optical path error in the absolute-length measurement. In practice, if the laser beam is not incident at the center of a ball lens, but the entire incoming beams are the same parallel with a measuring line as shown in **Fig. 5.4 (a)**, they will fall to the back focal point into the end surface of a ball lens. Then, the reflected beam traces the same parallel path to the interferometer. In this case, the optical path is not affected by the target, but the laser power that reflected by the target will be weak if the beam shift too far from the measuring line, because the measuring system is a single-mode fiber interferometer. It requires the reflected beam return back to the interferometer as the same path with incident beam.

(a)

(b)
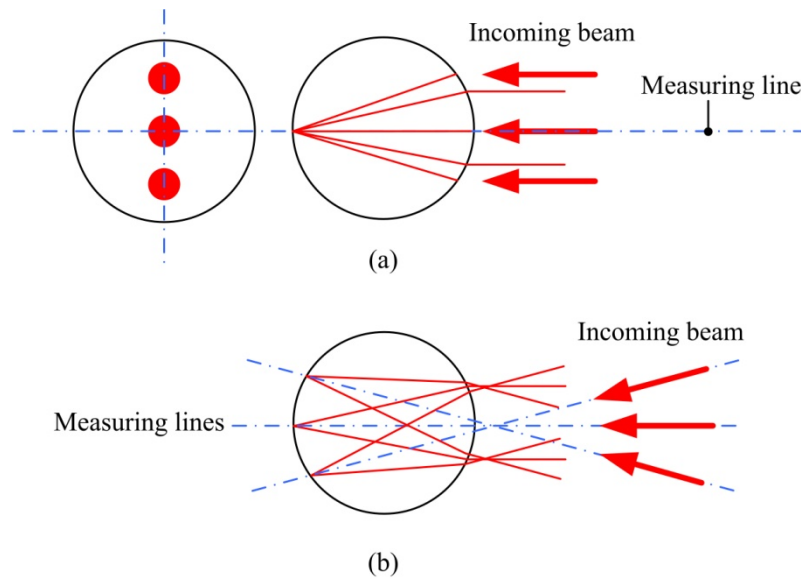
Fig. 5.4 Laser beam alignment on the ball lens target: (a) the entire incoming beams are the same parallel with a measuring line, (b) the measuring lines and the incident beams are different.

Alternatively, **Fig. 5.4 (b)** shows that the incoming beams are not incident as the same measuring line with others. In this case, the optical path lengths are exactly different. Therefore, it has to be concerned that the reflected beam traces the same path with incident beam. To avoid an optical path error due to misalignment of the laser beam on the target, it easily be solved by obtaining the maximum power intensity of the reflected beam from the initial position and the longest position of the measurement in the alignment process. However, an optical path error due to misalignment also depends on both of the laser beam diameter and a diameter of the target. It should be concerned that the laser beam must be aligned at the same axis with measuring line during measurement for avoiding unnecessary of an optical path error.

The following experiment demonstrates relationship between the power of reflected beam, which returns to interferometer and the beam position on a ball lens target. The experimental setup diagram is illustrated in **Fig. 5.5**.
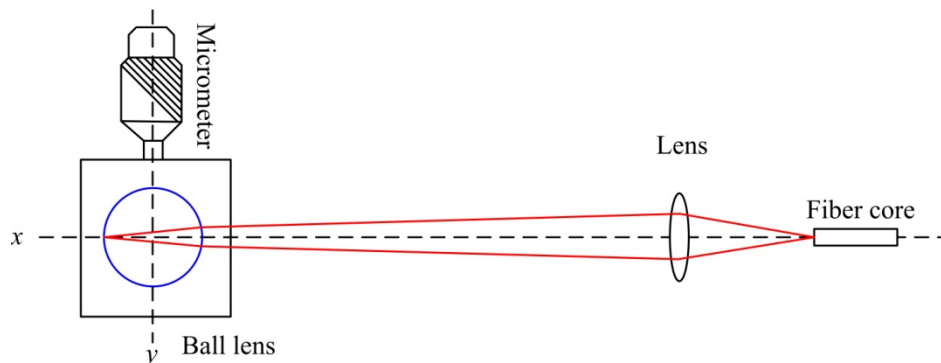
Fig. 5.5 The experimental setup diagram for determining relationship between reflected-beam intensity and the beam position on the target.

This experiment assumed that the incident beam and measuring line is the same direction in *x*-axis. Laser beam was collimated by a lens; a focal length of 30 mm. A ball lens target was fixed on a translation stage that placed perpendicular to incident beam. The location is approximately 3 m form a lens. First, laser beam was aligned close to the center of a target by obtaining the maximum power that returns to the output port of the CIR. Then, the target was moved in the direction of *y*-axis, each position and the power intensity of reflected beam were measured. Experimental measurement results are shown in **Fig. 5.6**.
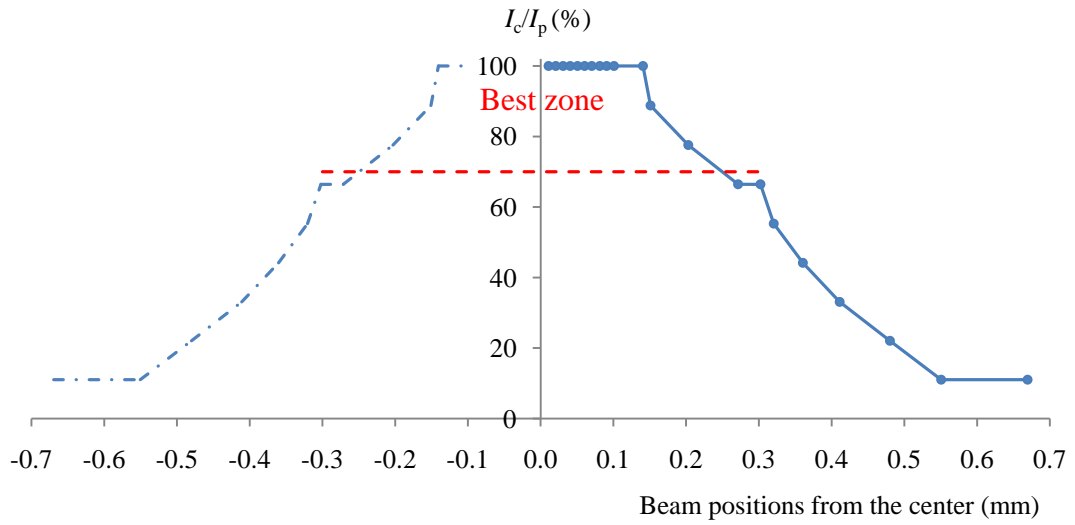
Fig. 5.6 Percentages of reflected-beam intensity to beam positions on a ball lens target.

The above result shows percentages of reflected-beam intensity to beam positions on a ball lens target, where I_c / I_p is the intensity ratios at the center (I_c) and each position (I_p) on the target. It indicates that the power of reflected-beam intensity is rapidly decreased, when the beam position far from the center of the target more than 0.15 mm. Due to a ball lens is a sphere, and both sides from the center are assumed to be symmetry boundaries. Thus, it can be implied that the reflected-beam intensity ratios maintain at 100%, if the laser beam is located around ± 0.15 mm close to the center of the target. The best area on the target for achieving a perfect interference fringe is that the ratio of reflected beam should be higher than 70% or around ± 0.3 mm from the center of target. However, this experiment results depend on both of the laser beam diameter and a diameter of the target. The small beam diameter on a large ball lens target enhances reflected beam power, because of the numerical aperture (NA) of the ball lens. From this experiment, the collimated beam is not a pure parallel beam. The laser beam diameter on the target is approximately 3 mm at the length of 3 m from a collimated lens. If laser beam is misalignment 0.3 mm, it may be cause of the cosine error less than 50 nm. Summary, optical path error due to misalignment on a ball lens target does not significant to absolute-length measurement, but we should play attention on the intensity of reflected beam, because a weak signal is simply destroyed by surrounding conditions.

5.3 Preliminary absolute-length measurement

The performances of a single-mode fiber optical-comb pulsed interferometer with a ball lens target in an open air have been studied. The absolute-length measurements are considered in a laboratory without control of air temperature and humidity. The measurement set up is shown in **Fig. 5.7**.
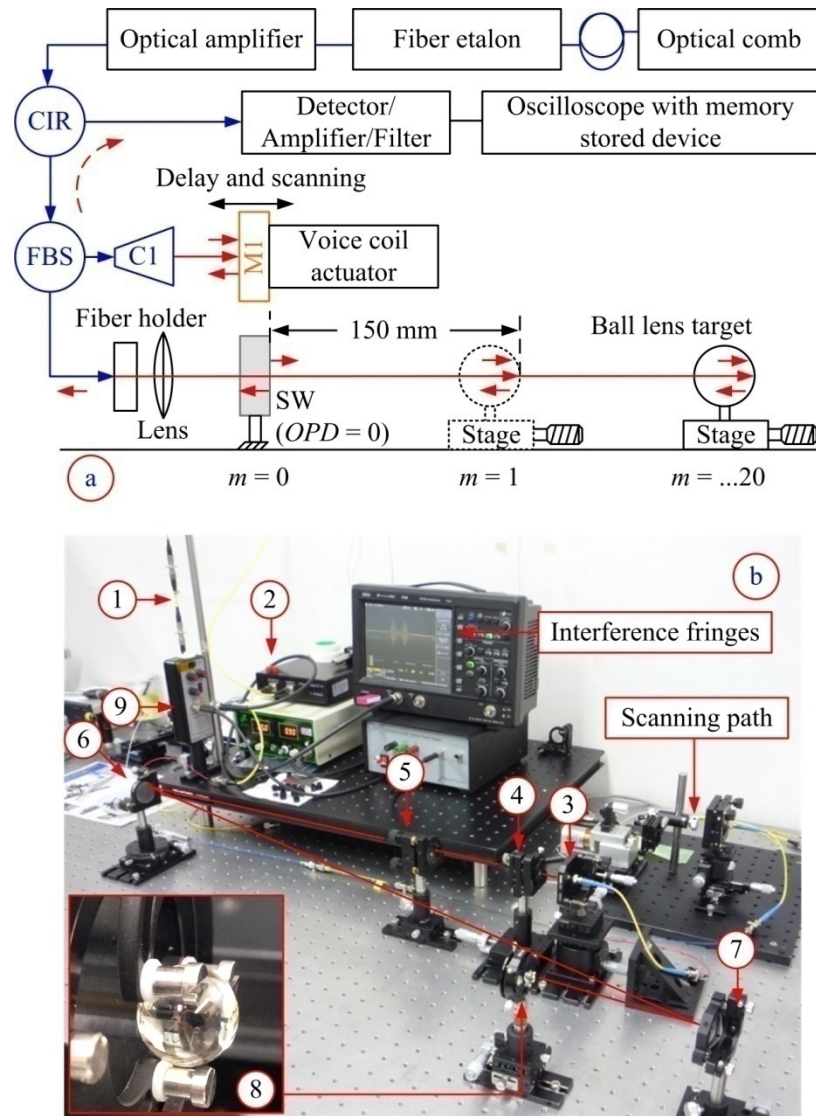
Fig. 5.7 Preliminary absolute-length measurement up to 3 m; (a) is measurement set up diagram, and (b) is photograph of the measurement; ① is a fiber etalon 1-GHz FSR, ② is an optical amplifier, ③ is a fiber holder, ④ is a lens, ⑤ is a reference position, ⑥⑦ are mirrors, and ⑧ is a ball lens.

The laser beam after through a fiber etalon was amplified by an optical amplifier, because the power intensity of the laser beam was reduced by a fiber etalon. The amplified beam crosses an optical fiber circulator (CIR) to a fiber beam splitter (FBS). After that, the laser was divided into two beams by the FBS. One beam was collimated by a collimator C1 into the direction of a scanning mirror M1, while other was collimated by a lens, transmitted through a sapphire window plate (SW) at the reference position and then the ball lens target. The absolute-length measurements were done by changing the positions of a ball lens target of approximately 150 mm to 3 m. Each position was measured five time repetitions. The environmental conditions during measurement were also recorded, which air temperature, relative humidity and air pressure were approximately (23.46 ± 0.15) °C, (48.6 ± 0.2) %RH and (101.09 ± 0.01) kPa. The measurement results were compensated by group refractive index of air following Ciddor's equation.
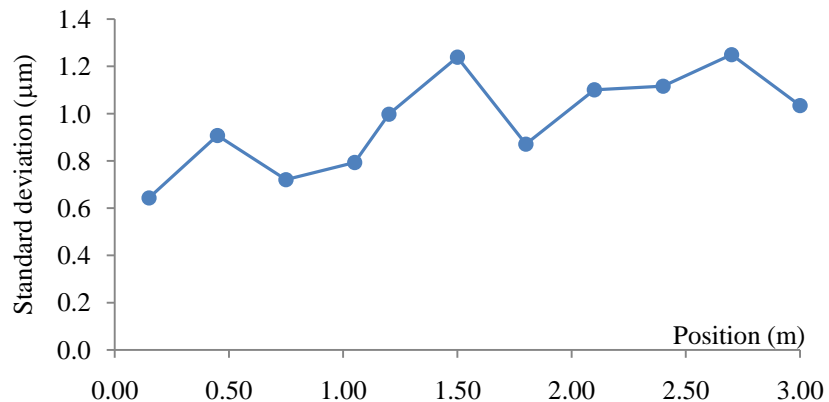
Fig. 5.8 The results of preliminary absolute-length measurement up to 3 m.

Preliminary absolute-length measurements up to 3 m have been conducted. The measurement results are shown in **Fig. 5.8**. The maximum measurement standard deviation is approximately 1.25 μm. Measurement standard deviation involves with the repeatability of envelope interference fringes. The result expresses that the noises of interference fringes are caused by air-flow fluctuations and mechanical vibrations. In addition, the trend of measurement standard deviation is slowly increased when the measuring lengths are extended. Interference fringes are not steady as a short measuring length, because the reflected-beam power from the target is diminished as mentioned in **Section 5.2.2**. These envelope interference fringes are easier destroyed by environment conditions. Furthermore, imprecise and unstable of a scanning device also affect repeatability of envelope interference fringes.

5.4 The measurement efficiency for long-measuring range

Once again, the efficiency of a single-mode fiber optical-comb pulsed interferometer with a ball lens target was studied for the long range of measurement. This experimental measurement demonstrates that how long the range of the proposed system can be performed.
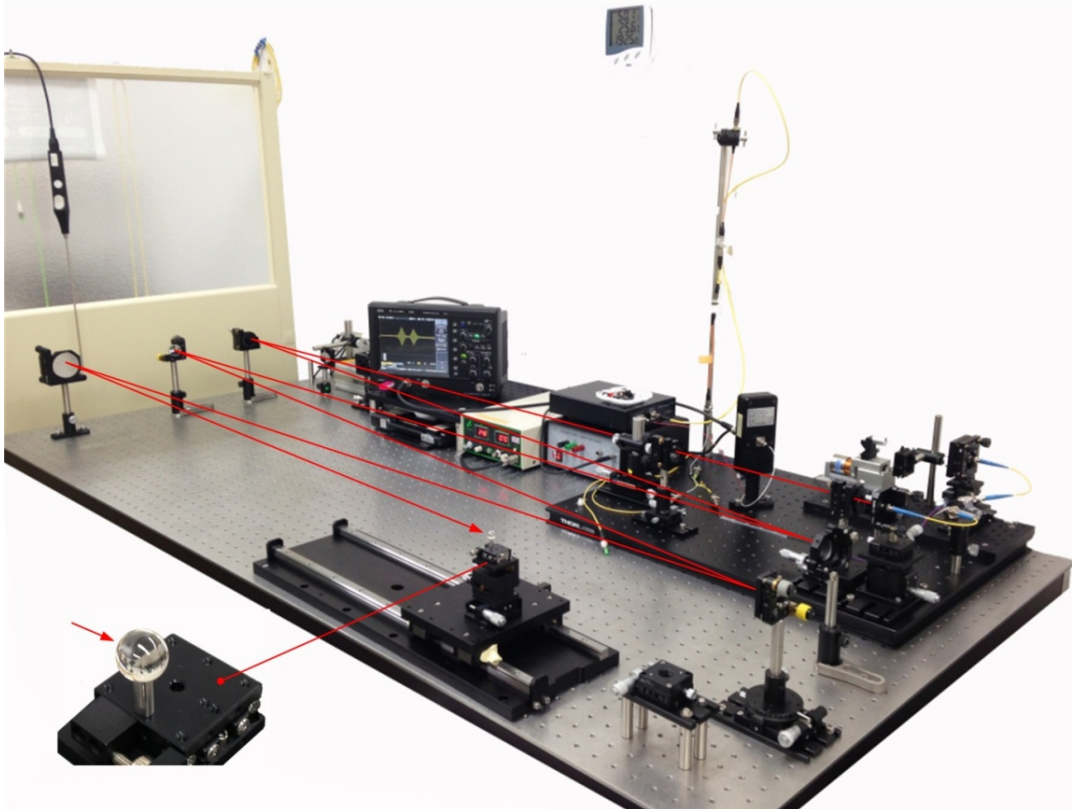
Fig. 5.9 Absolute-length measurement at the distance of 9 m.
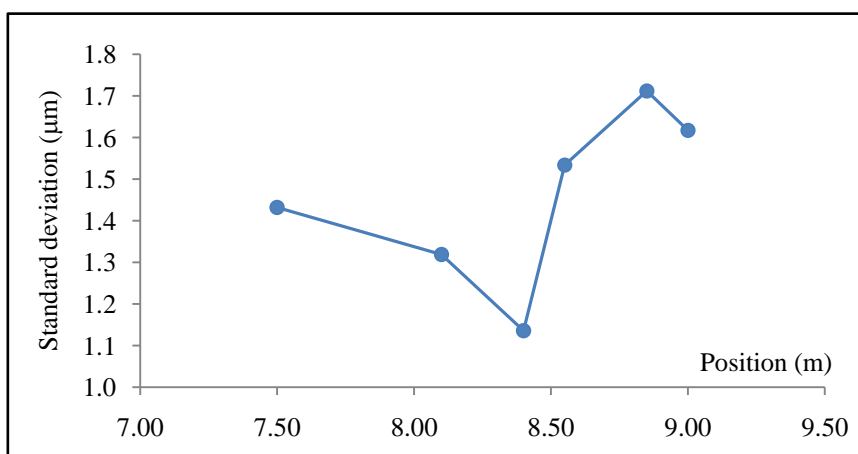
Fig. 5.10 The measurement standard deviations of the long-range measurements.

The measurement setup and optical components are the same as description in the previous section, but the distances of the target are positioned from 7.5 m to 9.0 m. The photograph of the measurement is shown in **Fig. 5.9**. Under uncontrolled-air laboratory, the measurement results are shown in **Fig. 5.10**. For five times measurement repetitions, the maximum standard deviation is approximately 1.62 μm. As the previous mention, the measurement standard deviation mainly involves with the repeatability of envelope interference fringes as discussed in **Section 5.3.**
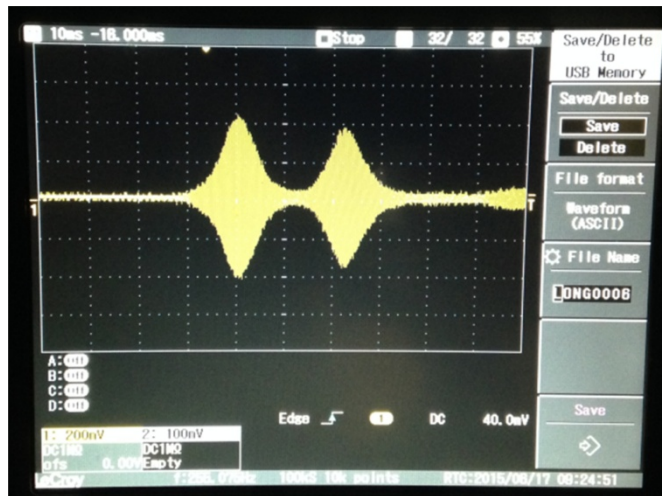
Fig. 5.11 Generated interference fringes at the absolute length of approximately 9.0 m.

Using a single-mode fiber optical-comb pulsed interferometer with a ball lens target, only the power intensity of the reflected beam from the target has to be concerned, because it is reduced by an etalon, and not at all of incident beam that is reflected back to the interferometer. Therefore, an efficient optical amplifier is required. Although the laser power is reduced, the signal-to-noise ratio of interference fringes are still satisfied for the long-length measurements and the interference fringes are sufficient enhanced for applications as shown in **Fig. 5.11**. This experiment result strongly indicates that the proposed measuring system is able to measured absolute length cover the range of CMM applications from a medium-sized to a large-sized CMM because the maximum measuring volume of most large-sized CMMs are approximately 10 m^3.

In order to improve the measurement repeatability, other efficient technique is used to determined distance of peak-to-peak of envelope interference fringes rather than using Gaussian best-fit function. Because unsteady and asymmetry of envelope interference fringes destroyed by environmental conditions present imprecise peak detection when analyzed by Gaussian technique. More improvement details are discussed in **Chapter 6**.

5.5 The space diagonal measurements

According to the standard of ISO 10360-2:2009 [9], it lists four required positions for CMMs verification, which shall be the space diagonals of a CMM as shown in **Fig. 1.4**. Therefore, following experimental measurements demonstrate an application of a single-mode fiber optical-comb pulsed interferometer with a ball lens target for the space diagonals of a CMM measurement. A ball lens target is installed on a probing system of a CMM. General probing system of a CMM includes stylus and stylus tip as shown in **Fig. 5.12** [5], which has their own dynamic characteristics during the measuring process. The stylus tip contact with the detected surface is the source of signals that will develop the pattern on the working objects. So, the performance of the CMM overall system is very much dictated by the motion precision of the probe tip and its actuator. Therefore, the probe stylus tip is laterally at the center of the CMM operation and a key element of coordinate measurements. The detection probes branch into two main categories. There are contact (tactile) probes and non-contact probes [66].

In this research, although a contact type probing system of a CMM is used, it acts as a non-contact probes because it does not touch any workpiece during measurement. The stylus tip in **Fig. 5.12** is replaced by a ball lens to proceed as a retroreflector for a single-mode fiber optical-comb pulsed interferometer. The experiments demonstrate the efficiency of the proposed technique comparing with a conventional artifact test method, and the comparison results are discussed.
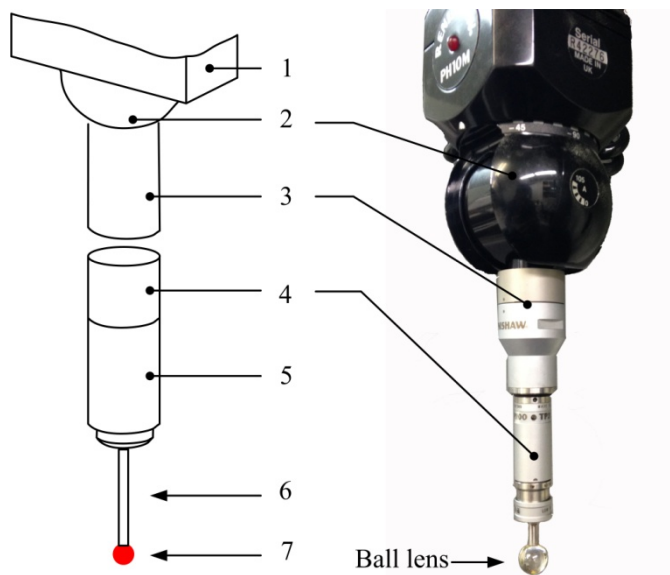
Fig. 5.12 Articulating probing system: (1) Ram, (2) Articulation system, (3) Probe extension, (4) Probe, (5) Stylus extension, (6) Stylus, (7) Stylus tip.

5.5.1 Pulsed interferometer method

The space diagonals of a CMM measurement based on a single-mode fiber optical-comb pulsed interferometer demonstrates in this experiment. The compact-size pulsed interferometer measuring system was setup as a diagram illustrated in **Fig. 5.13**.
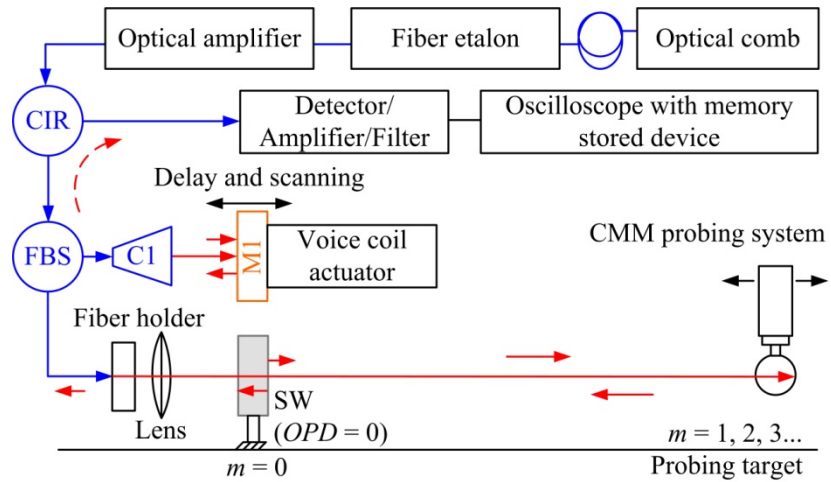
Fig. 5.13 Measurement setup diagram.
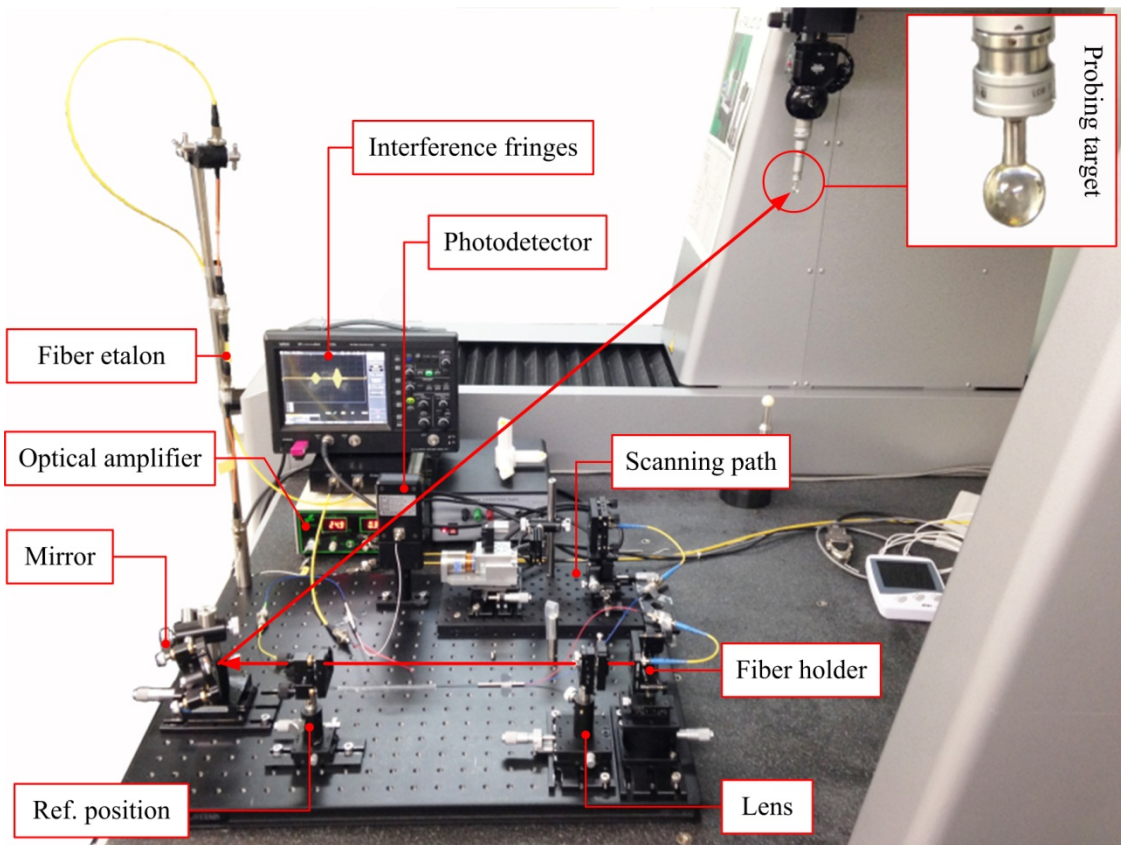
Fig. 5.14 A space diagonal of a CMM measurements using a pulsed interferometer.

The compact size of a single-mode fiber optical-comb pulsed interferometer was connected to an optical comb passing through an optical fiber over 100 m from 10th floor to the basement floor of the building. (An optical comb has been installed at the 10th floor, and a CMM has been installed at the basement of the building). A ball lens target was fixed on a CMM probing system as shown in **Fig.5.12**. Then, diagonals of a moving bridge-type CMM (FALCIO APEX 707, Mitutoyo) were measured by this system. First of all, the measuring volume of a CMM was defined as shown in **Fig. 1.4**, and the measuring lines in diagonal of a CMM were identified. An example of space diagonal of a CMM measurement in a measuring line of $(1, 0, 0 - 0, 1, 1)$ is shown in **Fig. 5.14**, where measuring lines in opposite corners of the measuring volume are assumed to be $(0, 0, 0)$ and $(1, 1, 1)$ in coordinates (X, Y, Z).

To avoid the optical path error due to the difference of refractive indices between air and ball lens target, the initial zero positions both of CMM and interferometer were set when the value of $m \geq 1$, because the optical path error of each position will automatically be compensated by the initial position. The measurements were done by moving a CMM probe head in diagonals of approximately 150 mm, and then absolute lengths were measured. The measurement results of four directions in diagonal are shown in **Fig. 5.15**.
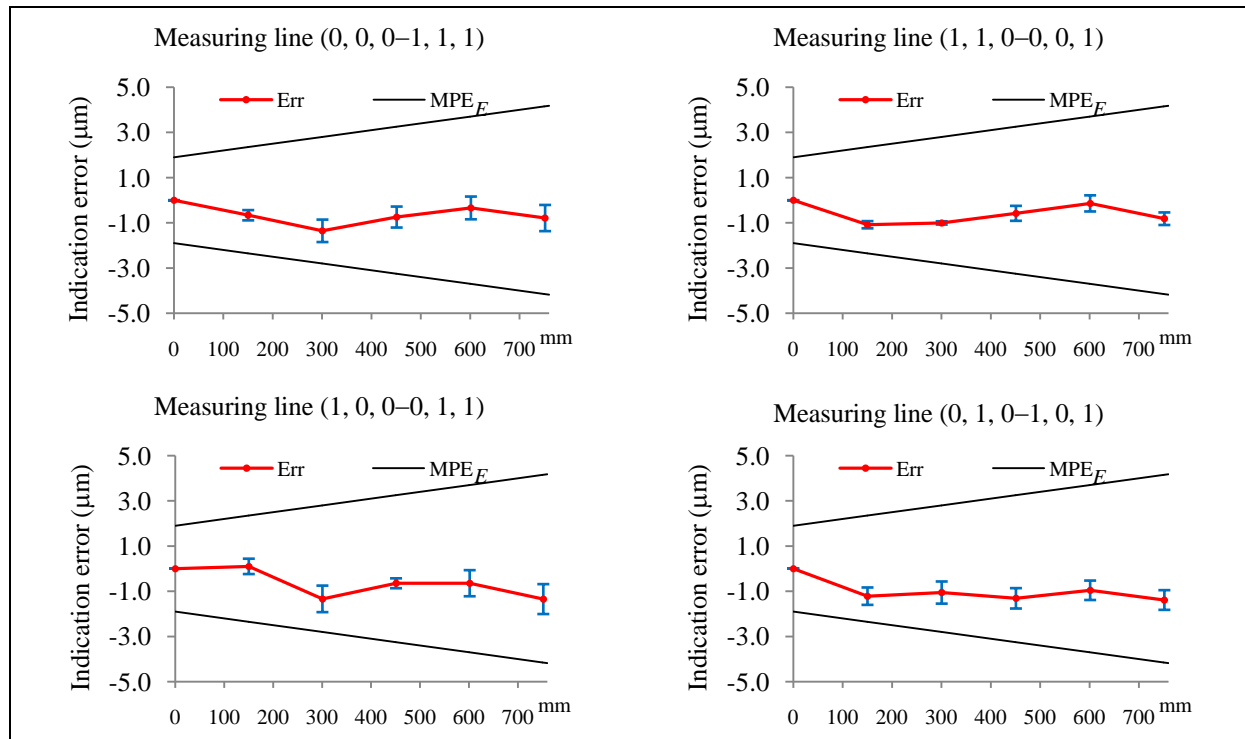
Fig. 5.15 Measurement results for four diagonals in space; measuring lines in opposite corners of the measuring volume are assumed to be $(0, 0, 0)$ and $(1, 1, 1)$ in coordinates (X, Y, Z).

In this experimental measurement, a CMM was operated by the speed condition of 100 mm/s. **Fig. 5.15** shows the errors of each diagonal direction of a CMM with measurement standard deviation bar. Errors in diagonals of CMM are determined by the difference between nominal positions of a CMM and absolute lengths these measured by interferometer. All results are within the maximum permissible error of a CMM for size measurement. The maximum measurement standard deviation is approximately 0.4 µm for five time measurement repetitions. However, the standard deviation consist of the positioning repeatability of a CMM, and positioning errors are evaluated based on non-contact probing system, while the maximum permissible error of a CMM is determined by including probing error of a CMM.

5.5.2 Artifact test method

To confirm the accuracy and efficiency of the proposed method, these measurements were compared with the results of a standard artifact test method. The artifact is a step-gauge (S232, KOBA−step) with a steel frame, 16 ceramic gauges, 32 faces, and 20 mm nominal length as shown in **Fig. 5.16**. The thermal expansion coefficient is ~11.5×10^{-6} K^{-1}. This step gauge was supported, and the reference lengths were measured by the National Metrology Institute of Japan, (NMIJ).
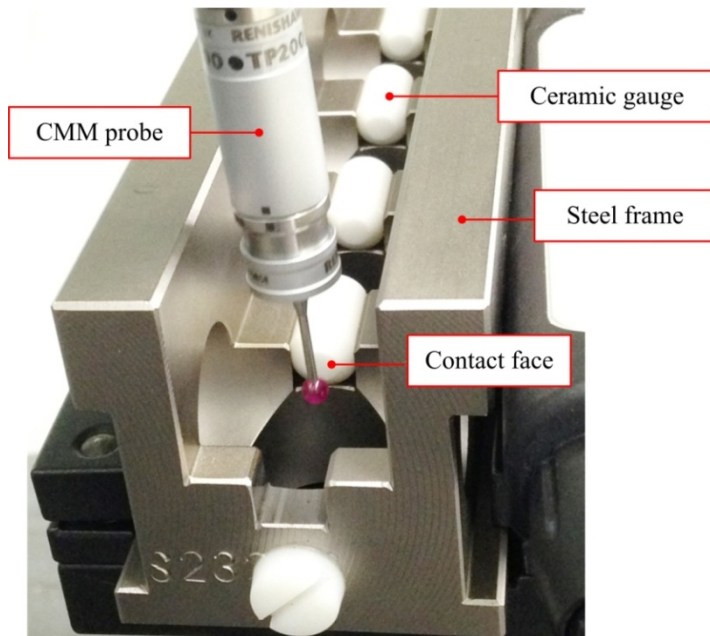
Fig. 5.16 A standard artifact that is used in the measurement comparison: a step gauge (200412 S232, KOBA−step) with 32 contact faces, and 620 mm long, which the standard lengths were measured by NMIJ.

The step gauge was aligned to be close to the measurement lines of a single-mode fiber optical-comb pulsed interferometer method along the four diagonals of the CMM. An accurate temperature sensor was attached on step gauge to observe the gauge temperature during measurements and two temperature sensors were used for expanded length compensations. Each measurement line was measured only after the temperature of the step gauge had remained stable for more than 3 hours. The measurement results were corrected to the reference temperature by CMM software. The measurement setup for four directions are shown in **Fig.5.17 (a)–(d)**.
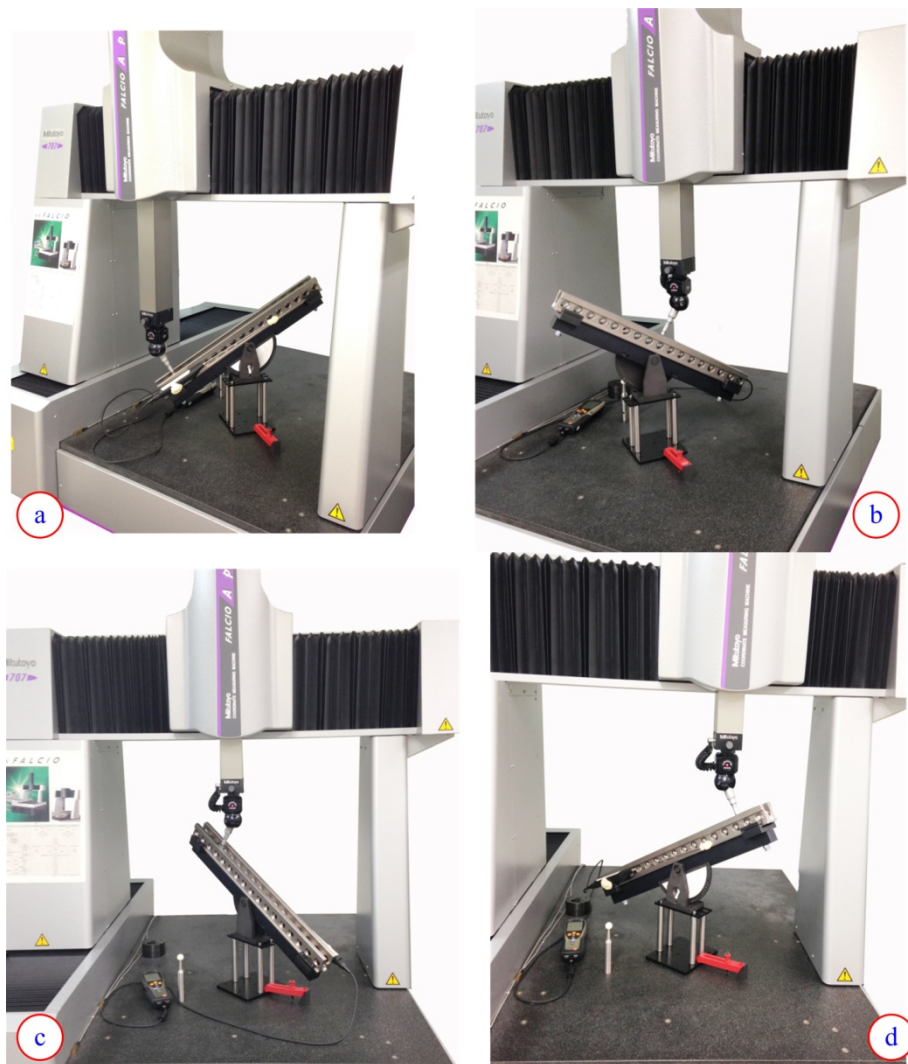
Fig. 5.17 The space diagonals of a CMM measurement based on artifact test method; (a) is the measuring line (0, 0, 0 − 1, 1, 1), (b) is (1, 0, 0 − 0, 1, 1), (c) is (0, 1, 0 − 1, 0, 1), and (d) is (1, 1, 0 − 0, 0, 1), respectively.

The measurement results were corrected due to thermal expansion to the reference temperature. The results after compensation are illustrated in **Fig. 5.18**.
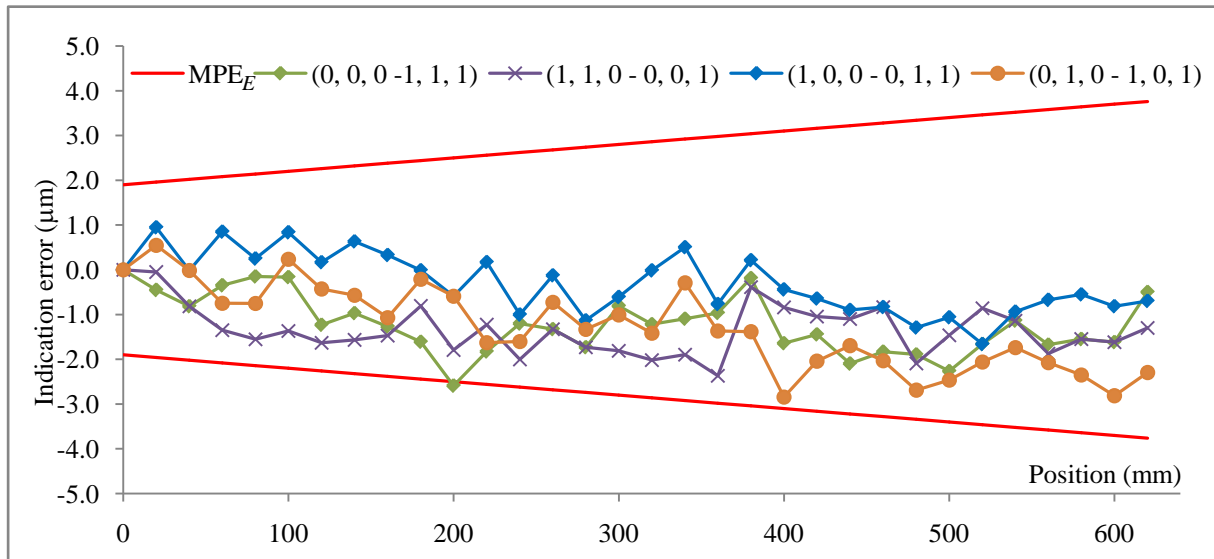
Fig. 5.18 Both indication errors of uni− and bi−directional measurement of a CMM for four diagonals. The number in brackets refer to direction of measurement lines.

The indication errors of each measuring line were determined by the difference of measured values and reference lengths of a step gauge. Most measurement results are within the maximum permissible error of a CMM [$MPE_E = \pm (1.9 + 3l/1000)$ μm, where l is the indication length of a CMM in mm], only a point that out of specification and the maximum standard deviation of measurement is approximately 0.71 μm.

However, using a step gauge is a contact type of the measurement, both unidirectional and bidirectional measurements are used to determine the indication errors of a CMM. Therefore, the measurement results include the probing error of a CMM's probe head. It is very difficult to compare the results between artifact method and the proposed method because a single-mode fiber optical-comb pulsed interferometer technique is a non-contact type of the measurement. In order to make a measurement comparison, only unidirectional measurement results of the step gauge method were considered because the lengths which are evaluated in unidirectional measurements do not need the stylus-tip diameter compensation. It can be eliminated the error due to the compensation [67]. Then the measurement results are able to compare as shown in **Fig. 5.19 (a)−(d)**.
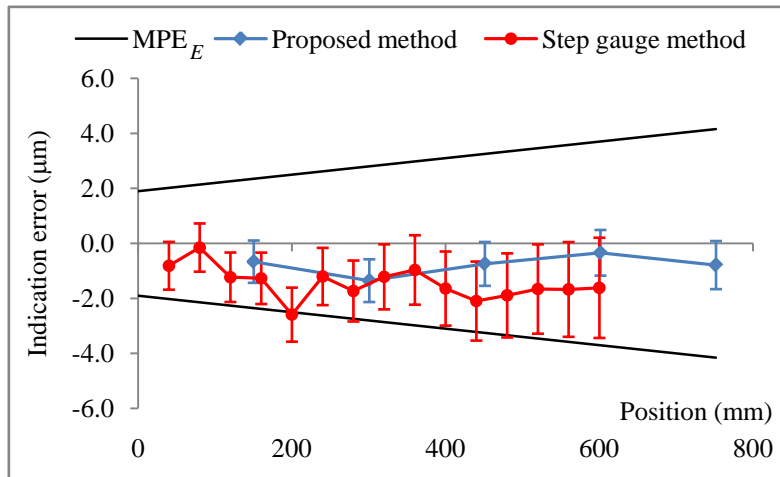
Fig. 5.19 (a) Measurement results of measuring line (0, 0, 0 − 1, 1, 1).
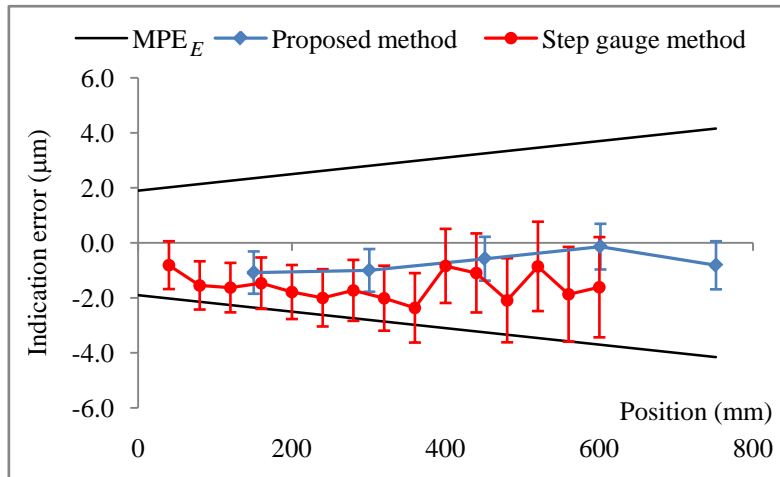
Fig. 5.19 (b) Measurement results of measuring line (1, 1, 0 − 0, 0, 1).
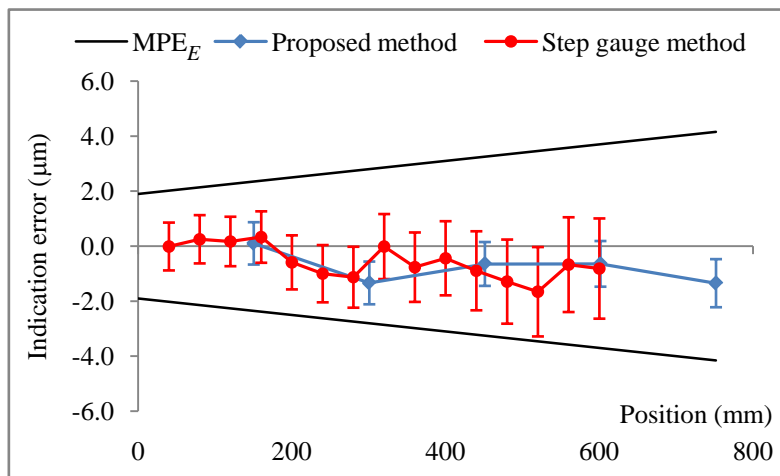
Fig. 5.19 (c) Measurement results of measuring line (1, 0, 0 − 0, 1, 1).

101
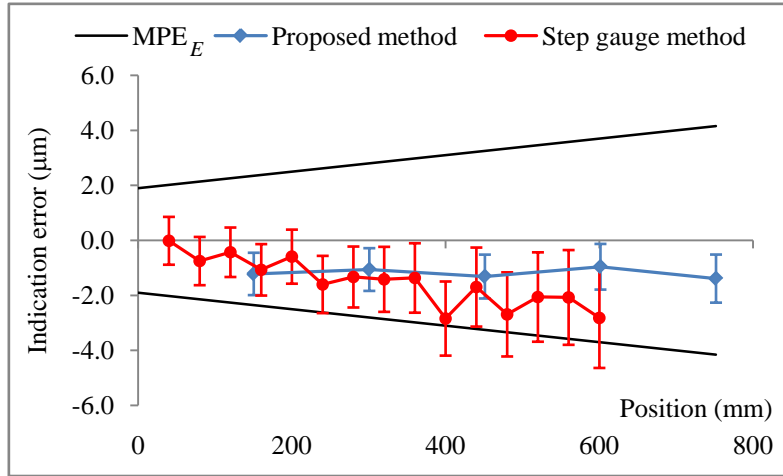
Fig. 5.19 (b) Measurement results of measuring line $(0, 1, 0 - 1, 0, 1)$.

For the measurement comparisons, only unidirectional measurements of a step gauge were considered in order to reduce probing error of a CMM. The results show that all position measurements fall within the maximum permissible error of indication of a CMM for size measurement. The uncertainties of measurements are discussed in the next section. However, the proposed method is a non-contact, and the positioning accuracy along each diagonal was verified approximately every 150 mm. In contrast, the step gauge method is a contact measurement, and each diagonal was verified at approximately every 40 mm, following the nominal length of a step gauge. In addition, although error due to stylus tip compensation was eliminated by taking only unidirectional measurements, probing errors of the CMM still affect measurement repeatability. However, measurement uncertainty of the proposed method was smaller than that of the step gauge due to a slight effect of air temperature. Additionally, temperature distribution on a step gauge significantly affects the measurement uncertainty rather than the proposed method. Moreover, the step gauge method is more time consuming than the proposed method because of the waiting for stabilized temperature. The proposed method can directly verify a CMM after 30 minutes warm up of the measuring system.

In order to establishment of the effectiveness and comparability of testing or measurement methods, evaluation of the performance characteristics of the proposed method and validation of uncertainty claims, a part of general requirements for proficiency testing (ISO 17043:2010) has been applied [68]. General measurement comparisons are often determined by E_n ratio as **Eq. (5.4)**, where $x–X$ is the difference value between the participant's measured result (x) and the assigned value (X). U_{lab} is the expanded uncertainty of a participant's measured result, and U_{ref} is the expanded uncertainty of the reference laboratory's assigned value.

$$E_n = \frac{x - X}{\sqrt{U_{lab}^2 + U_{ref}^2}} \tag{5.4}$$

The $|E_n| > 1.0$ indicates "unsatisfactory". On the other hand, the effectiveness and comparability of testing or measurement methods, the performance characteristics of the proposed method and validation of uncertainty claims are satisfied since $|E_n| \leq 1.0$.

By applying this standard, a CMM under test is considered as an artifact, which is verified by the step gauge method and the proposed method. The step gauge method is a standard test. So, it is considered as the reference measurement method for the comparison. However, the difference values between the proposed results and the conventional reference results are hard for comparing, because the proposed method verifies lengths every 150 mm while step gauge method is every 40 mm. For that reason, only the E_n ratio at the indication length of 600 mm in four space diagonals of a CMM were evaluated as shown in **Table 5.1**.

Table 5.1 Evaluation result of E_n ratios.

Measuring lines	$x–X$ (μm)	$|E_n|$
0, 0, 0 – 1, 1, 1	−1.28	0.60
1, 1, 0 – 0, 0, 1	−1.48	0.69
1, 0, 0 – 0, 1, 1	−0.17	0.08
0, 1, 0 – 1, 0, 1	−1.86	0.87

The E_n ratios in **Table 5.1** indicate that the comparability of the proposed method and validation of uncertainty claims are accepted, when compared with a standard step gauge method. The measurement uncertainties of both methods are evaluated and discussed in the next section.

5.6 Diagonal measurement uncertainties

5.6.1 Using a single-mode fiber optical-comb pulsed interferometer

The uncertainty of measurement is evaluated in accordance with GUM [4, 62–63]. The positioning error of each diagonal of a CMM (E_x), which is measured by a single-mode fiber optical-comb pulsed interferometer, is determined by **Eq 5.5**.

$$E_x = l_x - l_s + \delta l_{ix} + l_N \cdot \alpha \cdot \Delta T \tag{5.5}$$

where, l_x is indication length of a CMM,

l_s is standard length, which determined by the proposed method,

δl_{ix} is correction due to the finite resolution of a CMM,

l_N is the nominal length,

α is the thermal expansion coefficient of linear scale of a CMM,

ΔT is difference in temperature between linear scale of a CMM and reference temperature.

According to mathematical model of the positioning error of a CMM in **Eq. (5.5)**, the uncertainty of CMM diagonal measurement is evaluated by:

$$u^2(E_x) = u^2(l_x) + u^2(l_s) + u^2(\delta l_{ix}) + l_N \cdot \Delta T u^2(\alpha) \tag{5.6}$$

First of all, the standard length (l_s) determined by **Eq. (3.1)** relates to the uncertainties of the repetition frequency, the group refractive index of air, and the distance of peak-to-peak of the envelope interference fringes. The stability of the repetition frequency after passing a fiber etalon is in the order of 10^{-9} over 2 hours [52]. This case is a partial contribution to length uncertainty of $0.5 \times 10^{-9} l$ divided by the rectangular distribution, because of semi-range limits of a finite resolution of the instrument used. The uncertainty of the repetition rate and carrier offset frequency of an optical comb is canceled because the accuracy ratio with the maximum permissible error of a CMM is more than 100 times better.

Secondly, the standard length was compensated the group refractive index of air by Ciddor's equation. Therefore, the uncertainty components depend on the deviation of environmental conditions and accuracy of sensors which were used in the measurement. The compensation equation relates to uncertainties of air pressure, air humidity, air temperature, and the density of CO_2. However, CO_2 is used as a constant of 450 ppm. Therefore, the combined standard uncertainty of corrected length is determined by applying Ciddor's

equation as shown in **Eq. 5.7**.

$$u^2(l_n) = \left(\frac{\partial l_n}{\partial p}\right)^2 u^2(p) + \left(\frac{\partial l_n}{\partial t}\right)^2 u^2(t) + \left(\frac{\partial l_n}{\partial R}\right)^2 u^2(R)$$
(5.7)

The combined standard uncertainty is determined by applying Ciddor's equation which the sensitivity coefficients are evaluated by the first performing the partial derivatives. The contribution uncertainty of each parameter is evaluated by standard uncertainties multiply with their sensitivity coefficients [62, 63]. The uncertainties due to air pressure (p), air temperature (t), and air humidity (R) are evaluated by determining the maximum variations in laboratory during measurement. There are 2.9 %RH, 0.40 °C, and 0.1 kPa, respectively. These parameters are estimated to have rectangular limits, and the uncertainty of Ciddor's equation is estimated in order of 10^{-8}.

Next, uncertainty conversion of time to length scale that used to determine the peak-to-peak distance of envelope interference fringes is evaluated by the measurement of the relationship between time scale and length scale. This is evaluated from the maximum deviation between the measured values and the best-fit line. It is approximately 0.31 μm, which assumed to be a rectangular distribution. The uncertainty components due to measuring method are summarized in **Table 5.2**.

Table 5.2 Uncertainty sources of the proposed measuring method.

Uncertainty sources	Standard uncertainty, $u(x_i)$	Sensitivity coefficient, c_i	Uncertainty contribution, $u(y_i)$
Sources from interferometer			
Repetition frequency stability	$2.89 \times 10^{-10}\ l$	1	$2.89 \times 10^{-10}\ l$
Refractive index of air compensation			
−Ciddor's equation	$< 10^{-8}$	l	$1.00 \times 10^{-8}\ l$
−Air humidity	0.29 %RH	$1.02 \times 10^{-8}\ l/\text{%RH}$	$2.95 \times 10^{-9}\ l$
−Air temperature	0.23°C	$9.15 \times 10^{-7}\ l/°C$	$2.11 \times 10^{-7}\ l$
−Air pressure	57.74 Pa	$2.64 \times 10^{-9}\ l/\text{Pa}$	$1.51 \times 10^{-7}\ l$
Conversion of time to length scale	1.79×10^{-4} mm	1	1.79×10^{-4} mm
Combined uncertainty	0.18 μm + $2.61 \times 10^{-7}\ l$		
Expanded uncertainty (k =2)*	$[(0.36)^2 + (0.52 \times 10^{-3}l)^2]^{1/2}$ μm		

*Note: l is indication length of a CMM expressed in mm.

Following this section is the measurement uncertainty that is caused by CMM under test itself. In this experimental measurement, the difference of temperature between linear scale of a CMM and reference temperature cannot be directly measured, and the length positions of a CMM in each diagonal were automatically compensated of thermal expansion to the reference temperature by CMM's software. Therefore, only an uncertainty of the thermal expansion coefficient (1×10^{-6} $°C^{-1}$) is considered, and assumed to be a rectangular distribution.

Subsequently, the digital scale interval of the linear scale of CMM is 0.001 mm (the resolution in X, Y, and Z axes of a CMM are 0.0001 mm. The resolution of a CMM was rounded of the reading at the digit of 1 μm). Variations due to this finite resolution were estimated to have rectangular limits of 0.5 μm. Next, the measurement was repeated five times, resulting in a maximum standard deviation of approximately 0.40 μm. Consequently, uncertainty due to limited repeatability was estimated to have a normal distribution. The uncertainty components of CMM under test are summarized in **Table 5.3**.

Table 5.3 Uncertainty sources of CMM under test.

Uncertainty sources	Standard uncertainty, $u(x_i)$	Sensitivity coefficient, c_i	Uncertainty contribution, $u(y_i)$
Sources from CMM			
Thermal expansion of linear scale	5.77×10^{-7} $°C^{-1}$	0.4 °C l	2.31×10^{-7} l
Finite resolution	2.89×10^{-4} mm	1	2.89×10^{-4} mm
Measurement repeatability	1.79×10^{-4} mm	1	1.79×10^{-4} mm
Combined uncertainty	0.34 μm + 2.31×10^{-7} l		
Expanded uncertainty (k =2)*	$[(0.68)^2 + (0.46 \times 10^{-3}l)^2]^{1/2}$ **μm**		

*Note: l is indication length of a CMM expressed in mm.

Finally, the total expended uncertainty (k = 2) of a CMM verification in diagonals is calculated to be $[(0.77)^2 + (0.69 \times 10^{-3}l)^2]^{1/2}$ μm, where l is indication length of a CMM expressed in mm.

5.6.2 Uncertainty based on using a step gauge

The indication error of diagonal measurements of a CMM using a step gauge method at the reference temperature (20 °C) is obtained from following relation:

$$E_x = l_x - l_s + \delta l_{ix} + l_N \cdot \overline{\alpha} \cdot \Delta t \tag{5.8}$$

where, l_x is indication length of a CMM,

l_s is standard length of a step gauge,

δl_{ix} is correction due to the finite resolution of a CMM,

l_N is the nominal length of the actual step gauge,

$\overline{\alpha}$ is average thermal expansion coefficient of the step gauge and linear scale of a CMM,

Δt is difference in temperature between the step gauge and linear scale of a CMM.

The measurement uncertainty of positioning error of diagonal measurements using a step gauge is simply to determine by replacing term l_s by the reference length of a step gauge. As a result, the uncertainty components are evaluated by:

$$u^2(E_x) = u^2(l_x) + u^2(l_s) + u^2(\delta l_{ix}) + l_N \left[\overline{\alpha} \cdot u^2(\Delta t) + u^2(\overline{\alpha}) \cdot \Delta t \right] \tag{5.9}$$

The lengths of a step gauge used as the reference length standards, together with its associated expanded uncertainty of measurement, are given in the calibration certificate. This step gauge has been calibrated by National Metrology Institute of Japan, (NMIJ) with CMC (calibration and measurement capability) of $[(170)^2 + (480 \cdot L)^2]^{1/2}$ nm, where L is the length of the step gauge expressed in m.

Before measurements, both CMM and step gauge were leaved in laboratory more than 24 hours. After an adequate stabilization time, the temperature variation on the step gauge is 0.25 °C, while room temperature variation is 0.4 °C, by approximately. The coefficient of thermal expansion of the linear scale of a CMM is approximately 8.0 μm m^{-1}K^{-1} with an uncertainty of ± 1 μm m^{-1}K^{-1}, and a step gauge is approximately 11.5 μm m^{-1}K^{-1} with limits of ± 1 μm m^{-1}K^{-1}. In this measurement, the changes of temperature on linear scale of a CMM cannot be directly measured. However, the thermal expansion was automatically compensated to the reference temperature by CMM's software. In addition, two accurate sensors were used to measure temperature on a step gauge for expanded length compensations. Therefore, only

temperature variation on a step gauge is mainly significant to uncertainty of standard lengths, which is assumed to have rectangular distribution. The uncertainty due to limits of thermal expansion coefficient of a step gauge is estimated by multiply with the temperature variation on a step gauge.

The measurement is repeated five times with the maximum standard deviation approximately 0.71 μm. This mainly cause by the probing head of a CMM. Thus, uncertainty due to limited repeatability is estimated to have normal distribution. The uncertainties involved with a CMM are the same as explained in previous section. The uncertainty of measurement associated with the result is clearly dominated by the combined effect of the repeatability due to probe head of a CMM and the finite resolution of the CMM. The expanded uncertainty is evaluated to be $[0.87^2 + (2.91 \times 10^{-3} \times l)^2]^{1/2}$ μm, where l is indication length of a CMM in mm, and measurement uncertainty of diagonal measurements of a CMM using a step gauge is summarized in **Table 5.4**.

Table 5.4 Uncertainty sources of diagonal measurements using a step gauge method.

Uncertainty sources	Standard uncertainty, $u(x_i)$	Sensitivity coefficient, c_i	Uncertainty contribution, $u(y_i)$
Sources from standard step gauge			
Certificated calibration of length	0.085 μm + $2.40 \times 10^{-7} l$	1	0.085 μm + $2.40 \times 10^{-7} l$
Temperature variation on gauge	0.14 °C	$9.75 \times 10^{-6} l$ °C^{-1}	$1.14 \times 10^{-6} l$
Thermal expansion of step gauge	5.77×10^{-7} °C^{-1}	0.25 °C l	$1.44 \times 10^{-7} l$
Sources from CMM			
Thermal expansion of linear scale	5.77×10^{-7} °C^{-1}	0.4 °C l	$2.31 \times 10^{-7} l$
Finite resolution	2.89×10^{-4} mm	1	2.89×10^{-4} mm
Measurement repeatability	3.18×10^{-4} mm	1	3.18×10^{-4} mm
Combined uncertainty	0.44 μm + $1.45 \times 10^{-6} l$		
Expanded uncertainty (k =2)*	$[(0.87)^2 + (2.91 \times 10^{-3} l)^2]^{1/2}$ μm		

*Note: l is indication length of a CMM expressed in mm.

5.7 Chapter conclusion

The ball lens with refractive index of 2 can be used as the target of the single-mode fiber optical-comb pulsed interferometer. The measuring system can be applied to measure absolute lengths in all directions of the measurement setup. The total accuracy of the ball lens target depends on the accuracies of both the refractive index of glass material and the spherical fabrication. For one-dimensional length measurements, the sphericity of the ball lens does not affect the optical path difference, but it significantly affects three-dimensional lengths measurements. Thus, the error due to the target can be ignored for CMM diagonal measurements by the proposed method.

The reflected-beam intensity from the target is rapidly decreased, when the beam located far from the center of the target more than 0.15 mm. The best zone for achieving interference fringe is that the reflected-beam power form the target should be sufficiently higher than 70% or around ± 0.3 mm. If laser beam is misalignment of 0.3 mm, it may be caused of the cosine error less than 50 nm. Using a ball lens target, absolute length can be performed up to 10 m, cover the range of CMM applications from a medium-sized to a large-sized CMM, because the maximum measuring volume of most large-sized CMMs are approximately 10 m^3.

A new optical measurement method to verify CMMs was proposed. It is a single-mode fiber optical-comb pulsed interferometer, which performed as a non-contact measurement on a ball lens target with refractive index of 2. In practice, the initial zero positions of both CMM and a single-mode fiber optical-comb pulsed interferometer are set when the order of interference fringe is ($m \geq 1$). As a result, the difference indices between the reference plate and the ball lens target are automatically compensated by initial zero position. In addition, the constructive interference fringe is based on a temporal coherence length of the optical frequency comb and the fiber beam splitter is a non-polarization type. Therefore, the changes of phase and polarization due to a ball lens target and a reference plate are not affecting to the measurement. The proposed method is directly traced to the SI base unit.

If the uncertainties of CMM under test are ignored because of dependent upon machines, the measurement capability can be achieved an accuracy of approximately $[(0.36)^2 + (0.52 \times 10^{-3}l)^2]^{1/2}$ μm, which the coverage factor k is 2, or approximately 5.2 μm for the indication length of 10 m. The experimental results show that the measurement accuracy depends on noise in the interference fringe caused by airflow fluctuations and mechanical vibrations. However, measurement uncertainty is smaller than that of the artifact test method due to less effects of air temperature. In addition, the measurement time of the proposed method is 60% less than that of the artifact-test method because of its shorter start-up time; the proposed method can be used in measurements after 30 minutes system warm-up, while the artifact

method requires a waiting period of more than 3 hours to achieve a stabilized gauge temperature for each alignment. Moreover, the alignment procedure is easier in the proposed system because of the compact and convenient optical components. However, the proposed method is a non-contact one, and therefore its CMM verification does not include effects of the CMM probing system. **Table 5.5** is summarized the advantage of the proposed measuring system comparing with a step gauge method.

Table 5.5 Advantages of the proposed system comparing with a step gauge method.

Parameter/ method	Proposed method	Step gauge method
Measurand	Lengths	Lengths
Measurement type	Non-contact	Contact
Range	Up to 10 m	~1.5 m (limited by length of gauge)
Time consumption	< 30 min. / measuring line	> 3 h / measuring line
Temperature effect	Less	More
Measurement uncertainty	Small (~5.2 μm)*	Large (due to temperature effect)
Alignment procedure	Easy	Difficult

*Note: uncertainty is estimated for the indication length of 10 m under specified measurement conditions, and uncertainties due to CMM under test are not included.

For the uncertainty of the proposed measuring system, mainly cause by repeatability of envelope interference fringes, and the conversion of time to length scale. In order to improve the measurement uncertainty, other efficient technique is used to determine peak-to-peak distance of envelope interference fringes, because unsteady and asymmetry of envelope interference fringes are easier destroyed by environmental conditions. These provide imprecise peak detection, when analyzed by Gaussian technique. More accuracy improvements are discussed in the next chapter.

Chapter 6 Measurement accuracy improvement for applications

6.1 Introduction

The first absolute-length measuring machine, (machine prototype) has been established, and automatic measurement software was developed. The measuring system was improved with a high accuracy of measurement. It is lightweight and easy to apply for CMM verification and also any absolute-length measurement in dimensional metrology, which are performed as a non-contact measurement.

This chapter explains about machine design of an absolute-length measuring machine for the convenience in real applications. The machine prototype consists of two optical boxes, which are separated. There are a scanning box and a measuring box. Both optical boxes are connected together through a single-mode optical fiber. Due to separated design, a measuring part can be placed for measurement around the working area, while a scanning part can be fixed as a stationary that make the measurement system easily for real applications. In addition, the automatic measurement software was developed based on LabVIEW programming platform, which the absolute length under measurement is directly reported on the computer screen. Step by step procedure of machine design and automatic measurement software is explained. Moreover, the basic performances of the absolute-length measuring machine prototype such as repeatability, accuracy, resolution, and measurement stability have been evaluated and discussed.

6.2 The design of a compact absolute-length measuring system

The absolute-length measuring machine prototype or called machine prototype, the system diagram is shown in **Fig. 6.1**, consists of two optical boxes, which are separated. The first box (a) is the scanning box, and other (b) is called the measuring box. Both optical boxes are connected together through a single-mode optical fiber. Because of the separated design between a scanning box and a measuring box, the measuring system is easily for setup and conveniently for applications. The measuring box can be placed for setup around the working area, while a scanning box can be fixed as a stationary.
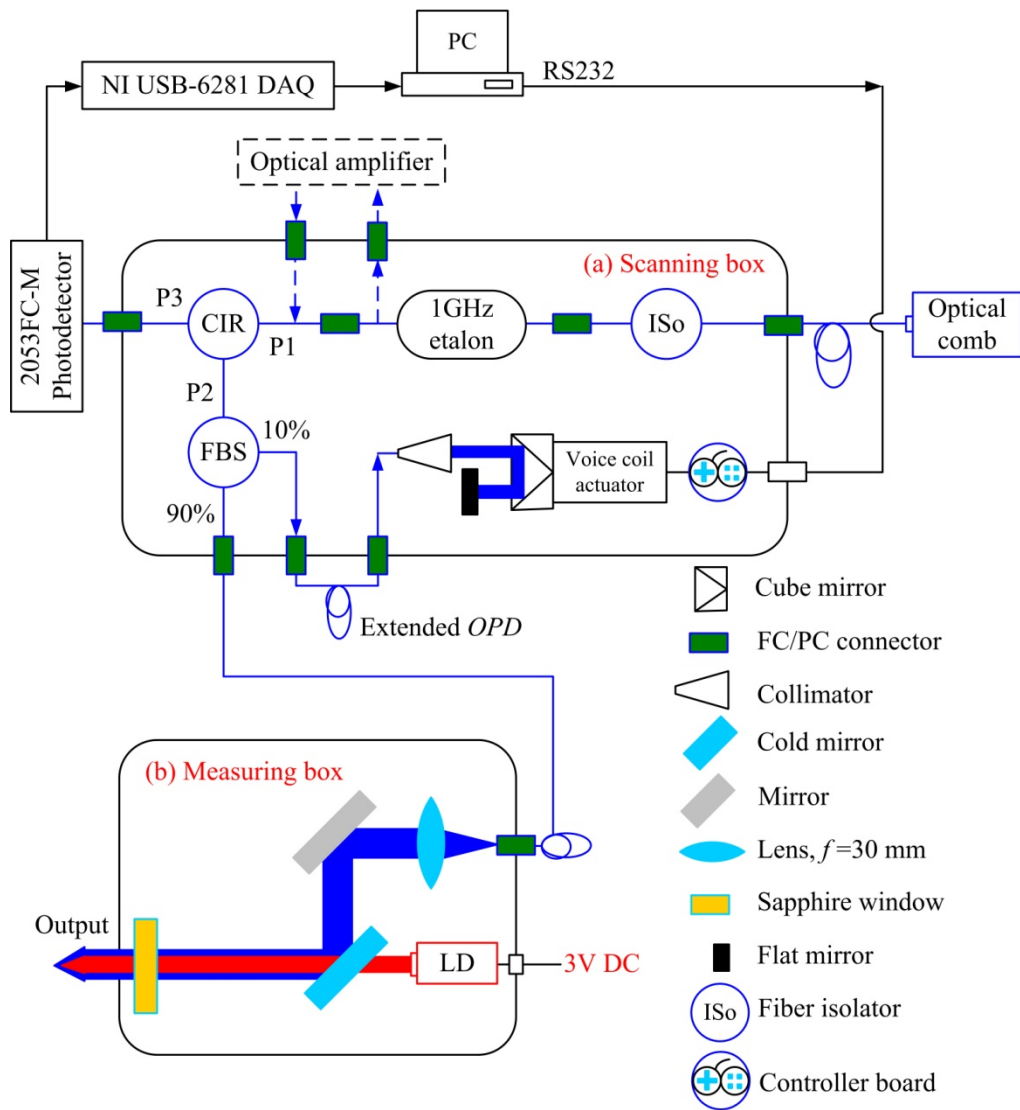
Fig. 6.1 System diagram of the first absolute-length measuring machine prototype.

From measuring system diagram in **Fig. 6.1**, an optical amplifier is an option, which is installed outside the scanning box. For the long-range of measurement, the optical amplifier is required, because the laser power is reduced by a fiber etalon. The hardware configurations outside both boxes are explained in deep details in **Section 6.3**. Overview of the first absolute-length measuring machine prototype is shown in **Fig. 6.2**.
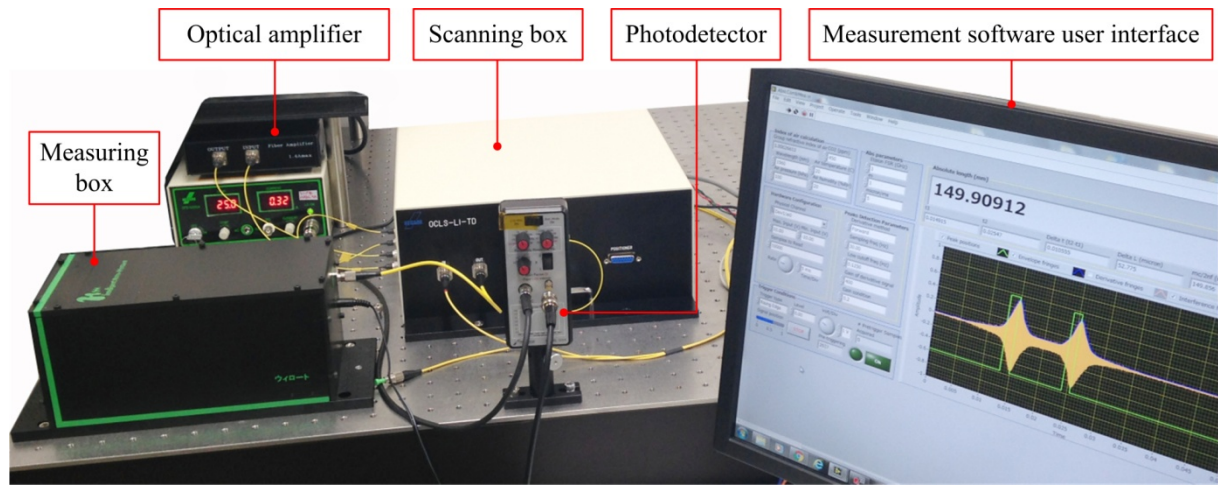
Fig. 6.2 The first absolute-length measuring machine prototype.

6.2.1 Scanning path

The scanning path, or called the scanning box is used to extend optical path length, and to delay optical path difference for matching conditions of generating interference fringes. It consists of a fiber isolator (ISo), a fiber etalon (1−GHz FSR), a fiber circulator (CIR), a fiber beam splitter (FBS), a collimator, a small cube mirror, a small flat mirror, and a voice coil actuator. The ISo is used to protect reflected light back to an optical comb light source. A fiber etalon is connected between the ISo and port-1, (P1) of the CIR. A fiber etalon can be changed to any FSR (default is 1−GHz FSR), corresponding to the absolute length being measured. Port 2, (P2) of the CIR is connected to the FBS, while port-3, (P3) is used as an output port; connect to a photodetector which is installed outside a scanning box. The optical-comb light after passing the CIR is split 90% by the FBS to the measuring box, while 10% is collimated by a collimator to a small cube mirror, which is installed on a voice coil actuator. The scanning speed and scanning direction of a voice coil actuator is controlled by a personal computer through a controller board via a standard for serial communication transmission of data (RS232). The whole components these described above are shown in **Fig. 6.3**. A small flat mirror is installed and adjusted perpendicular to the laser beam. By this optical configuration, the motion errors of a voice coil actuator can be reduced, because the reflected

beam is always returned to the same path with incident beam. As a result, almost interference fringes are symmetry between both sides of their peak positions, and provide a precision of peak position detection.
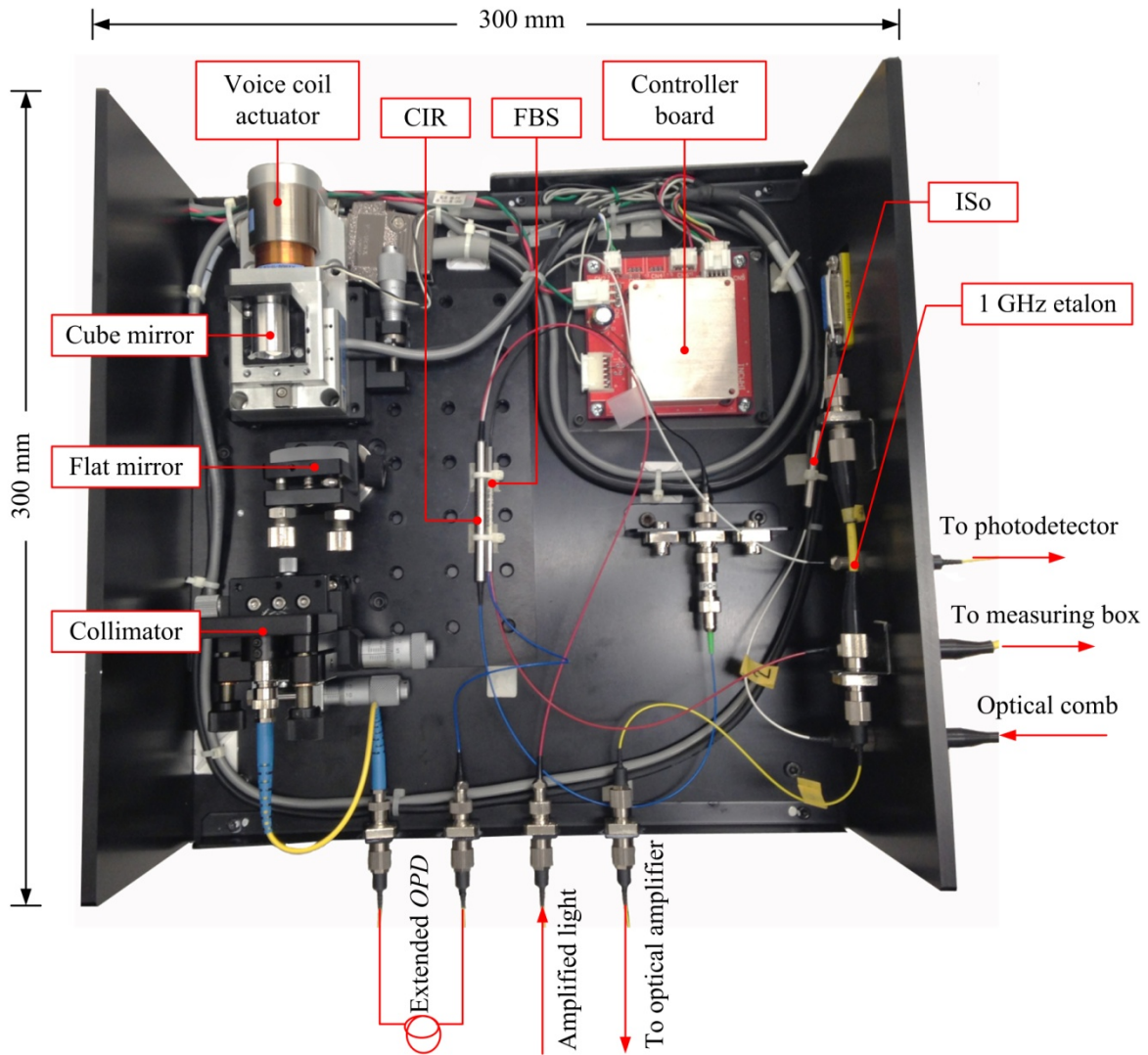
Fig. 6.3 Components inside the scanning box.

6.2.2 Measuring path

The measuring path, or called measuring box is a small box which the optical components inside the box are used as small as possible. By this design, the measuring system is very lightweight, and is easy for applications. The measuring box composes a lens, a flat mirror, a cold mirror, a sapphire window plate, a collimator, and a small laser diode (LD). Components of this part are shown in **Fig. 6.4 (a)**.
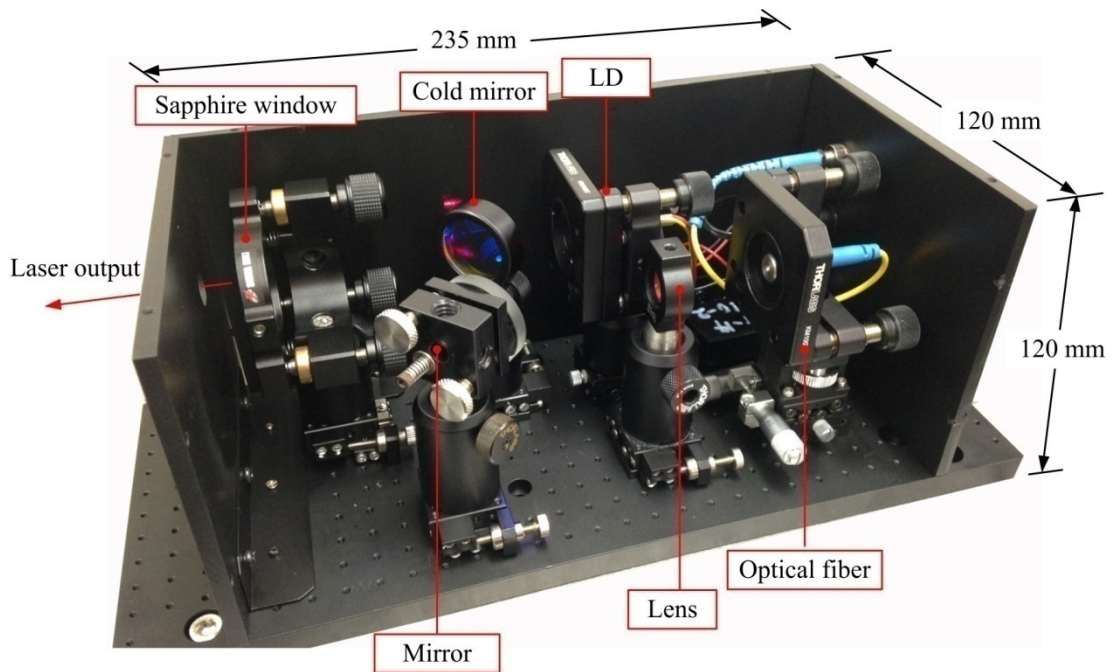
(a) Components inside the measuring box.
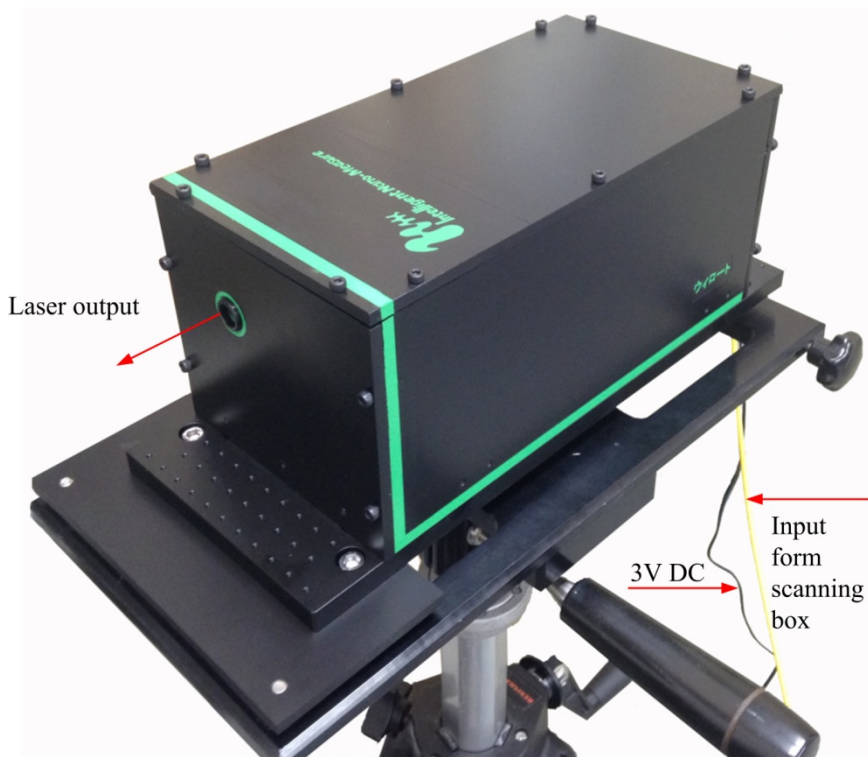
(b) The measuring box on a supporting stand.

Fig. 6.4 The measuring box: (a) shows components inside the box, and (b) the measuring box on a supporting stand.

For the measuring box, a bi-convex lens; a focal length of 30 mm is used to collimate the laser beam from FC-connector that is transmitted by a part of the scanning box. The collimated beam is reflected by a flat mirror and a cold mirror before passing through a sapphire window plate at the reference position to the target outside the box. The sapphire mirror is a reference position, which the *OPD* of the zero-fringe order ($m = 0$) is equally with optical path length of a scanning box. Optionally, a laser diode is installed next to the lens; the red-light beam is collimated by a collimator, transmit passing a cold mirror. The laser diode beam is coaxially aligned with an optical frequency comb light along the measuring line for alignment purposes. By the combination of an optical frequency comb light and a laser diode, the alignment process is easily during applications because the LD is a visible light, which is driven by any power supply of 3 V DC.

Additionally, the measuring box is designed for installation on a supporting stand. The adjustable supporting stand allows laser beam position is simply aligned. This part is needed for laser beam alignment in some applications. Moreover, a several meters of a single-mode optical fiber are used to connect a scanning box and a measuring box via FC connector. In practices, a fiber length that used to connect both boxes should be matched with the length of a fiber that is used for extended the *OPD*.

6.3 Automatic absolute-length measurement

Previous experimental measurements, the absolute lengths are evaluated offline because the peak-to-peak distance of envelope interference fringes, ΔL are determined after transferring data information from a memory stored device of an oscilloscope. This process is not convenient for real applications. Thus, following sections explain about software development for automatic absolute-length measuring system. The software is flexible and convenient coupled usage with the machine prototype.

6.3.1 Hardware configuration

According to diagram in **Fig. 6.1**, two embedded hardware are used in this system; the high-accuracy M-series multifunction data acquisition for Universal Serial Bus (NI USB-6281 DAQ) and the voice coil actuator controller board. The DAQ is connected to a personal computer via USB devices communication, while the controller board of a voice coil actuator passes the RS232 port. The scanning speed and direction of a scanning device are controlled by the controller board. The photodetector (Newport 2053FC-M) is connected to an analog input channel of the DAQ. This channel is used to achieve interference fringes signal. **Table 6.1** shows specification of the DAQ.

Table 6.1 Specifications of NI USB-6281 DAQ.

Channels	16 AI, 2 AO, 24 DIO
ADC resolution	18 bits
Sampling rate	Max. 500 kS/s
Timing accuracy	50 ppm of sampling rate
Input range	Max. ±10 V
Data transfer	USB signal stream, programmed I/O

*For more details refer to manufacturing device specifications.

6.3.2 Absolute-length measurement software

The absolute-length measurements are evaluated by computer software, and the evaluating process follows the flowchart diagram as shown in **Fig. 6.5**. The measurement software begins with the configuration of hardware I/O (Input / Output ports of the DAQ). Then, scanning direction of interference fringes is selected. Normally, a scanning device is operated to run both forward and backward directions. In order to eliminate hysteresis error of a scanning device during measurement, only one direction of a stage motion is selected for archiving interference fringes, either forward or backward direction. Subsequently, analog

118

interference fringes signal from photodetector is always transferred to the DAQ. Thus, the signal conditions and pre-triggering functions are required to achieve only interested signal. (User interface panel and programming codes can be found in **Appendix, Fig**. **A3–A11**.)
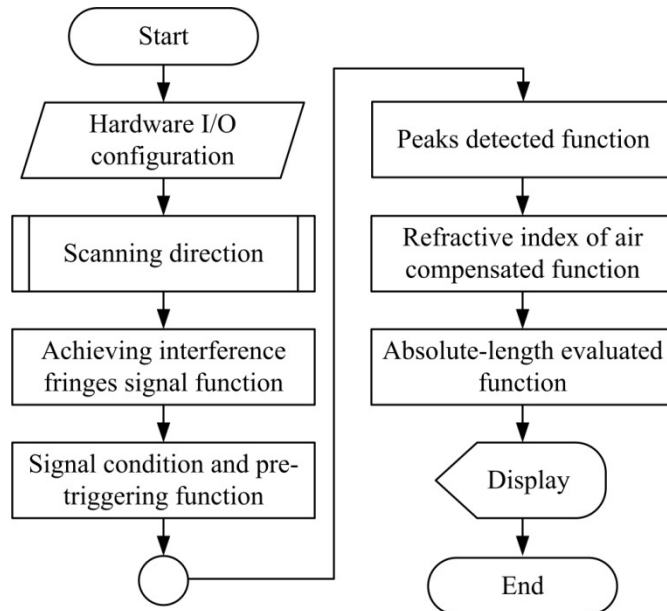
Fig. 6.5 Flowchart of absolute-length measurement software.

The DAQ has analog to digital converter (A/D) to convert analog signal from photodetector to digital signal. In this case, the interference fringes after detected by a photodetector are converted to digital signal and they are not presented between zero amplitude of the screen as shown in **Fig. 6.6**. The signal amplitude will swing somewhere on the screen depending to detected signal voltage from a photodetector, called DC-mode interference fringe signal.
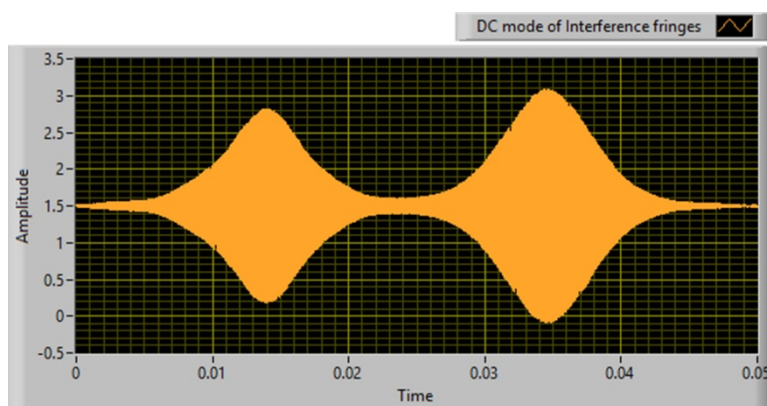
Fig. 6.6 DC-mode of interference fringes signal.

119

The DC-mode interference fringe signal must be adjusted, which positive and negative fringes are hung between zero amplitude by remaining all of signal information before peaks detection processes. This signal is called AC-mode interference fringes as shown in **Fig. 6.7**.
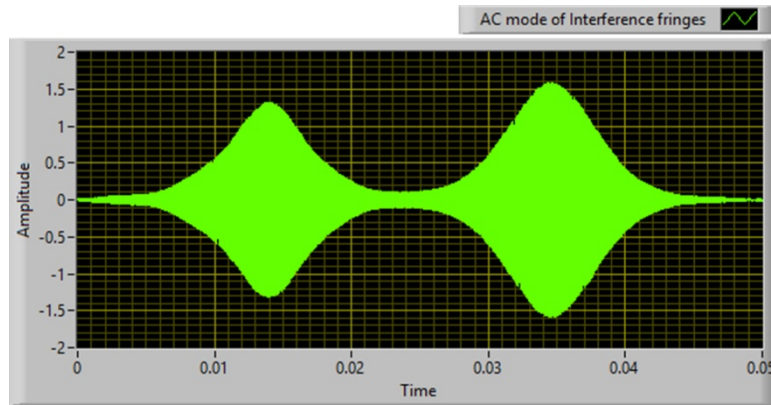
Fig. 6.7 AC-mode of interference fringes signal.

For pre-triggering acquisition via DAQ, the hardware starts acquiring data before the trigger signal is received. In practice, the hardware initiates data acquisition with a software function and stores the data in a circular buffer in the computer memory. The buffer is large enough to ensure that the required numbers of pre-trigger samples are stored. When the buffer is full, it simply wraps around and stores each subsequent sample over the oldest sample in memory. The primary responsibility of the trigger mechanism is to stop the acquisition so that the interested samples in memory represent the "slice-in-time" [69].

Trigger conditions for any application are specified in the configuration section by calling the functions or VIs in LabVIEW. The triggering edge and zero level are default of this software triggering, and then the signal input task will begin as soon as a rising edge occurs on the specified digital line above zero level. By software triggering, the reference interference fringe is always presented as the same position between zero amplitude on the screen of a computer.

6.3.3 Envelope-peak position detection

The precise envelope peak detection is significant to the repeatability and accuracy of absolute-length measurement because ΔL is determined by peak-to-peak distance of envelope interference fringes. According to envelope interference fringe analysis as mention in **Section 3.2.2**, these fringes are fitted by a Gaussian distribution, and then evaluate the envelope peaks positions. The poor accuracy of peak positions detection will be presented if the interference

fringes both side of the peak are asymmetry. This situation can be caused by the effect of environmental conditions and imperfect optical alignment. The peak positions of interference fringe will be shifted by Gaussian fitted curve function as illustrated in **Fig.6.8**.
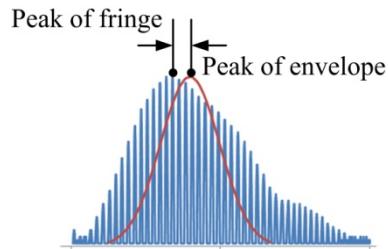
Fig. 6.8 Shifting of peak position due to Gaussian fitted curve function is caused by asymmetry interference fringe between both sides of the peak position.

General an electronics circuit can be used for peak detections [70]. However, it is a complex circuit. In contrast, a simply computer software can be applied for peak detection. It is easier and convenient than electronic circuit. Step by step processing of peak position detection using the computer software is illustrated in **Fig. 6.9**.
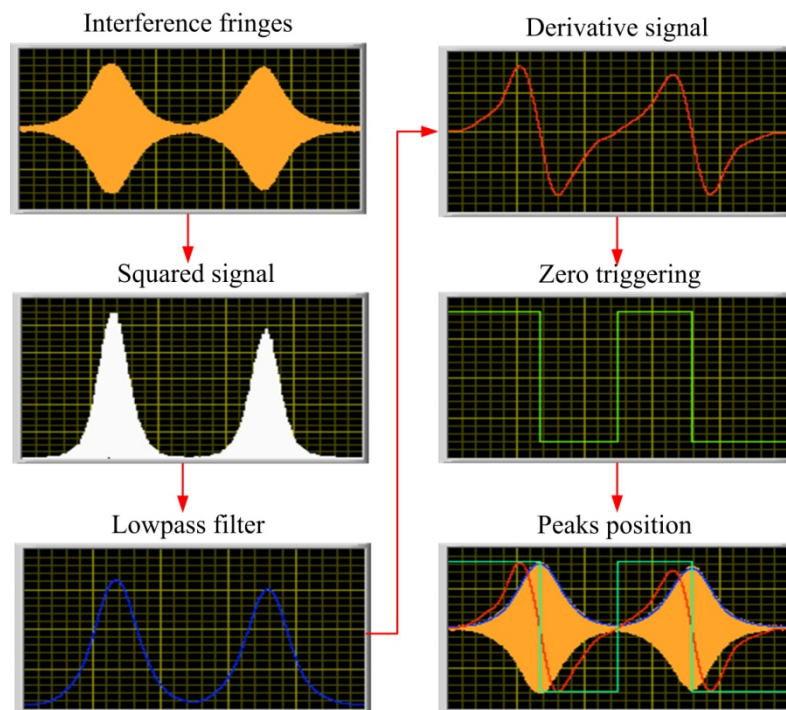
Fig. 6.9 Peak position detection processing

For peak position detection, after pre-triggering and signal condition, the interference fringes signal is squared, and the output signal is passed through a lowpass filter function to get the envelope signal. Subsequently, the envelope signal is differentiated by a derivative function. The peak positions are intersected the zero amplitude by this function. Lastly, the square pulse signal is generated at the zero-crossing position to trig the peaks positions. In case of asymmetry interference fringes, peak detections by this function is precisely and accurately to determine peak positions than using Gaussian best-fit technique, because it always track and trig only the peak position of the envelope signal. In addition, the trigger parameters can be adjusted by users for selecting the best matching condition of peak detection through user interface window as described in the next section.

6.3.4 User interface

The automatic absolute-length measurement software has been developed, and it is easy to use via a graphical user interface. It consists of six windows for controlling and monitoring interference fringes. The first window is use to configure the DAQ and the envelope-peak detection conditions as shown in **Fig. 6.10.**
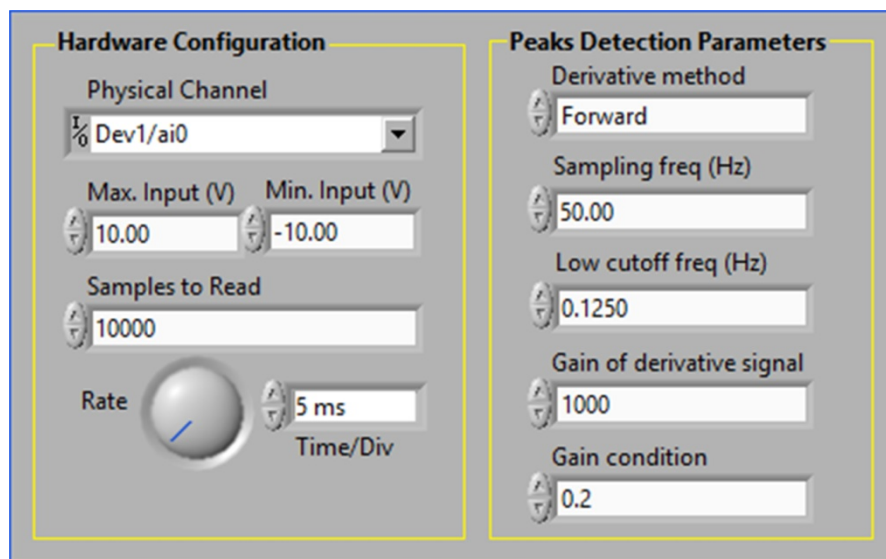
Fig. 6.10 Configurations of DAQ and the envelope-peaks detection conditions.

For hardware configuration window, the physical channel means the channel that the input signal from photodetector is connected to the DAQ. The maximum and minimum voltage input are limited not over $\pm$ 10 V. The sample to read is the number of data (A/D) that achieves from photodetector by DAQ. It is set of 10000 samples. Rate specifies the sampling

rate in samples per channel per second. Next to the hardware configuration window called peak detection parameters, is used to adjust the differentiated signal conditions of peak detection method such as derivative method, sampling frequency and low-cutoff frequency of a lowpass filter function. The gain conditions are use to re-scale of derivative signal to match with display window on the computer screen.
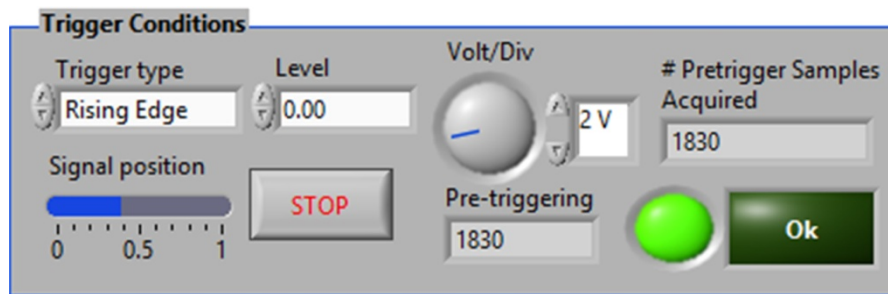
Fig. 6.11 Trigger conditions window.

The second widow is the trigger conditions and it is used for controlling the triggering conditions. In addition, users can select trigger type and voltage level of triggering, and adjust graph scale of interference fringe by adjusting a knob. The defaults are raising-edge trigger, zero-voltage level, and time/div is 2 V as illustrated in **Fig. 6.11**.

Next windows are the index of air calculation and absolute-length (Abs) parameters as shown in **Fig. 6.12**. The group refractive index of air is determined by Ciddor's equation as described in **Section 2.8**. Group refractive index of air will automatically re-calculated, when any parameters inside text boxes are changed such as CO_2, laser wavelength, air temperature, air pressure, and air humidity.
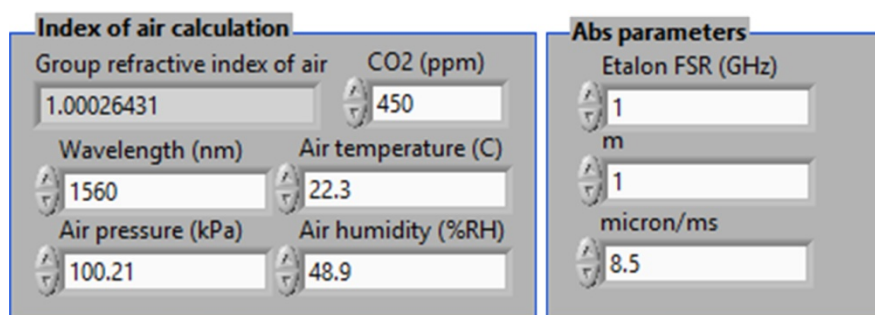
Fig. 6.12 Index of air calculation and absolute-length parameter windows.

For window of the Abs parameters, users can modify absolute-length parameters, which relates to measurement conditions such as a free spectral range of a fiber etalon, order of

interference fringe (*m*), and the relationship of time to length scale conversion as explained in **Section 3.4.1**.

Next, the screen graph display is used for interference fringes observation. Result is shown in **Fig. 6.13**, when the peak detection matches with a good condition. The interference fringes (yellow line), envelope interference fringes (blue line), differentiate signal (red line), and peak detected signal (green line) are presented.
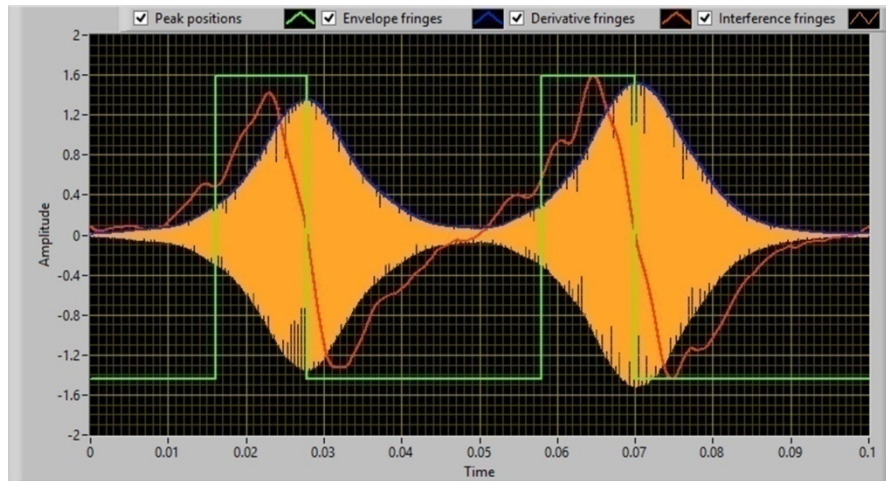
Fig. 6.13 Interference fringes and envelope peak detection window.

The last window is the display length of absolute length under measurement, expressed in mm as shown in **Fig. 6.14**. This is the measuring length that is determined by **Eq. 3.1**. When this value occurs, it means that parameter conditions match with all above discussions.
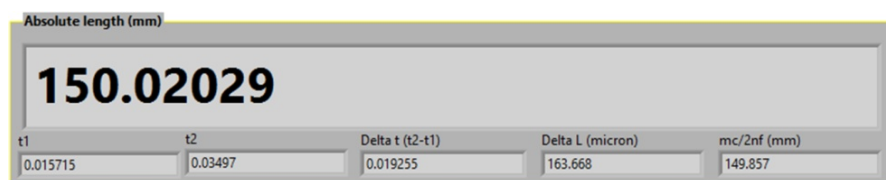
Fig. 6.14 Display window of absolute length under measurement.

The complete panel of a user interface and programming codes are illustrated in **Appendix**. It is the combination of six windows which are described above. All programming functions are run together by very fast step flowing programming flowchart in **Fig. 6.5**.

6.4 Basic performances of the machine prototype

The basic performances of the machine prototype coupling with the automatic absolute-length measurement software have been performed such as measurement repeatability, resolution, accuracy and stability of the measurement. Because of a new system design, the relationship of time to length scale conversion must be re-measured again. The measurement procedure is the same as explained in **Section 3.4.1**, and **Fig. 6.15** shows photograph of the experimental measurement.
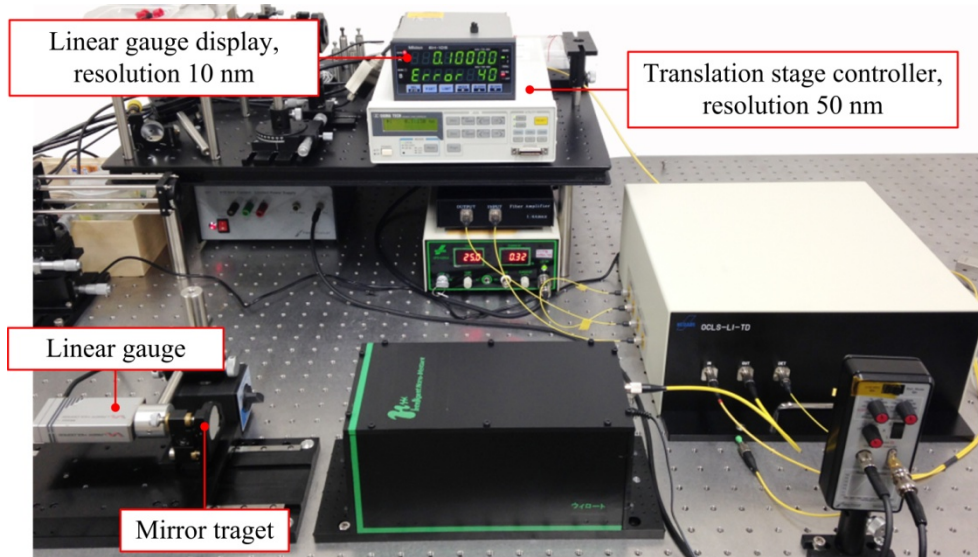
Fig. 6.15 Time to length scale measurement.
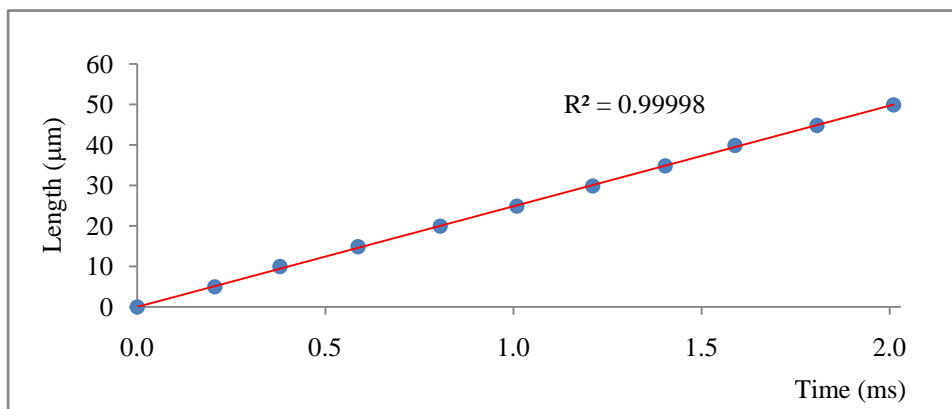
Fig. 6.16 Time to length scale measurement results.

125

The measurement was performed when two interference fringes were completely separated with each other, because this condition provided a small measurement standard deviation as discussed in **Section 3.2.2**. Each length accurately measured by steps of 5 µm up to 50 µm, and was controlled by a precise translation stage controller. The scanning device inside a scanning box was operated by a constant speed of 0.002 m/s.

The average measurement result of three times repetitions and the best-fit line (red line) is shown in Fig. **6.16**. This result shows that relation of time to length scale is linear. Here, the conversion factor of 1 ms corresponds to the length of approximately 23.979 µm. The maximum deviation of length scale to the best-fit line is approximately 0.23 µm, and the maximum of measurement standard deviation is approximately 5.13 µs, or relates to a length of approximately 0.12 µm.

6.4.1 Resolution of machine prototype

Resolution of measurement is the fineness to which an instrument can be observed. In this measuring system, the resolution of machine prototype involves how well the responding time of interference fringes can be achieved. Therefore, it depends on analog to digital converter and sampling clock of a data acquisition device. The specification of DAQ with A/D resolution of 18 bits, and the maximum sampling rate of 500 kS/s with a timing accuracy of 50 ppm of sampling rate as list in **Table 6.1**, is sufficient for archiving sub-micron resolution. However, the resolution also depends on configuration of the DAQ throughout running the measurement process.

Table 6.2 Resolution of machine prototype and assigned sampling clock.

Sampling clock	Adjacent data point	Full scale	Resolution
ms	ms	ms	µm
0.5	0.0005	5	0.01
1	0.001	10	0.02
2	0.002	20	0.05
5	0.005	50	0.12
10	0.01	100	0.24

With automatic measurement software, 10000 sample points of interference fringes signal are recorded per one time of the scanning in a computer buffer before analysis. The interference fringes always display on a computer screen with 10000 sample points in 10 columns of time scale as shown in **Fig.6.13**. Therefore, the resolution relates to two adjacent data points in time domain, and it depends on sampling clock which is assigned by users.

Because of 1 ms corresponds to a length of approximately 23.979 μm, resolution of machine prototype to sampling clock can be determined and shown in **Table 6.2**. Therefore, the machine prototype is able to achieve the measurement resolution of 10 nm if the sampling clock assigned to 0.5 ms.

6.4.2 Stability of machine prototype

The stability evaluation of a measuring system is not easy, because it depends on interested factor to be evaluated, and at the same time unexpected parameters always affect the measurement. In practices, unexpected parameters are frequently controlled which interested factor can be measured. In addition, the evaluation of a long-term stability requires many measured data for a long period of measurement.

According to above discussion, measuring system stability of the machine prototype has been studied as a short-term drift. The machine prototype is a single-mode fiber optical-comb pulsed interferometer which the group refractive index of air is calculated and compensated. Therefore, the stability involves with environmental conditions such as air temperature, air humidity, air pressure, and content of CO_2. However, the major effect of this system is air temperature, and it is sensitive than other parameters. For that reason, a short-term drift in length to the change of air temperature was measured by comparing with the fixed standard length. A fixed length of 150 mm standard long gauge block was used to determine stability of machine prototype. The measurement procedure is the same as discussed in **Section 3.3.3**. Both of a standard long gauge block and the measuring box were covered by a metal sheet for stabilizing temperature and protecting flow of air. After stabilized temperature, the measurements were performed five repetitions every 10 minutes in 1 hour.

Fig. 6.17 Measurement stability and accuracy of the machine prototype; a fixed length of standard long gauge block and the measuring box was installed under a metal sheet.

127

Photograph of the measurement is shown in **Fig. 6.17**, which the 150 mm standard LGB, measuring box, and environmental sensors were installed inside a metal sheet. Under environmental conditions of (22.87 ± 0.39) °C, (22.89 ± 0.15) % RH, and (100.89 ± 0.02) kPa, for air temperature, air humidity, and air pressure, respectively, the average of five measurement results is shown in **Fig.6.18**.
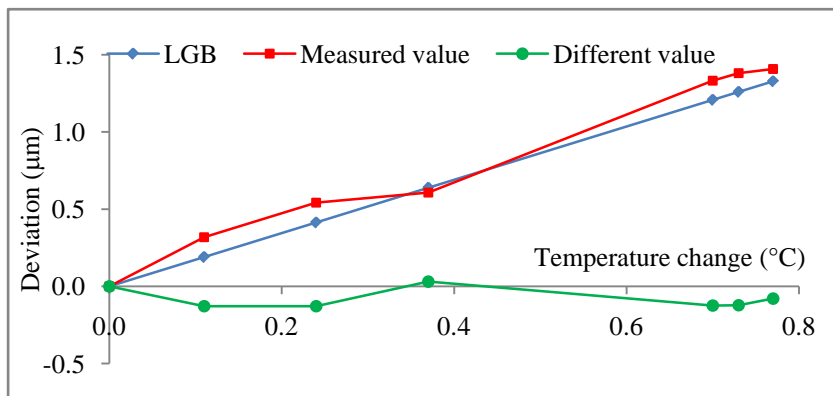
Fig. 6.18 Stability machine prototype to the change of air temperature.

In this experimental measurement, it is very hard to determine the drift of machine prototype, because a standard length of the LGB is always changed due to thermal expansion. However, the measured values (red line) by machine prototype should follow the expanded length of the LGB (blue line) due to thermal expansion, which is linear. Results show that the maximum difference between linear expanded lengths of the LGB and measured values is approximately −0.13 μm, when air temperature deviated by 0.77 °C. This experiment result might be summarized that the short-term drift of machine prototype is approximately −0.13 μm under conditions of (22.87 ± 0.39) °C, (22.89 ± 0.15) % RH, and (100.89 ± 0.02) kPa for air temperature, air humidity and air pressure. This measurement result is estimated that the gauge temperature on the LGB is equal to air temperature.

6.4.3 Accuracy of measuring system

The accuracy of measuring system has been confirmed by comparing with the standard length 150 mm of the LGB again. The measurement set up is the same as previous section.

The peak-to-peak distance of envelope interference fringe measurement is sensitive to the change of environmental conditions, especially ground vibration and the oscillating vibration of the voice coil actuator. These factors affect a large measurement standard deviation. In order to archive sub-micron measurement repeatability, a running average software function has been used to evaluate peak-to-peak distance of 30 samples before reporting of one measurement. In addition, the measurement should be performed as fast as

possible under controlled environmental conditions. As discussion, the repeatability of measurement is approximately 30 nm under the conditions of (21.51–21.54) °C, 22.4% RH, 100.99 kPa for air temperature, air humidity, and air pressure. Measurement results of 10 times repetition are summarized in **Table 6.3**.

Table 6.3 Accuracy of measuring system.

Average temperature	Length of LGB	Average measured	SD	Difference	Variation
°C	mm	value (mm)	μm	μm	μm
21.52	150.00262	150.00256	0.03	0.06	0.08

Additionally, the precision of machine prototype involves with resolution that is assigned by users, because peak detection method as explained in **Section 6.3.3** has an uncertainty at least a pair of achieving data per one peak. So that uncertainty of peak detection estimate to have a finite resolution of acquiring interference fringe as demonstrated in **Fig 6.19** and related to **Table 6.2**.
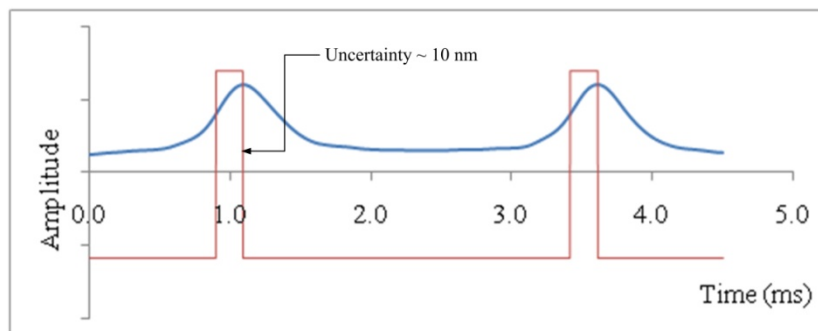
Fig. 6.19 Uncertainty due to peak detection method: a trigger signal (red line) has an uncertainty of 0.5 μs or approximately 10 nm for the sampling clock of 0.5 ms.

The accuracy of machine prototype has been estimated based on information as previous experiments. The evaluation of measurement uncertainty may be analyzed in two groups; relative and absolute terms. Relative term involves with pulsed interferometer and reflective index of air compensation, and absolute term relates to above discussed information. Thus, the measurement accuracy of machine prototype is summarized in **Table 6.4**, which standard uncertainties of absolute terms estimated to be rectangular distribution, except a corrected value of the comparison with a standard length of the LGB. However, Uncertainty due to thermal expansion of the LGB and the variation in length of winging film thickness terms are not considered.

As a result, the measurement accuracy of the absolute-length measuring machine prototype is estimated to be 0.26 μm/m, which the confidential level is approximately of 95%.

Table 6.4 The estimation of machine prototype accuracy.

Uncertainty sources	Standard uncertainty, $u(x_i)$	Sensitivity coefficient, c_i	Uncertainty contribution, $u(y_i)$
Relative term			
Repetition frequency stability	$2.89 \times 10^{-10}\, l$	1	$2.89 \times 10^{-10}\, l$
Refractive index of air compensation			
−Ciddor's equation	$< 10^{-8}$	l	$1.00 \times 10^{-8}\, l$
−Air humidity	0.17 %RH	$1.02 \times 10^{-8}\, l/\%RH$	$1.77 \times 10^{-9}\, l$
−Air temperature	0.02°C	$9.15 \times 10^{-7}\, l/°C$	$1.58 \times 10^{-8}\, l$
−Air pressure	17 Pa	$2.64 \times 10^{-9}\, l/Pa$	$4.57 \times 10^{-7}\, l$
Absolute term			
Time to length conversion	0.07 μm	1	0.07 μm
Peak detection of reference fringe	0.006 μm	1	0.006 μm
Peak detection of target fringe	0.006 μm	1	0.006 μm
Finite resolution	0.006 μm	1	0.006 μm
Repeatability	0.017 μm	1	0.017 μm
Difference from standard LGB	0.06 μm	1	0.06 μm
Stability	0.075 μm	1	0.075 μm
Combined uncertainty	$0.12\ \mu m + 4.94 \times 10^{-8}\, l$		
Expanded uncertainty ($k = 2$)	$[(0.24)^2 + (0.10 \times 10^{-3} l)^2]^{1/2}\ \mu m$		

Note that l is the nominal length expressed in mm.

6.5 Chapter conclusion

The first absolute-length measuring machine, (machine prototype) has been established, and automatic measurement software was developed. The measuring system was improved with a high accuracy of measurement. It is convenient for applications. It is very lightweight and easy to apply for CMM verification and also any absolute-length measurement in dimensional metrology, which are performed as a non-contact measurement. The basic specifications of machine prototype are summarized in **Table 6.5**.

Table 6.5 Machine prototype specifications.

Categories	Specifications
Measurand	Absolute length
Range	Step length of 150 mm up to 10.05 m
Resolution	10 nm
Repeatability	30 nm*
Accuracy	$[(0.24)^2 + (0.10 \times 10^{-3}l)^2]^{1/2}$ μm *
Stability	0.13 μm*
Traceability	Rb-frequency standard
Measuring box dimension	$(120 \times 235 \times 120)$ mm
-weight	~1 kg
Scanning box dimension	$(300 \times 300 \times 125)$ mm
-weight	~3 kg

*Note that measurement repeatability and accuracy were performed under controlled environmental conditions of (21.51–21.54) °C, 22.4% RH, 100.99 kPa for air temperature, air humidity, and air pressure. The stability was measured as a short-term drift in length, compared with linear expanded lengths of a 150 mm standard long gauge block in 1 hour under conditions of (22.87 ± 0.39) °C, (22.89 ± 0.15) % RH, and (100.89 ± 0.02) kPa, for air temperature, air humidity, and air pressure, respectively.

This machine prototype's performances are satisfied for CMM verification. In order to more improvement, a new scanning stage with a high precise translation is recommended. Because interference fringes directly affect by vibration of the scanning due to a scanning mirror is installed on a scanning device. In addition, several low-thermal expansion of standard fixed lengths should be used to evaluate machine performance, and several accuracy sensors are recommended to measure environmental conditions for automatic compensation, and the standard controlled laboratory shall be used for performing the tests.

Chapter 7 Conclusion

7.1 Thesis conclusion and discussion

This research presents a new optical measurement method of coordinate measuring machine verification following the International Standard of ISO 10360-2:2009 (acceptance and reverification tests for coordinate measuring machines, CMM). Standard has been introduced method to obtain machine performance by comparing with standard lengths. Five calibrated test lengths and seven measurement directions (four in space diagonals, and three parallel with CMM's axes) are required. Artifact-based methods, e.g. based on a series of gauge blocks, a step gauge, or a ball plate are limited in their application to small and medium-sized CMMs (measuring volume < 1 m^3). This technique cannot easily be applied to large CMMs, because artifacts cannot be simply up scaled. They become too heavy and hard to handle. Elasticity and thermal behavior of artifacts become critical to maintenance of the gauge accuracy.

Beyond artifact tests, optical instruments such as continuous-wave laser interferometers for length measurements are wildly used in dimensional field. The interference patterns are counted continuously during the motion of the measuring mirror. This relative displacement measurement technique is one of the most precise metrological tools. However, it has practical difficulties in the long-range measurement, because the target mirror should be installed for translating from the initial position to the final position continuously without any interruption. Moreover, for the long-distance measurements, the accuracy is affected by air turbulence and mechanical vibration, and therefore, is not easy to apply.

For optical three-dimensional measurement like a laser tracker, it is suitable for large structure with accuracy in micrometer scale. It is the combined measurement method between interferometer and two rotary encoders, which produces the spherical coordinate instrument. The accuracy of a laser tracker is therefore limited by the accuracy of azimuth and elevation angles due to mechanical assembly. Laser trackers can be used to measure volumetric errors of a CMM, and azimuth and elevation angles errors can be eliminated by multi-lateration measurement method. However, this technique needs laser tracker at least three stations.

The optical frequency comb is now become a standard for length and frequency measurements. It provides many precise lines of optical frequency and very short-pulse train. Many researchers have studied applications of the optical frequency comb for dimensional metrology, because it directly transfers a high accuracy of the primary standard to working standard lengths. The pulsed laser itself can construct a temporal coherence interference fringe patterns, and these fringes are used as the length standard for practical absolute-length measurements. The distance of constructive interference fringe between pulsed trains can be defined. It is inverse proportion by a repetition frequency of the laser source. Therefore, the

134

repetition frequency becomes a key to control a length standard. Normally, modification the repetition frequency directly inside a laser cavity is difficult, because the laser cavity is almost fixed. In this research, the external repetition rate modification of the C-fiber femtosecond laser is done by a fiber etalon. The repetition frequency of 100 MHz is transferred to a high frequency of 1 GHz that corresponds to the distance of constructive interference fringe of approximately 150 mm. Classically, an etalon or a Fabry–Pérot etalon can be composed by a pair of plane-parallel mirrors, concave mirrors, or an optical fiber with coating. However, the fiber type etalon is convenient and flexible for applications than other, and it is also less affected by surrounding conditions. In practice, a high-accurate length of a fiber etalon provides a high accuracy of free spectral range, and a high finesse presents a shaper transmission peaks with lower minimum transmission coefficient. The precise positions of constructive interference fringe relate to the accuracy of free spectral range, and amplitude power of interference fringe is proportional to finesse of an etalon. However, the constructive absolute position of interference fringe of any etalon can be measured by comparing with the known lengths such as standard lengths of gauge blocks or other interferometers.

General the constructive interference fringes of a single-mode fiber optical-comb pulsed interferometer are presented in the time domain. For practical absolute-length measurement, the conversion of time to length scale is required for determining the distance of peak-to-peak envelope interference fringes. Measurement of peak positions in unit of time, which is correlated to length scale, is the simplest way of the conversion. A high accuracy of linear gauge or other interferometers can be used for this measurement. The accuracy of the conversion factor is associated with the measurement method and accuracy of used instrument. This factor relates to the speed of the scanning device in the scanning arm of interferometer. Therefore, precise motion and a constant speed of a scanning device are required. The distance of peak-to-peak estimation by Gaussian fit curve function shows that the distance can be precisely achieved when two interference fringes are completely separated with each others. However, the peaks detection will be lost the accuracy if both sides of pattern fringes between the peaks are not symmetry. Asymmetry interference fringes can be caused by affecting of environmental conditions, imperfect optical alignment, and poor motion accuracy of a scanning device.

This research aims to develop a measuring system for CMM verification, which can be used to measure absolute length in three dimensions by a target. Thus, the sphere target type had been considered. The stylus tip of a CMM will be replaced by a sphere target. Then, the verified lengths are defined by a CMM controller comparing with absolute lengths of interferometer. First, metal balls had been experimented. Two factors affect the measurement; there are sphericity and surface roughness. The sphericity of the target directly affects to

optical path difference or accuracy of absolute length in three-dimensional measurements, but it is less significance for one dimension. For the surface roughness of the target, it strongly affects the amplitude power of interference fringe. The surface roughness (Ra) over 0.2 μm cannot reflect the laser beam at the optical path length over 3 m back to interferometer, while a smooth surface (small Ra) enhances power of interference fringe. In contrast, if too smooth surface of a sphere target, it cannot be used as well, because laser beam alignment is difficult, only a small area at the center of the metal ball reflects the light back to interferometer, other areas reject the beam out of the measuring axis. In application, a rough metal ball with a diameter of approximately 25 mm, and surface roughness of 0.1 μm had been selected as the target of a single-mode fiber optical-comb pulsed interferometer for CMM positioning accuracy measurements. The uncertainty of measurement is mainly caused by repeatability of peak detection. The repeatability of peak positions involves with interference fringes shape that relates to the surface roughness of the target. This target can be applied to measured absolute length up to 1.5 m, which achieves the measurement capability approximately 0.6 μm. By a rough metal ball target, the measuring range is limited due to a poor reflected beam of the target, and if the laser beam is misalignment of ± 0.2 mm from the center of the target, it may be caused an error of length measurement approximately 1 μm. However, a single-mode fiber optical-comb pulsed interferometer with a rough metal ball target is simply to construct, and this target can be applied only for low-accuracy measurements such as robotic arms, or arm CMMs, which performed as a non-contact absolute-length measurement.

According to measuring range limitation of the rough metal ball target, the ball lens with refractive index of 2 had been studied as the target of interferometer. Based on Snell's law, the incident light beam on a ball lens is refracted to the back focal point, and retracted the same path with incident beam in opposite direction that is a function of retroreflector. The total accuracy of the ball lens target depends on the accuracies of both the refractive index of glass material and the spherical fabrication. For one-dimensional length measurements, the sphericity of the ball lens does not affect the optical path length, but it significantly affects three-dimensional lengths measurements. Thus, the optical path error due to the target based on the proposed method can be ignored for CMM diagonal measurements. However, the reflected-beam intensity from the target is rapidly decreased, when the beam located far from the center of the target more than 0.15 mm. The best area on the target for achieving interference fringe is that the reflected-beam power should be sufficiently higher than 70% or around ± 0.3 mm from the center of target. If laser beam is misalignment of 0.3 mm, it may be caused of the cosine error less than 50 nm. Using a ball lens target, absolute length can be performed up to 10 m, cover the range of medium-sized to large-sized CMM applications. For diagonals CMM measurements, the initial zero positions of both CMM and a single-mode

fiber optical-comb pulsed interferometer are set when the order of interference fringe is $m \geq 1$. As a result, the difference indices between the reference plate and the ball lens target are automatically compensated by initial zero position. The proposed measurement method was compared with the standard artifact method for diagonal in space measurements. The experimental results show that the measurement accuracy depends on noise in the interference fringe caused by airflow fluctuations and mechanical vibrations. However, measurement uncertainty is smaller than that of the artifact test method due to less effects of air temperature. In addition, the measurement time of the proposed method is 60% less than that of the artifact-test method because of its shorter start-up time; the proposed method can be used in measurements after 30 minutes system warm-up, while the artifact method requires a waiting period of more than 3 hours to achieve a stabilized gauge temperature for each alignment. Moreover, the alignment procedure is easier in the proposed system because of the compact and convenient optical components. However, the proposed method is a non-contact one, and therefore its CMM verification does not include effects of the CMM probing system.

The results of experimental measurements show that the single-mode fiber optical-comb pulsed interferometer with a ball lens target successfully encourage goals of the thesis. Subsequently, the prototype of absolute-length measuring system and automatic measurement software has been developed. The machine prototype consists of two optical boxes, which are separated. There are a scanning box and a measuring box. Both optical boxes are connected together through a single-mode optical fiber. Due to separated design, a measuring part can be placed for measurement around the working area, while a scanning part can be fixed as a stationary that make the measurement system easily for real applications. In addition, the automatic measurement software was developed based on LabVIEW programming platform, which the absolute length under measurement is directly reported on the computer screen. The precise peak detection function is applied by the measurement software. It precisely detects peak positions, because only peak of each envelope interference fringe is detected. The error of peak position detection is approximately 10 nm. Additionally, the basic performances of a prototype have been confirmed by comparing with a standard fixed length under controlled measurement conditions. The measurement repeatability is approximately 30 nm with resolution of 10 nm, a short term stability is approximately 130 nm and measurement accuracy is approximately $[(0.24)^2 + (0.10 \times 10^{-3}l)^2]^{1/2}$ μm, where l is the indication length expressed in mm. The absolute-length measuring system is satisfied for CMM verification, and also can be applied for any non-contact absolute-length measurement in dimensional metrology with a high accuracy requirement.

Summary, the new optical measurement method based on the single-mode fiber optical-comb pulsed interferometer with the ball lens target successfully encourage goals of the thesis. All our requirements agree with the research goals as summarized in **Table 7.1**. This technique is therefore having a good impact to industries, because the measurement procedure is simply and less time consumption. Moreover, it has a high efficiency for the medium-sized to large-sized CMM verifications, long-measuring range up to 10 m with a small measurement uncertainty due to less effect by surrounding conditions. In addition, the first complete set of the absolute-length measuring machine can be applied to measure other absolute lengths, which is performed as a non-contact measurement. Furthermore, this study provides background knowledge for development of the calibration system that details are explained in the next section. The proposed research is therefore intended to make contributions to the literatures on coordinate metrology, and variety on dimensional metrology.

Table 7.1 Summary of thesis achievements.

Categories	Goals	Achievements
Main propose	Application for CMM verification	○
CMMs target	Medium-sized to large-size CMM	○
Measurand	Absolute length	○
Measurement method	Non-contact pulsed interferometer	○
Target of interferometer	Spherical target	○ Ball lens (index:2)
Measuring range	Up to 10 m	○
Measurement accuracy	Better than 1 μm/m	○ ~0.26 μm/m (k=2)
Resolution	~10 nm	○
Stability	~50 nm/h	Δ ~130 nm/h
Traceability	International Standard or SI base unit	○

7.2 Future work

For future work, the volumetric of CMM calibration to identify 21-parametric errors will be conducted by applying the absolute-length measuring systems with a ball lens target. Following this section explains the concept idea of how to conduct the research and what the requirement of next step is.

The concept of calibration system is the comparisons between the machine coordinates system (MCS) and the absolute coordinates system (ACS), which is measured by the proposed method, so then parametric errors of a CMM can be analyzed [71].
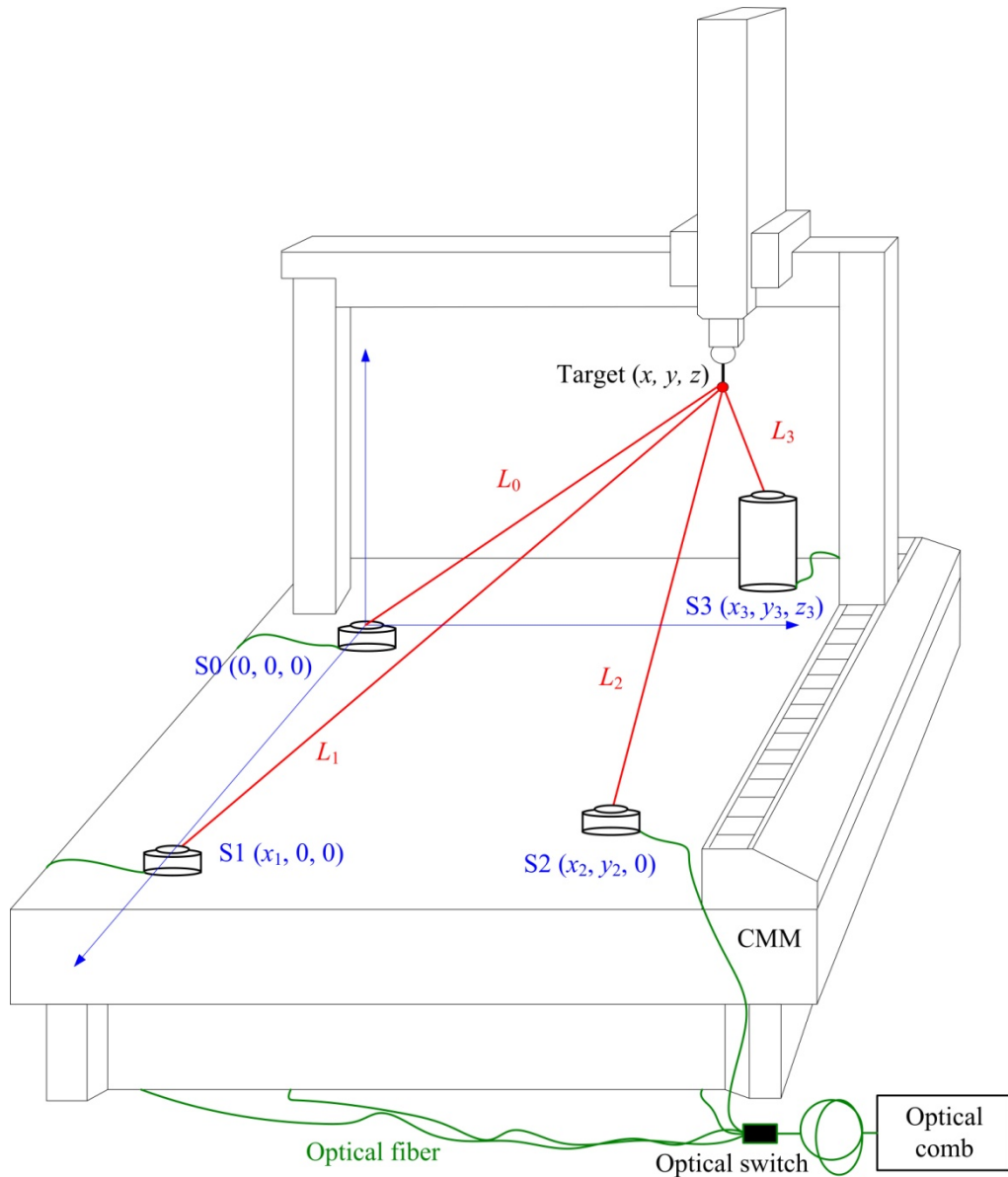
Fig. 7.1 CMM volumetric calibration using optical-comb pulsed tracking system.

Based on multi-lateration measurement method, The ACS can be measured using only lengths (radial measurement) from at least three laser trackers [72–73]. A target point (x, y, z) as shown in **Fig. 7.1**, is obtained by the intersection of the three spherical coordinates defined by only radial component of each tracker station (S0–S2). Equations (7.1)–(7.3) provide the length obtained by the measurement of each tracker, respectively as:

$$L_0^2 = (x - x_0)^2 + (y - y_0)^2 + (z - z_0)^2 \tag{7.1}$$

$$L_1^2 = (x - x_1)^2 + (y - y_1)^2 + (z - z_1)^2 \tag{7.2}$$

$$L_2^2 = (x - x_2)^2 + (y - y_2)^2 + (z - z_2)^2 \tag{7.3}$$

The intersection point coordinates calculated by three spheres is a transform of the quadratic equations system, which target coordinates are generated by trackers. If locations positions in coordinates system of each tracker are known, then the relation of target point and measuring lengths from **Fig.7.1** are:

$$x = \frac{(L_0^2 - L_1^2 + x_2^2)}{2x_1} \tag{7.4}$$

$$y = \frac{(L_0^2 - L_1^2 + x_2^2 + y_2^2 - 2xx_2)}{2y_2} \tag{7.5}$$

$$z = \pm(L_0^2 - x^2 - y^2)^{1/2} \tag{7.6}$$

The sign ambiguity in z-axis obtained in **Eq. 7.6** can be avoided by forth tracker (P3), which is located at (x_3, y_3, z_3) position as shown in **Fig. 7.1**. The reference system of S3 should belong to a plane difference from the plane xy formed by the other three trackers reference system [74]. Finally, the (x, y, z) target coordinates are obtained in the rotation-translation linear matrix as shown in **Eq. 7.7**.

$$\begin{bmatrix} x \\ y \\ z \end{bmatrix} = -0.5 \begin{bmatrix} \dfrac{1}{x_1} & 0 & 0 \\ -\dfrac{x_2}{x_1 y_2} & \dfrac{1}{y_2} & 0 \\ -\left(\dfrac{x_3}{x_1 z_3}\right) + \left(\dfrac{x_2 y_3}{x_1 y_2 z_3}\right) & -\dfrac{y_3}{y_2 z_3} & \dfrac{1}{z_3} \end{bmatrix} \begin{bmatrix} L_1^2 - L_0^2 - x_1^2 \\ L_2^2 - L_0^2 - x_2^2 - y_2^2 \\ L_3^2 - L_0^2 - x_3^2 - y_3^2 - z_3^2 \end{bmatrix} \tag{7.7}$$

In application, the target coordinates will be considered as identification points compared with nominal points of a CMM coordinates system. If many points of a working volume CMM are identified, the 21-parametric errors of a CMM can be analyzed from these points [72–74].

From above discussion, the volumetric of a CMM calibration based on multi-lateration measurement method as shown in **Fig. 7.1** is required the tracking system for the measurement of each length from tracker to target. Although the angle information is not required in this technique, each tracker station still needs continuously track the target for synchronized lengths. Next task laser trackers based on a single-mode fiber optical-comb pulsed interferometer will be developed. Using a dome glass as a first reference of interference fringe is an idea of a low-cost absolute-length laser tracker, a poor accuracy mechanism of tracking system can be applied for reducing cost of the measuring system. Each tracker station will be connected with an optical comb via an optical switch. By applying dome glass, the accuracy of absolute-length measurements will relate to the spherical accuracy of the dome glass reference than those angular encoders of mechanical tracking system. The main task of the next research is that how to collimate the reflected beam form the dome glass and the target back to a single-mode fiber interferometer, because the concave surface is almost difficult to laser beam alignment. The high surface quality of a dome glass may be required in order to achieve high reflected-beam power. In addition, the continuous lengths observation form each tracker to the target may be required. In this case, a new fiber etalon with 3–GHz FSR and a scanning device with travel length over 30 mm will be considered, respond to absolute length 50 mm and scanning range over ± 30 mm, respectively.

Additionally, for three dimensional measurements by single-mode fiber optical-comb pulsed interferometers more than one system with a ball lens target, some factors have to be concerned. For examples, the refractive index of ball lens target has to be compensated, because lengths will be determine from the referent positions to the center of a sphere target rather than that from the back focal point of ball lens. In addition, this technique is not

141

142

completely pure absolute-length measurement due to optical delay in the scanning-arm interferometer. Therefore, high measurement repeatability can be achieved, when referent fringe and target fringe are completely separated (peak-to-peak distance ~100 μm). For accuracy and stability of the measuring system, heat that generated by a scanning device in the reference arm interferometer may change the optical path length, affecting the conversion factor of time to length scale, and measurement stability.

Reference

[1] P. Howarth, F. Redgrave: "Metrology - in short," *EURAMET project 1011*, 3rd edition, July 2008.

[2] D. Flack, J. Hannaford: "Fundamental good practice in dimensional metrology," *NPL-a national measurement good practice guide*, No. 80, 2005.

[3] International vocabulary of metrology−Basic and general concepts and associated terms (VIM), 3rd edition, JCGM 200:2012.

[4] Evaluation of measurement data−Guide to the expression of uncertainty in measurement, GUM 1995 with minor corrections, 1st edition, JCGM 100:2008.

[5] ISO 10360-1, Geometrical Product Specifications (GPS) −Acceptance and reverification tests for coordinate measuring machines (CMM) −Part 1: Vocabulary, 2000.

[6] D. Flack: "CMM Verification," *NPL-a national measurement good practice guide*, No. 42, 2011.

[7] M. Abbe, K. Takamasu, S. Ozono: "Reliability on calibration of CMM," Measurement, No. 33, pp. 359–68, 2003.

[8] K. Takamasu, R. Furutani, T. Kurosawa, T. Takatsuji, F. Wäldele, H. Schwenke, N. Brown, E. Jaatinen: "International Standard Development of Virtual CMM," *Final Research Report NEDO International Joint Research Project FY 1999 - FY 2001*, May 2002.

[9] ISO 10360-2, Geometrical Product Specification (GPS). Acceptance and reverification tests for coordinate measuring machines (CMM). Part 2: CMMs used for measuring linear dimensions, International Organization for Standardization, 2009.

[10] JIS B 7440-2, Japanese Industrial Standard for Geometrical product specifications (GPS) − Acceptance and reverification tests for coordinate measuring machines (CMM) −Part 2: CMMs used for measuring linear dimensions, 2013.

[11] BS 6808-2, British Standards Coordinate measuring machines; Methods for verifying performance, 1987.

[12] ASME B89.1.12M, American Society of Mechanical Engineers Measurement −Methods For Performance Evaluation Of Coordinate Measuring Machines, 1990.

[13] VDI/VDE 2617 Blatt 2.1, German Standard, Accuracy of coordinate measuring machines −Parameters and their reverification −Code of practice for the application of DIN EN ISO 10360-2 for length measurement, 2014−03.

[14] S.D. Phillips, D. Sawyer, B. Borchardt, D. Ward, D.E. Beutel: "A novel artifact for testing large coordinate measuring machines," *Precision Engineering*, Vol.25, pp. 29−34, 2001.

[15] L. Arriba, E. Trapet, M. Bartscher, M. Franke, A. Balsamo, G. Costelli, S. Torre4, F. Kitzsteiner, F. San Martín: "Method and artifacts to calibrate large CMMs," European standards measurements and testing programme, project SMT4-PL97-2330, 1999.

[16] K. Wendt, H. Schwenke, F. Wäldele, M. Krawczyk, K. Kniel: "Error mapping of large CMMs by sequential multi-lateration using a laser tracker," *Proceeding of 2nd euspen international conference*, 2001.

[17] H. Schwenke, R. Schmitt, P. Jatzkowski, C. Warmann: "On-the-fly calibration of linear and rotary axes of machine tools and CMMs using a tracking interferometer," *CIRP Annals - Manufacturing Technology* Vol. 58, pp. 477−80, 2009.

[18] A. Gąska, M. Krawczyk, R. Kupiec, K. Ostrowska, P. Gąska, J. Sładek: "Modeling of the residual kinematic errors of coordinate measuring machines using LaserTracer system," *International Journal of advance manufacturing and technology*, Vol. 73, pp. 497−07, 2014.

[19] ISO 10012, Measurement management systems −Requirements for measurement processes and measuring equipment, 2003.

[20] BE. A. Saleh, M.C. Teich: "Fundamental of Photonics," *John Wiley & Sons, Inc.*, pp. 531−36, 1991.

[21] J. Liu: "*Photonic Devices*," Cambridge University Press, pp. 718−35, 2009.

[22] C. Rullière: "Femtosecond Laser Pulses -principles and experiments," *Springer*, pp.53–2, 1998.

[23] O. Svelto: "Principles of Lasers," 5th ed., *Springer*, pp.339–46, 2010.

[24] J. Ye, S. T. Cundiff, "Femtosecond Optical Frequency Comb: Principle, Operation, and Applications," *Springer*, pp. 12–2, 2004.

[25] S. T. Cundiff, J. Ye: "Femtosecond optical frequency combs," *Reviews of modern physics*, Vol.75, No.1, pp. 325–42, 2003.

[26] D. J. Jones, S. A. Diddams, J. K. Ranka, A. Stentz, R. S. Windeler, J. L. Hall, S. T. Cundiff: "Carrier-Envelope Phase Control of Femtosecond Mode-Locked Lasers and Direct Optical Frequency Synthesis", *Science*, Vol. 288, No. 5466, pp. 635–39, 2000.

[27] R. Holzwarth, Th. Udem, T. W. Hänsch: "Optical Frequency Synthesizer for Precision Spectroscopy," *Physical Review Letters*, Vol. 85, No. 11, pp. 2264–67, 2000.

[28] H. Inaba, Y. Nakajima, FL. Hong, K. Minoshima, J. Ishikawa, A. Onae, H. Matsumoto, M. Wouters, B. Warrington, N. Brown: "Frequency Measurement Capability of a Fiber-Based Frequency Comb at 633 nm," *IEEE Transactions on Instrumentation and Measurement*, Vol. 58, No. 4, pp. 1234–40, 2009.

[29] K. Minoshima, H. Matsumoto: "High-accuracy measurement og 240-m distance in an optical tunnel by use of a compact femtosecond laser," *Applied Optics*, Vol. 39, No. 30, pp. 5512–17, 2000.

[30] H. Matsumoto, X. Wang, K. Takamasu, T. Aoto: "Absolute measurement of baselines up to 403 m using heterodyne temporal coherence interferometer with optical frequency comb", *Applied Physics Express*, Vol. 5, pp. 046601−1−3, 2012.

[31] X. Wang, S. Takahashi, K. Takamasu, H. Matsumoto: "Space position measurement using long-path heterodyne interferometer with optical frequency comb," *Optics Express*, Vol. 20, No. 3, pp. 2725–32, 2012.

[32] X. Wang, S. Takahashi, K. Takamasu, H. Matsumoto: "Spatial positioning measurements up to 150 m using temporal coherence of optical frequency comb", *Precision Engineering*, Vol. 37, pp. 635–39, 2013.

[33] C. Narin, S. Takahashi, K. Takamasu, H. Matsumoto: "Step gauge measurement using high-frequency of a mode-locked fiber laser," *Proceeding of XX IMEKO Wold Congress, Metology for Green Growth*, Busan, Korea, pp. 177–81, 2012.

[34] N. Schuhler, Y. Salvadé, S. Lévêque, R. Dändliker, R. Holzwarth: "Frequency-comb-referenced two-wavelength source for absolute distance measurement, " *Optics Letters*, Vol. 31, No. 21, pp. 3101–03, 2006.

[35] SW. KIM, YJ. KIM: "Advanced optical metrology using ultrashort pulse laser," *Review of Laser Engineering*, Vol 36, pp. 1254–57, 2008.

[36] N. R. Doloca, K. Meiners-Hagen, M. Wedde, F. Pollinger, A. Abou-Zeid: "Absolute distance measurement system using a femtosecond laser as amodulator," *Measurement Science and Technology*, Vol. 21 pp. 115302–1–7, 2010.

[37] S. Hyun, YJ. Kim, Y. Kim, J. Jin, SW. Kim: "Absolute length measurement with the frequency comb of a femtosecode laser," *Measurement Science and Technology*, Vol. 20, pp. 095302–1–6, 2009.

[38] J. Jin, SW. Kim: "Precision Dimensional Metrology Based on a Femtosecond Pulse Laser, *Advances in Solid State Lasers Development and Applications*," Available from: http://www.intechopen.com/books/advances-in-solid-state-lasersdevelopment-and-applic ations/precision-dimensional-metrology-based-on-a-femtosecond-pulse-laser, 2010.

[39] PE. Ciddor: "Refractive index of air: new equations for the visible and near infrared," *Applied* optics, Vol. 35, No. 9, pp. 1566–73, 1995.

[40] PE. Ciddor: "Refractive index of air. 2. Group index," *Applied optics*, Vol. 38, No. 9, pp. 1663–67, 1998.

[41] Y. Yamaoka, K. Minoshima, H. Matsumoto: "Direct measurement of the group refractive index of air with interferometry between adjacent femtosecond pulses," *Applied optics*, Vol. 41, No. 21, pp. 4318–32, 2002.

[42] H. Matsumoto, K. Sasaki, A. Hirai: "Remote measurement of refractive index of air using tandem interferometer over long optical fiber," *Japanese Journal of Applied Physics*, Vol. 47, No. 9, pp. 7386–89, 2008.

[43] H. Matsumoto, K. Sasaki, A. Hirai: "In situ measurement of group refractive index using tandem low-coherence interferometer," *Optic Communications*, 266, pp.214−7, 2006.

[44] A. Hirai, H.Matsumoto: "Low-coherence tandem interferometer for measurement of group refractive index without knowledge of the thickness of the test sample," *Optics letters*, Vol. 28, No. 21, pp.2112–14, 2003.

[45] J. C. Owens: "Optical refractive index of air: dependence on pressure, temperature and composition," *Applied optics*, Vol. 6, No. 1, pp. 51–59, 1967.

[46] B. Edlén: "The refractive index of air," *Metologia*, Vol. 2, No. 2, pp. 71−80, 1966.

[47] K. P. Birch, M. J. Downs: "An update Edlén equation for the refractive index of air," *Metrologia*, Vol. 30, pp. 155–62, 1993.

[48] J. M. YAUGHAN: "The Fabry-Perot Interferometer History, Theory, Practice and Applications," *New York, NY 10016*, 1989.

[49] B. E. A. Saleh, M. C. Teich: "Fundamentals of Photonics," *John Wiley & Sons*, 2ed, 2007.

[50] FT. S. Yu, S. Yin: "Fiber Optic Sensors", *Marcel Dekker, New York*. 2002.

[51] R. Šmíd, O. Číp, J. Lazar: "Precise length etalon controlled by stabilized frequency comb," *Measurement science review*, Vol. 8, No. 5, pp. 114–17, 2008.

[52] N. Chanthawong, S. Takahashi, K. Takamasu, H. Matsumoto: "Performance evaluation of a coordinate measuring machine's axis using a high-frequency repetition mode of a mode-locked fiber laser," *International Journal of Precision Engineering and Manufacturing*, Vol.15, Issue 8, pp. 1507–12, 2014.

[53] T. Doi, K. Toyoda, Y. Tanimura: "Effects of phase changes on reflection and their wavelength dependence in optical profilometry," *Applied optics*, Vol. 36, No. 28, pp. 7157–61, 1997.

[54] K. Sugimoto, S. Matsuda, Y. Ogiwara, K. Kitamura: "Microscopic Ellipsometric Observation of the Change in Passive Film on 18Cr-8Ni Stainless Steel with the Initiation and Growth of Pit," *Electrochemical Science and Technology*, Vol. 132, No 8, pp.1791–95, 1985.

[55] T. Doiron, J. Beers: "The Gauge Block Handbook," Dimensional Metrology Group Precision Engineering Division, National Institute of Standards and Technology, Available from: http://emtoolbox.nist.gov/Publications/NISTMonograph180.pdf, pp. 134–39.

[56] F.G. Thwaite: "Phase correction in the interferometric measurement of end standard," *Metrologia*, Vol. 14, pp. 53–62, 1978.

[57] H. Matsumoto, L. Zeng: "Simple compensation method for winging errors in the interferometric calibration of gauge blocks," *Metrologia*, Vol. 33, pp. 1–4, 1996.

[58] W. Sudatham, H. Matsumoto, S. Takahashi, K. Takamasu: "Verification of the positioning accuracy of industrial coordinate measuring machine using optical-comb pulsed interferometer with a rough metal ball target," *Precision Engineering*, Vol. 41, pp. 63–7, 2015.

[59] ISO 4287, Geometrical Product Specifications (GPS) −Surface texture: Profile method − Terms, definitions and surface texture parameters, ISO 4287:1997/Amd 1:2009.

[60] W. Sudatham, H. Matsumoto, S. Takahashi, K. Takamasu: "Non-contact measurement technique for dimensional metrology using optical comb," *Measurement*, Vol. 78, pp. 381–87, 2016.

[61] ISO 1. Geometrical product specification (SPC). Standard reference temperaturefor geometrical product specification and verification. International Organiza-tion for Standardization; 2002.

[62] EA-4/02, "Evaluation of the uncertainty of measurement in calibration," *European accreditation*, Rev. 01, EA-4/02 M: 2013.

[63] M3003, "The expression of uncertainty and confidence in measurement," *UKAS*, United Kingdom accreditation service, 3rd ed., 2012.

[64] T. Takatsuji, M. Goto, S. Osawa, R. Yin, T. Kurosawa: "Whole-viewing-angle cat's-eye retroreflector as a target of laser trackers," *Measurement Science Technology*. Vol.10, pp. N87–N90, 1999.

[65] O Nakamura, M Goto, K Toyoda, N Takai, T Kurosawa: "A laser tracking robot-performance calibration system using ball-seated bearing mechanisms and a spherically shaped cat's-eye retroreflector", Review Scientific Instruments. Vol. 65 No. 4, pp.1006–11, 1994.

[66] A. Weckenmanna, T. Estlerb, G. Peggsc, D. McMurtryd: "Probing systems in dimensional metrology," *CIRP Annals-Manufacturing Technology*, Vol. 53, pp. 657–84, 2004.

[67] W. Sudatham, H. Matsumoto, S. Takahashi, K. Takamasu: "Diagonal in space of coordinate measuring machine verification using an optical-comb pulsed interferometer with a ball-lens target," *Precision Engineering*, Vol. 43, pp. 486–92, 2016.

[68] ISO 17043, Conformity assessment−General requirements for proficiency testing, 2010.

[69] DAQ M Series User Manual NI 622x, NI 625x, and NI 628x Devices, 371022K-01, National Instruments Corporation, July 2008.

[70] N. Chanthawong, S. Takahashi, K. Takamasu, H. Matsumoto: "A new method for high-accuracy gauge block measurement using 2 GHz repetition mode of a mode-locked fiber laser", Meas. Sci. Technol. Vol. 23, pp. 1−6, 2012.

[71] E. Trapet, F. WiUdele: "A reference object based method to determine the parametric error components of coordinate measuring machines and machine tools Measurement", *Measurement*, Vol. 9, No. 1, pp. 17–22, 1991.

[72] JJ. Aguilar, S. Aguado, D. Samper: "Mutilateration in volumetric verification of machine tool", *XX IMEKO World Congress*, 2012.

[73] K. Umetsu, R. Furutnani, S. Osawa, T. Takatsuji, T. Kurosawa: "Geometric calibration of a coordinate measuring machine using a laser tracking system", *Meas. Sci. Technol.*, Vol. 16, pp.2466–72, 2005.

[74] T. Takatsuji, M. Goto, A. Kirita, T. Kurosawa, Y. Tanimura: "The relationship between the measurement error and the arrangement of laser trackers in laser trilateration", *Meas. Sci. Technol.* Vol. 11, pp. 477–83, 2000.

Acknowledgment

<div align="right">
Wiroj SUDATHAM

ウィロート　スダータム

วิโรจน์ สุดาธรรม

Department of Precision Engineering,

The University of Tokyo, 2016
</div>

Publication list

Journal Papers

Wiroj Sudatham, Hirokazu Matsumoto, Satoru Takahashi, Kiyoshi Takamasu: "Non-contact measurement technique for dimensional metrology using optical comb," *Measurement*, Vol. 78, pp. 381–87, 2016.

Wiroj Sudatham, Hirokazu Matsumoto, Satoru Takahashi, Kiyoshi Takamasu: "Diagonal in space of coordinate measuring machine verification using an optical-comb pulsed interferometer with a ball-lens target," *Precision Engineering*, Vol. 43, pp. 486–92, 2016.

Wiroj Sudatham, Hirokazu Matsumoto, Satoru Takahashi, Kiyoshi Takamasu: "Verification of the positioning accuracy of industrial coordinate measuring machine using optical-comb pulsed interferometer with a rough metal ball target," *Precision Engineering*, Vol. 41, pp. 63–7, 2015.

International Conference Proceedings

1st–5th June, 2015, euspen 2015, Wiroj Sudatham, Hirokazu Matsumoto, Satoru Takahashi, Kiyoshi Takamasu: "Absolute precision measurement for space coordinates metrology using an optical-comb pulsed interferometer with a ball lens target," pp. 109–10, Leuven, Belgium.

2nd–5th September, 2014, 11th IMEKO Symposium LMPMI 2014, Wiroj Sudatham, Hirokazu Matsumoto, Satoru Takahashi, Kiyoshi Takamasu: "Non-contact measurement technique for dimensional metrology using optical comb," A25, Tsukuba, Japan.

Domestic Conference Proceedings

4th–6th September, 2015, JSPE Autumn Meeting (2015 年度秋季大会 (東北大学) について), Wiroj Sudatham, Hirokazu Matsumoto, Satoru Takahashi, Kiyoshi Takamasu: "Temporal-Coherence Interferometer Using Optical Comb for CMM Verification (3rd Report) – CMM diagonal measurements –", B67, Tohoku.

10th April, 2015, KEK| High Energy Accelerator Research Organization-workshop, 第 16 回高エネ研メカ・ワークショップ報告集（2015.4.10）, Wiroj Sudatham, Hirokazu Matsumoto, Satoru Takahashi, Kiyoshi Takamasu: "Temporal-Coherence Interferometer Using Optical Comb for CMM Verification", Tsukuba.

17th–19th March, 2015, JSPE Spring Meeting (2015 年度春季大会（東洋大学）について), Wiroj Sudatham, Hirokazu Matsumoto, Satoru Takahashi, Kiyoshi Takamasu: "Temporal-Coherence Interferometer Using Optical Comb for CMM Verification (2nd Report) –Pulsed interferometer with a ball lens target –", C44, Tokyo.

9th –10th December, 2014, 54th Meeting on Lightwave Sensing Technology, (第 54 回光波センシング技術研究会, 東京理科大学), Wiroj Sudatham, Hirokazu Matsumoto, Satoru Takahashi, Kiyoshi Takamasu: "High accuracy measurement method for coordinate measuring machine using fast optical comb and ball lens", pp. 125–29, Tokyo.

16th–18th September, 2014, JSPE Autumn Meeting (2014 年度秋季大会（鳥取大学）について), Wiroj Sudatham, Hirokazu Matsumoto, Satoru Takahashi, Kiyoshi Takamasu: "Temporal-Coherence Interferometer Using Optical Comb for CMM Verification (1nd Report) – Pulsed interferometer with a rough metal ball target –", Q26, Tottori.

18th –19th June, 2014, 53rd Meeting on Lightwave Sensing Technology, (第 53 回光波センシング技術研究会, 東京理科大学), Wiroj Sudatham, Hirokazu Matsumoto, Satoru Takahashi, Kiyoshi Takamasu: "New absolute length-measuring technique for industrial CMM using optical-comb pulsed interferometer", pp. 65–71, Tokyo.

Award

Excellent Paper Award, 11th IMEKO Symposium LMPMI 2014 (2nd–5th September), Wiroj Sudatham, Hirokazu Matsumoto, Satoru Takahashi, Kiyoshi Takamasu: "Non-contact measurement technique for dimensional metrology using optical comb," A25, Tsukuba, Japan.

Appendix

```matlab
%=================================================
% Simulation of sinusoidal modes are fixed;
% and random phase orientations of pulsed laser.
%=================================================
E0 = 1; %Assume an ammplitude
factor1 = 0;
factor2=10;
t = -1.5:1/1000:1.5;
Ein = 0;
Eout=0;
% Case of all modes are the same phase.
for f = 1:31
phase1 = rand*factor1;
Einphase = E0*cos(2*pi*f*t+phase1);
Ein = Ein+Einphase;
end
% Case of all modes are random phase.
for f = 1:31
phase2 = rand*factor2;
Eoutphase = E0*cos(2*pi*f*t+phase2);
Eout = Eout+Eoutphase;
end
plot(t,abs(Ein.^2),'r',t,abs(Eout.^2),'b');
%=================================================
```

Fig. A1 MATLAB simulation codes of sinusoidal modes are fixed and random phase orientations of pulsed laser.

```matlab
%=========================================================
% Simulation of Airy function for different reflection
% coefficients of the idea etalon.
%=========================================================
delta=0:1/40:2;      % Defind delta (phase)
R1=0.85;                   % Defind each reflection coeff.
R2=0.60;
R3=0.40;
F1=4*R1/(1-R1).^2;       % Finess calculations
F2=4*R2/(1-R2).^2;
F3=4*R3/(1-R3).^2;
T1=1./(1+F1.*sin(delta*pi).^2); % Airy function calculations
T2=1./(1+F2.*sin(delta*pi).^2);
T3=1./(1+F3.*sin(delta*pi).^2);
figure;%plot as a function of delta (0 to 2pi)
plot(delta,T1,'r',delta,T2,'b',delta,T3,'g');
%=========================================================
```

Fig. A2 MATLAB simulation codes of Airy function for different reflection coefficient of the ideal etalon as a function of phase difference (δ).
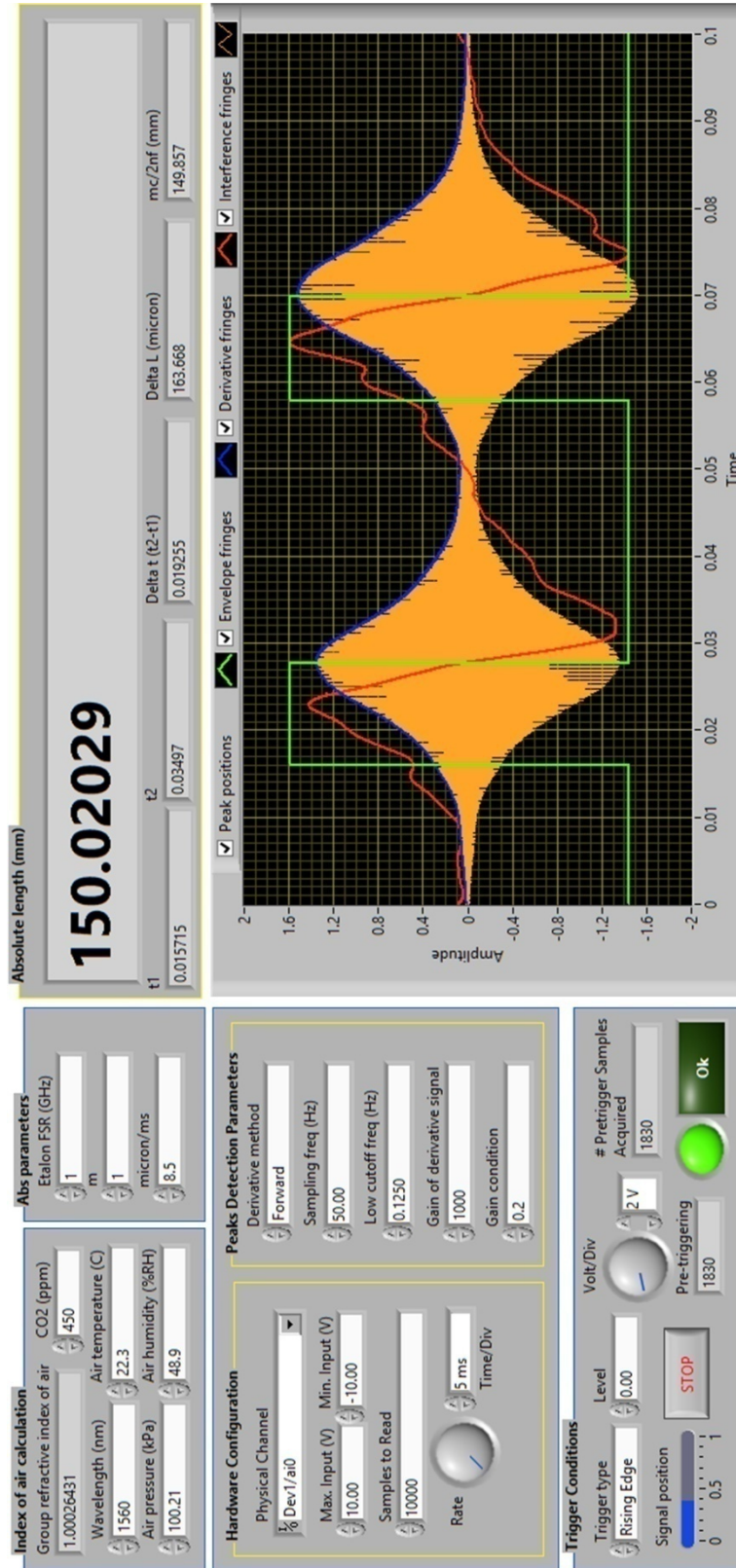
Fig. A3 User interface of absolute-length measurement software.
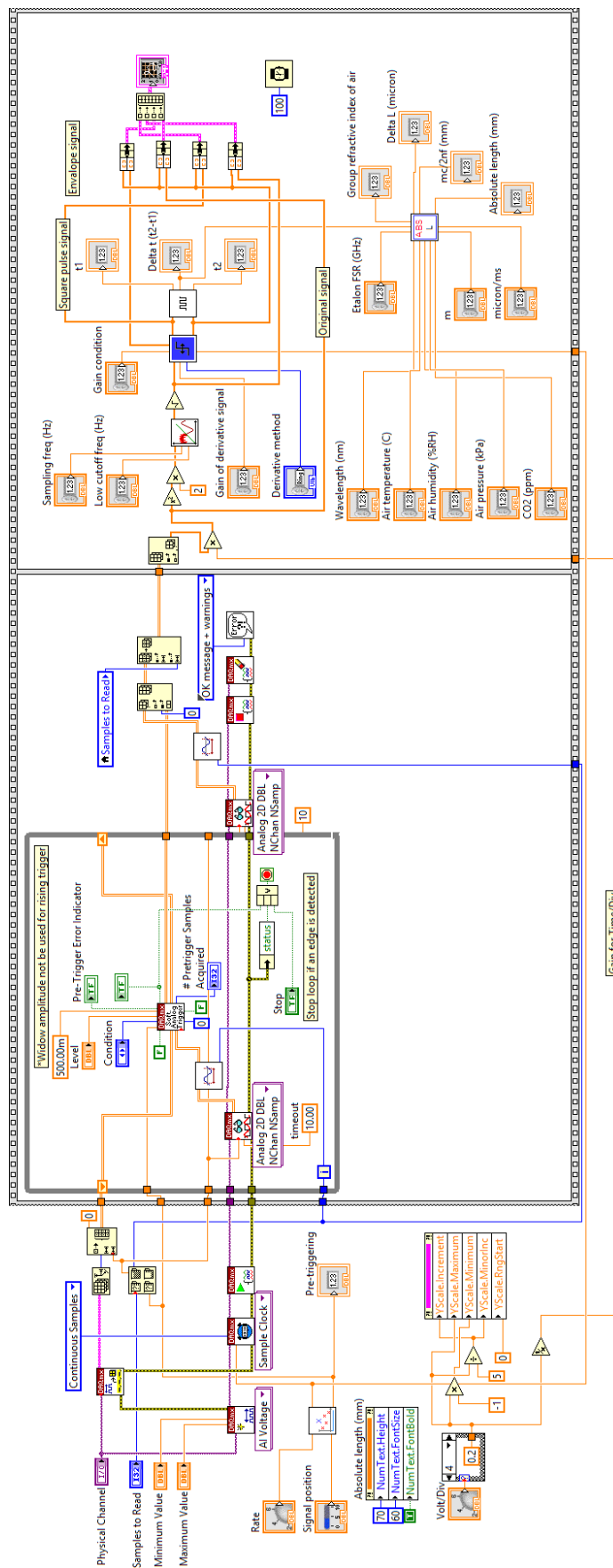
Fig. A4 Main absolute-length measurement software function.
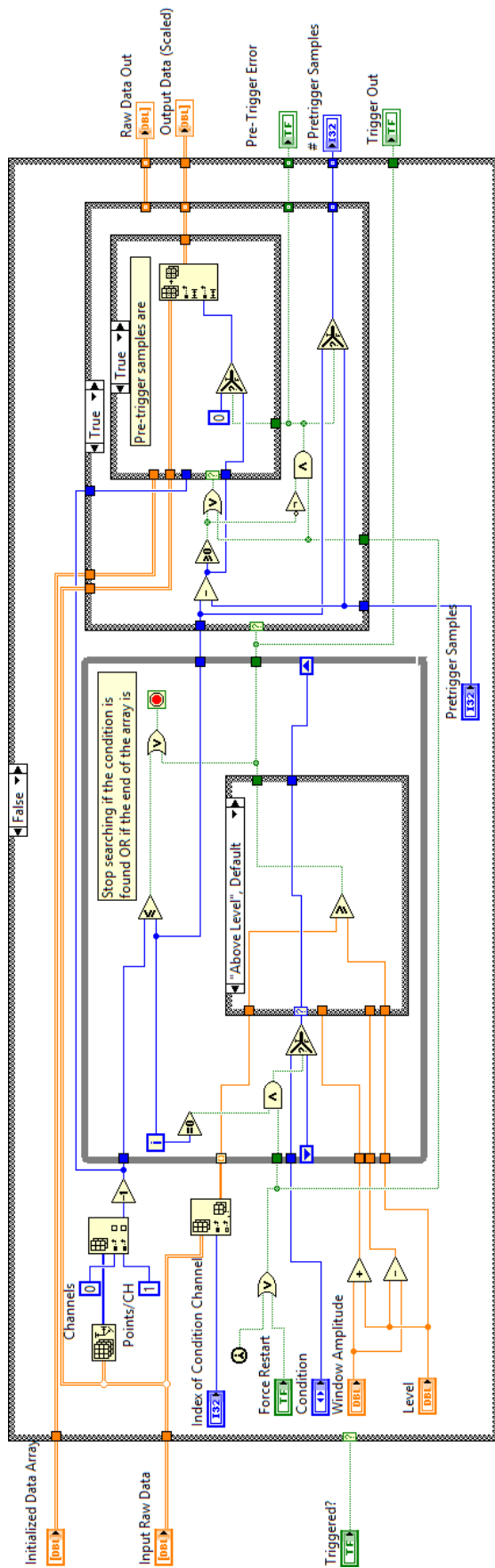
Fig. A5 Pre-triggering condition function.
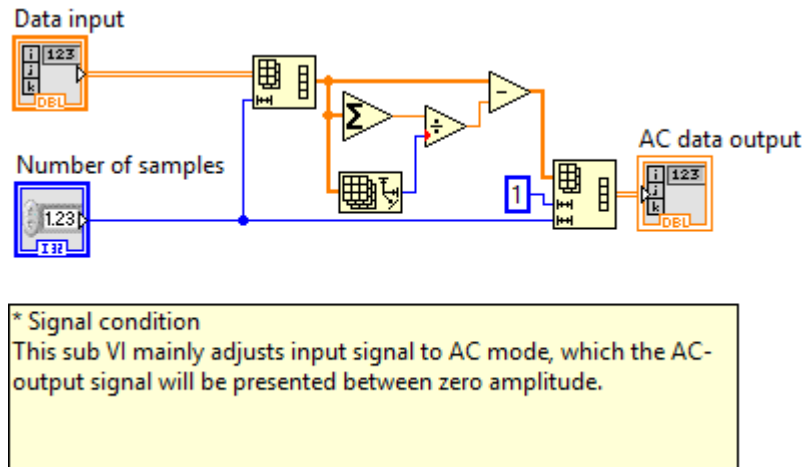
Fig. A6 AC signal condition function.
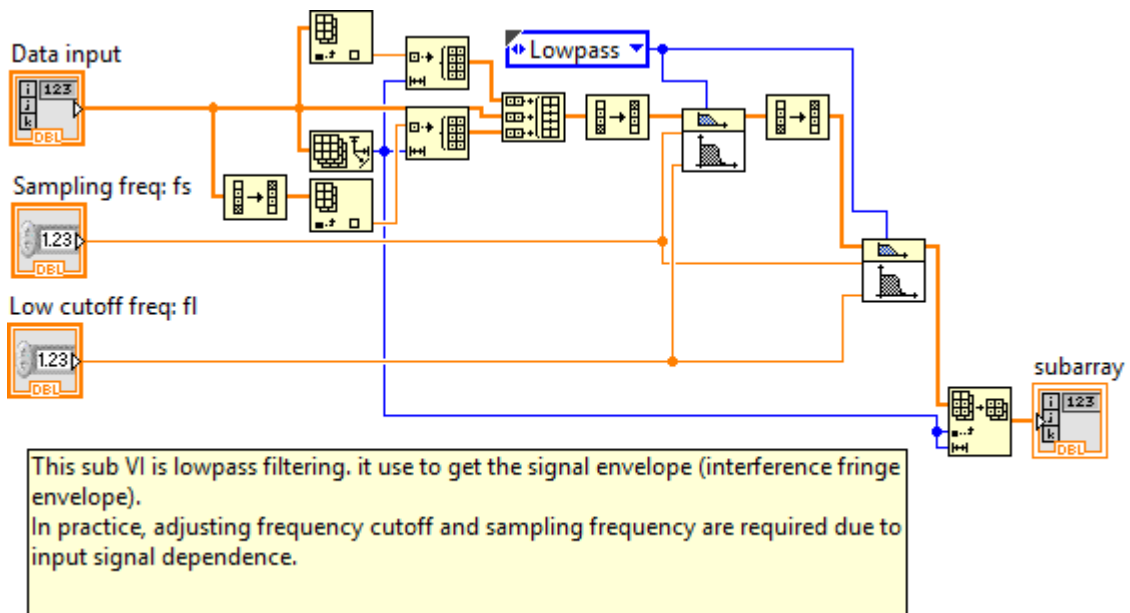
Fig. A7 Lowpass filtering function.

Fig. A8 Peak detection function.

Fig. A9 Positions of peaks identify function.

165

```
1    % Group refractive index of air calculation based on Ciddor's equation
2    % Constants used in the BIPM 1981/91, The saturation vapor pressure of water:
3    format long
4    A=1.2378847e-5;
5    B=-1.9121316e-2;
6    C=33.93711047;
7    D=-6.3431645e3;
8    % Calculation of the saturation water vapor pressure of water vapor ib air at temp
9    svp=exp(A*(t+273.15)^2+B*(t+273.15)+C+D/(t+273.15));
10
11   % Constants of the enhancement factor of water vapor:
12   lpha=1.00062;
13   beta=3.14e-8;
14   gamma=5.6e-7;
15   % Calculation of the enhancement factor of water vapor in air:
16   f=lpha+(beta*p)+(gamma*t^2); % p is air pressure expressed in Pa
17   xw=f*h*svp/p; % h is fraction of humididy between 0-1
18
19   % Constants involved in the standard phase and group refractivities of dry air:
20   %xc=450; % CO2 assumed 450 ppm
21   sigma=1/wavelength ; % Wavenumber
22   k0=238.0185;
23   k1=5792105;
24   k2=57.362;
25   k3=167917;
26   ngasx_eq10RightTerm=(((k1*(k0+sigma^2))/(k0-sigma^2)^2)+(k3*(k2+sigma^2
27   Ma=10^-3*(28.9635+12.011e-6*(xc-400));
28
29   % Constants for the compressibility:
30   a0=1.58123e-6;
31   a1=-2.9331e-8;
32   a2=1.1043e-10;
33   b0=5.707e-6;
34   b1=-2.051e-8;
35   c0=1.9898e-4;
36   c1=-2.376e-6;
37   d=1.83e-11;
38   e=-0.765e-8;
39   Za=1-((101325/288.15)*(a0+(a1*t)+(a2*t^2)))+((101325/288.15)^2*(d));
40   Zw=1-((1333/293.15)*(a0+(a1*t)+(a2*t^2)+(b0+(b1*t))+(c0+(c1*t))))+((1333/293.
41
42   Mw=0.018015;
43   R=8.314510;
44   paxs=(101325*Ma)/(Za*R*288.15);
45   pws=((1333*Ma)/(Zw*R*293.15))* (1-(1-(Mw/Ma)));
46   Z=1-(p/(t+273.15))*((a0+(a1*t)+(a2*t^2))+(b0+(b1*t))*xw)+((c0+(c1*t))*xw^2))+
47   pa=(p*Ma*(1-xw))/(Z*R*(t+273.15));
48   pw=(p*Mw*xw)/(Z*R*(t+273));
49
50   % Constants for STD water vapor:
51   cf=1.022;
52   w0=295.235;
53   w1=2.6422;
54   w2=-0.032380;
55   w3=0.004028;
56   ngws_eq11RightTerm=cf*(w0+(3*w1*sigma^2)+(5*w2*sigma^4)+(7*w3*sigma^
57   % Group index calculation
58   np_1Eq5=(pa/paxs)*ngasx_eq10RightTerm+(pw/pws)*ngws_eq11RightTerm;
59   ng=1+(np_1Eq5*10^-8);
```
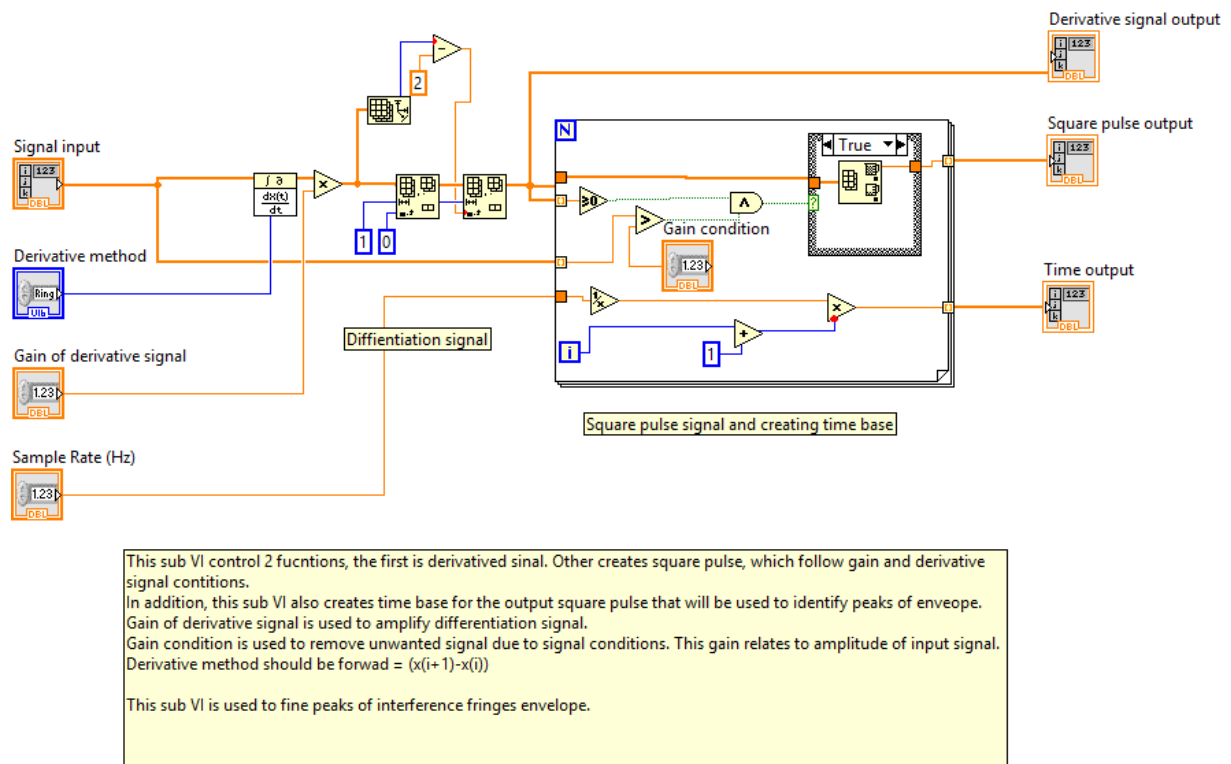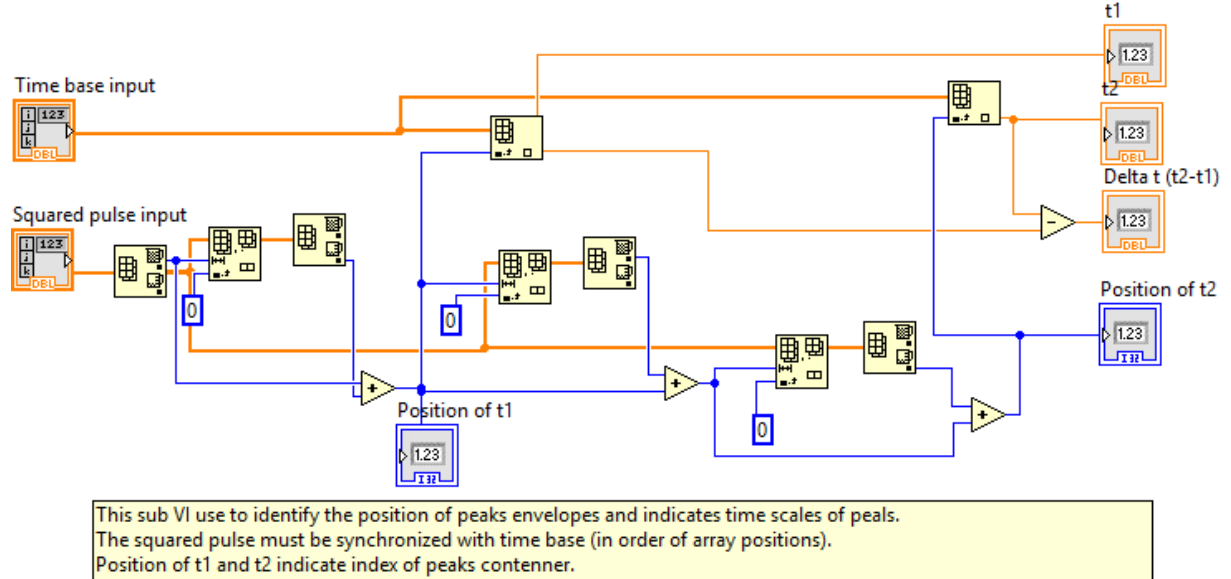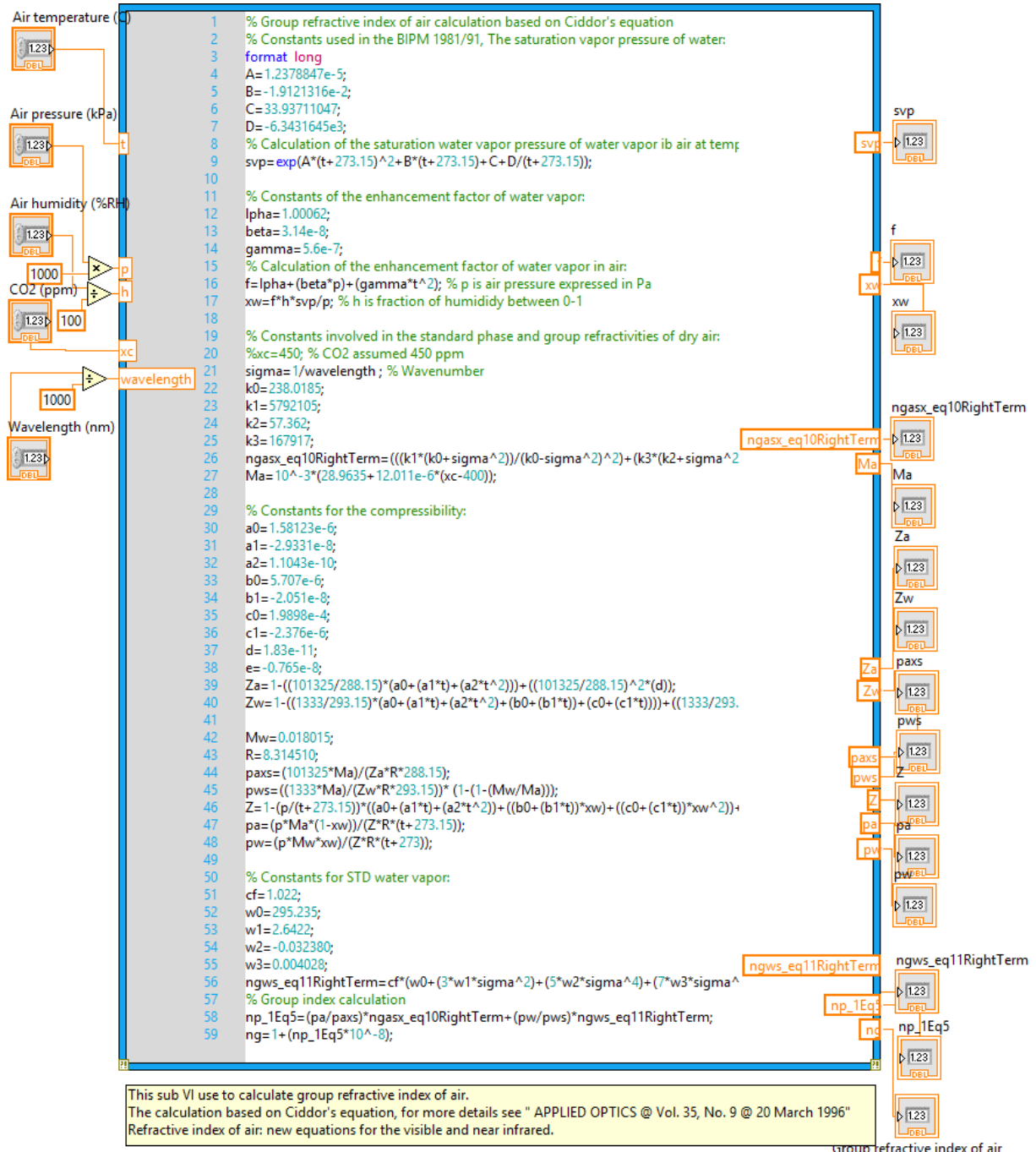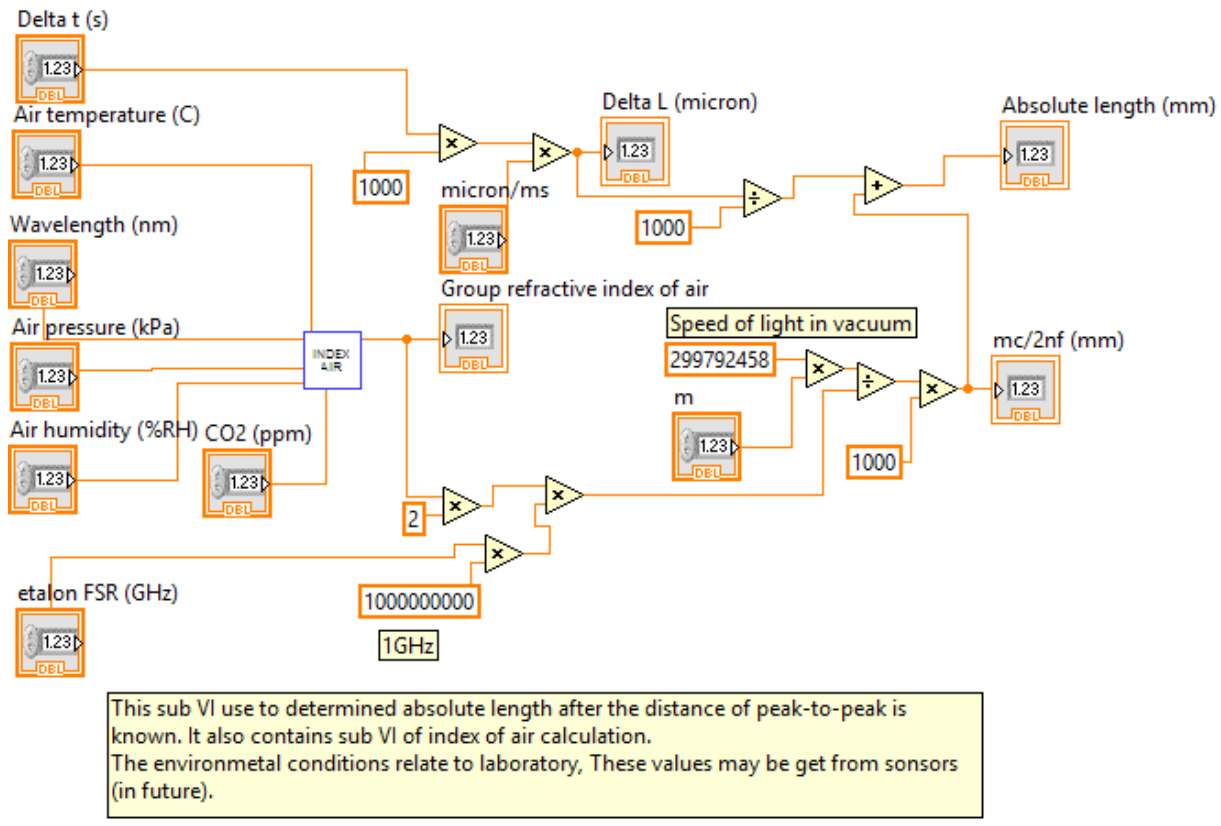
Input labels: Air temperature (C), Air pressure (kPa), Air humidity (%RH), CO2 (ppm), Wavelength (nm)

Output labels: svp, f, xw, ngasx_eq10RightTerm, Ma, Za, Zw, paxs, pws, Z, pa, pw, ngws_eq11RightTerm, np_1Eq5, Group refractive index of air

This sub VI use to calculate group refractive index of air.
The calculation based on Ciddor's equation, for more details see " APPLIED OPTICS @ Vol. 35, No. 9 @ 20 March 1996"
Refractive index of air: new equations for the visible and near infrared.

Fig. A10 Group reflective index of air compensation function.

Fig. A11 Absolute-length calculation function.